

3D Radon Transform for Seismic Data Processing

BY

Arbab Latif

A Dissertation Presented to the
DEANSHIP OF GRADUATE STUDIES

KING FAHD UNIVERSITY OF PETROLEUM & MINERALS

DHAHRAN, SAUDI ARABIA

1963 ١٣٨٣

In Partial Fulfillment of the
Requirements for the Degree of

DOCTOR OF PHILOSOPHY

In

ELECTRICAL ENGINEERING


December 2017


KING FAHD UNIVERSITY OF PETROLEUM & MINERALS
DHAHRAN 31261, SAUDI ARABIA


DEANSHIP OF GRADUATE STUDIES


This thesis, written by **ARBAB LATIF** under the direction of his thesis adviser and approved by his thesis committee, has been presented to and accepted by the Dean of Graduate Studies, in partial fulfillment of the requirements for the degree of **DOCTOR OF PHILOSOPHY IN ELECTRICAL ENGINEERING**.

Dissertation Committee


Dr. Wail A. Mousa (Adviser)


Dr. Azzedine Zerguine (Co-adviser)



Dr. Abdullatif A. Al-Shuhail
(Member)


Dr. Ali Muqabel (Member)


Dr. Saleh Al-Dossary (Member)



Dr. Ali Ahmad Al-Shaikhi
Department Chairman


Dr. Salam A. Zummo
Dean of Graduate Studies

15/2/2018
Date



©Arbab Latif
2017

*Dedicated to my Life, my Wife, **Iffat!***

ACKNOWLEDGMENTS

Thanks to Almighty Allah for giving me opportunity, strength, and His blessing in completing this dissertation.

I would like to thank KFUPM for providing me the opportunity to complete my Ph.D. degree. Foremost, I want to thank my advisor, Dr. Wail A. Mousa, for introducing me to the seismic signal processing. His enthusiasm, advice, immense knowledge and guidance made this research possible.

I would also like to thank the committee members: Dr. Al-Shuhail, Dr. Al-Dossary, Dr. Zerguine, and Dr. Muqaibel, for their invaluable comments, feedback, and insightful suggestions throughout this research work. Furthermore, I would like to thank Deanship of Graduate Studies for providing me the scholarship for this Ph.D. degree.

I can never give enough thanks to my wife, parents for their great encouragement and trust in me during difficult times. In particular, the patience, courage, love, support, and understanding shown by my wife during the honors years, is greatly appreciated.

TABLE OF CONTENTS

ACKNOWLEDGEMENT	v
LIST OF TABLES	ix
LIST OF FIGURES	x
ABSTRACT (ENGLISH)	xiv
ABSTRACT (ARABIC)	xvi
CHAPTER 1 INTRODUCTION	1
1.1 Thesis Contributions	3
1.1.1 Angle-based Radon transform	4
1.1.2 Projections onto convex sets based Radon transform	4
1.1.3 An Efficient apex-shifted hyperbolic Radon transform	5
1.2 Thesis Organization	6
CHAPTER 2 BACKGROUND ON THE RADON TRANSFORM	8
2.1 Introduction	8
2.1.1 Applications	9
2.1.2 The generalized Radon transform	9
2.2 Properties of Radon transform	10
2.3 Inversion of the Radon transform	16
2.4 Radon transform in Seismology	17
2.5 Linear Radon transform	22

2.5.1	Types of Linear Radon transform	23
2.5.2	Linear Radon transform of different curves	27
2.6	Hyperbolic Radon transform	30
2.6.1	NMO Corrected Radon transform	31
2.6.2	The Shifted-Hyperbolic Radon transform	32
2.7	Parabolic Radon transform	33
2.7.1	Types of Parabolic Radon transform	36
2.7.2	Inverse Parabolic Radon	39
2.7.3	Parabolic Radon transform of different curves	40
2.8	Conclusion	43
CHAPTER 3 ANGLE BASED RADON TRANSFORM		44
3.1	Introduction	45
3.2	Mathematical Formulation	49
3.2.1	3-D angle based Radon Transform	51
3.3	Application	53
3.3.1	Performance Metrics	54
3.3.2	Synthetic Data	55
3.4	Interpolation of Missing Seismic Events	65
3.4.1	Simulation Result	66
3.5	Multiple Removal	82
3.5.1	Simulation Results	88
3.6	Conclusion	95
CHAPTER 4 PROJECTIONS ONTO CONVEX SETS BASED RADON TRANSFORM		96
4.1	Introduction	97
4.1.1	Projections onto convex sets	97
4.2	The proposed POCS based Radon transform	101
4.3	Simulation Results	106
4.3.1	2-D Data with linear events	106

4.3.2	2-D Data with non-linear events	109
4.3.3	3-D Real Marine data	119
4.4	Conclusion	126
CHAPTER 5 AN EFFICIENT HYPERBOLIC RADON TRANS-		
	FORM	127
5.1	Introduction	128
5.1.1	The Shifted-Hyperbolic Radon transform	129
5.2	The Proposed efficient Hyperbolic Radon transform	132
5.2.1	Computational Efficiency	134
5.3	Simulation Results	135
5.3.1	3-D Data	139
5.4	Conclusion	143
CHAPTER 6 CONCLUSION		144
6.1	Further Work	147
REFERENCES		149
VITAE		162

LIST OF TABLES

3.1	Mean squared error for the angle-based Radon transform method versus other Radon transform methods for Figure 3.2a.	64
3.2	Mean squared error for the angle-based Radon transform method versus other Radon transform methods for Figure 3.14(a).	80
3.3	Mean squared error for the proposed angle-based Radon transform method versus other Radon transform methods for 3-D Real Dataset.	82
3.4	Mean squared error for the proposed angle-based Radon transform method versus other Radon transform methods for Figure 3.24(b).	93
4.1	Mean squared error for the proposed POCS based Radon transform method versus other Radon transform methods for Figure 4.10(a).	119
4.2	Mean squared error for the proposed angle-based Radon transform method versus other Radon transform methods for 3-D Real Dataset.	122
5.1	Time comparison: Proposed and traditional apex shifted Radon transform	137

LIST OF FIGURES

2.1	Projections of a function along (a) straight lines and (b) parabolic path.	11
2.2	Radon transform: Projections along x,y-axis.	12
2.3	Generalized Radon transform	13
2.4	Radon transform of a Phantom image	18
2.5	Unfiltered inverse Radon transform	19
2.6	Filtered inverse Radon transform	20
2.7	Hyperbola approximation using (a) shifted hyperbolic approximation and (b) Dix approximation.	34
2.8	Hyperbolic Radon transform	35
3.1	Representation of line in term of θ	50
3.2	Angle-based Radon transform for synthetic seismic reflected data	57
3.3	CG-FFT based Radon transform for synthetic seismic reflected data	58
3.4	Least square based Radon transform for synthetic seismic reflected data	59
3.5	Angle-based Radon transform for synthetic seismic reflected data with 10% noise	60
3.6	CG-FFT based Radon transform for synthetic seismic reflected data with 10% noise	61
3.7	Angle-baed Radon transform for synthetic seismic reflected data with 20% noise	62

3.8	Angle-based Radon transform for synthetic seismic reflected data with 40% noise	63
3.9	Reconstruction of 10 % missing traces using angle-based Radon transform	67
3.10	Reconstruction of 40 % missing traces using angle-based Radon transform	69
3.11	Reconstruction of 10 % missing traces using angle-based Radon transform	70
3.12	Reconstruction of missing traces with 30% compression and 10% Noise using angle-based Radon transform	71
3.13	Reconstruction of missing traces with 20% compression and 40% Noise using angle-based Radon transform	72
3.14	Reconstruction of missing traces with 10% compression using angle-based Radon transform	74
3.15	Reconstruction of missing traces with 30% compression using angle-based Radon transform	75
3.16	Reconstruction of missing traces using traditional Radon transform with 20% compression using CG-FFT based Radon transform	76
3.17	Reconstruction of missing traces using traditional Radon transform with 20% compression using least square based Radon transform	77
3.18	Reconstruction of missing traces using angle based Radon transform with 20% compression	78
3.19	Reconstruction of missing traces using angle based Radon transform with 20% compression	79
3.20	3-D Real Data from Waihapa, New Zealand	83
3.21	Reconstruction of missing traces with 20% compression using angle-based Radon transform	84
3.22	Reconstruction of missing traces with 20% compression using angle-based Radon transform	85

3.23	Reconstruction of missing traces with 20% compression using CG-FFT Radon transform	86
3.24	Multiple attenuation using angle-based Radon transform	89
3.25	Multiple attenuation using CG-FFT based Radon transform	91
3.26	Multiple attenuation using angle-based Radon transform	92
3.27	Multiple-reflection attenuation by Radon transform	94
4.1	Example of convex set.	98
4.2	Example of convex and concave sets.	99
4.3	Projections onto convex sets example for two closed and convex sets C_1 and C_2	102
4.4	Interpolation using POCS and Radon transform for synthetic seismic data.	108
4.5	Interpolation using POCS and Radon transform for synthetic seismic data with 10% random Gaussian noise.	110
4.6	Interpolation using POCS and Radon transform for synthetic seismic data with 40% random Gaussian noise.	111
4.7	(a) Interpolation of missing seismic traces using Radon transform with total number of traces 481 with 161 missing traces.(b) Interpolated data with POCS and parabolic Radon transform.	112
4.8	(a) The synthetic seismic reflected data and (b) data after 40 missing traces. (c) The interpolated data after applying the POCS with parabolic Radon transform.	113
4.9	Reconstruction of missing traces with 30% compression and 20% Noise using POCS with parabolic Radon transform	114
4.10	Reconstruction of missing traces with 10% compression using POCS with parabolic Radon transform	116
4.11	Reconstruction of missing traces using traditional Radon transform with 30% compression sing CGG-FFT based Radon transform	117

4.12	Reconstruction of missing traces using traditional Radon transform with 20% compression using least square Radon transform	118
4.13	Reconstruction of missing traces using POCS and Radon transform with 20% compression	120
4.14	3-D Real Data from Waihapa, New Zealand	122
4.15	Reconstruction of missing traces with 20% compression	123
4.16	Reconstruction of missing traces with 20% compression	124
4.17	Reconstruction of missing traces with 20% compression using CG- FFT Radon transform	125
5.1	The hyperbolic Radon transform	130
5.2	Efficient apex-shifted hyperbolic Radon transform	136
5.3	Traditional apex-shifted hyperbolic Radon transform	138
5.4	3-D Real Data from Waihapa, New Zealand (Courtesy of New Zealand Petroleum and Minerals (NZPM)).	140
5.5	The real in-line data from the Waihapa, New Zealand	141
5.6	The real cross-line data from the Waihapa, New Zealand.	142

THESIS ABSTRACT

NAME: Arbab Latif
TITLE OF STUDY: 3D Radon Transform for Seismic Data Processing
MAJOR FIELD: Electrical Engineering
DATE OF DEGREE: December 2017

Data processing of seismic data is one of the most crucial steps in seismic exploration. Once acquired, the data has low resolution due to the presence of noise and unwanted energies (e.g.; multiple reflections, ground roll, etc.). Furthermore, the acquired data is huge, mostly in terabytes. Processing of such large amounts of data is expensive; hence, it requires time and lots of resources. Therefore, techniques that can process the data efficiently and effectively are needed. One of the techniques that has been used in seismic for quite some time, is the use of Radon transform. The Radon transform is robust and is part of the seismic processing for last three decades. However, due to the increase in complexity of the acquired data and demand for high-resolution data, there is a need for efficient ways to calculate and process data in Radon domain. In this thesis, three different methods to compute Radon transform are proposed and investigated for the seismic data pro-

cessing. The first method proposes an additional (angle based) parameter for the traditional Radon transform, which results in high resolution, robust Radon transform without the need of move-out correction, which is required for the traditional Radon transform. Furthermore, the angle based Radon transform even works for the far offset. The second method utilizes the projections onto the convex sets along with regular Radon transform to find the missing seismic traces which is a key step in seismic data processing. The last proposed technique is an efficient way to calculate the apex shifted hyperbolic Radon transform. This method utilizes the prior information to calculate the Radon transform effectively and is about 12 times faster than the existing apex shifted hyperbolic Radon transform. These proposed methods are tested for the multiple reflection removal, reconstruction of missing traces. The proposed methods are computationally more efficient than the existing methods and are robust under noisy conditions. The methods were tested on synthetic and real, 2-D and 3-D seismic dataset, with different compression levels and various levels of additive white Gaussian noise. Therefore, since the new methods are efficient and robust than existing techniques, it is believed that the proposed methods are an appropriate new addition to the existing methods for computing high-resolution Radon transform.

ملخص الرسالة

الاسم الكامل: ارباب لطيف

عنوان الرسالة: 3D تحويل الرادون لمعالجة البيانات الزلزالية

التخصص: الهندسة الكهربائية

تاريخ الدرجة العلمية: ديسمبر 2017

معالجة البيانات من البيانات الزلزالية هي واحدة من أهم الخطوات في الاستكشاف الزلزالي. وبمجرد الحصول عليها، فإن البيانات منخفضة الدقة بسبب وجود ضوضاء والطاقت غير المرغوب فيها. لذلك، هناك حاجة إلى التقنيات التي يمكن معالجة البيانات بكفاءة وفعالية. واحدة من التقنيات التي استخدمت في الزلزالي لبعض الوقت، هو استخدام تحويل الرادون. في هذه الأطروحة، يتم اقتراح ثلاث طرق مختلفة لحساب تحويل الرادون والتحقق في معالجة البيانات الزلزالية. تقترح الطريقة الأولى معلمة إضافية (زاوية قائمة) لتحويل رادون التقليدي، مما يؤدي إلى ارتفاع القرار، وتحويل الرادون قوية دون الحاجة إلى تصحيح الخروج، وهو مطلوب لتحويل رادون التقليدية. وعلاوة على ذلك، فإن رادون على أساس زاوية تحويل حتى يعمل على تعويض بعيد. الطريقة الثانية تستخدم الإسقاطات على مجموعات محدبة جنباً إلى جنب مع تحويل الرادون العادية للعثور على آثار الزلزالية المفقودة التي هي خطوة رئيسية في معالجة البيانات الزلزالية. آخر تقنية المقترحة هي وسيلة فعالة لحساب تحول رأسية الزائدية التحول الزائدي. تستخدم هذه الطريقة المعلومات المسبقة لحساب تحويل الرادون بشكل فعال وحوالي 10 مرات أسرع من تحويل رادوني الزائدي المتغير الحالي. يتم اختبار هذه الطرق المقترحة لإزالة انعكاس متعددة، وإعادة بناء آثار المفقودين. الطرق المقترحة هي أكثر كفاءة من الناحية الحسابية من الطرق القائمة وهي قوية في ظل ظروف صاخبة. لذلك، وبما أن الأساليب الجديدة فعالة وقوية من التقنيات القائمة، ويعتقد أن الطرق المقترحة هي إضافة جديدة مناسبة للطرق القائمة لحساب عالية الدقة تحويل الرادون.

CHAPTER 1

INTRODUCTION

The consumption of oil and gas is increasing at a rapid rate due to, which discovered reservoirs are diminishing with the passage of time. The accurate exploration of new reservoirs of oil and gas is becoming more important with the passage of time [1]. The ultimate aim of the seismic exploration is to obtain accurate information (images) of the earth subsurface so one can identify the hydrocarbons structure present below the earth surface, without any expensive or time-consuming drilling.

Seismic data processing plays an important role in achieving this goal [2]. Earth is composed of different layers with different physical properties. The acquired seismic data contain reflections from these different layers [3,4]. By analyzing these layers, geologists, after obtaining the final image of the subsurface, can predict the likelihood of hydrocarbons existence. Due to the complex geological conditions, different kinds of reflections are generated. The acquired data has low resolution due to the presence of noise and unwanted energies (e.g; multiple

reflection and ground roll) from the same layer, which in turn make the processing of seismic data more difficult. In general, as the complexity of the earth structure of the concerned area is increased, increasing the resolution and the removal of noise become more challenging and require more sophisticated processing techniques. Besides the difficulty in identification of primary reflections, one also faces difficulties in the data analysis and interpretation [1].

For seismic data processing, various approaches have been proposed and applied including the industry standard Radon transformation [5–8]. The generalized Radon transform is the tool that is heavily used in many applications for image processing [9], medical imaging [10, 11], solution of mathematical problems [12, 13] and, most importantly in the field of reflection seismic data processing [5, 6, 14–18]. Radon transform is robust in nature and has attracted the attention of seismic data processing scientists and engineers during the last two decades. It is being used for quite some time in different applications which includes seismic deconvolution [6], multiple removal as discussed in [16, 19–21], first arrival picking or enhancement [14, 22]. Besides the low-resolution Radon transform, high resolution along with sparse fast high-resolution Radon transform has been proposed and used in the industry. The concept of sparse Radon transform was introduced by Thorson [20], who presented a low-resolution Radon transform using least squares. High-resolution Radon transform in frequency domain was proposed by [23], which utilized the regularization technique. Although the regularization method enhanced the focusing power of the transform, however,

the inversion was computationally expensive. Since then different version of fast high-resolution Radon transform has been proposed, some examples are available in [5, 8, 17, 22, 24–28].

There exist three types of Radon transform used for seismic data processing [29]. These transforms are the linear Radon transform (slant-stack), the parabolic Radon transform, and the hyperbolic Radon transform. As the name suggests, the linear Radon transform integrates the data along the planar surfaces and maps linear events (e.g., direct arrivals, ground rolls, etc.) to single points. Similarly, parabolic and hyperbolic Radon transforms maps parabolic and hyperbolic events (e.g., primary reflections, multiple reflections, etc.) to a single point, respectively. In other words, the Radon transform transforms the data from the time-space domain (t, x) to the linear Radon domain $(\tau - p)$ or parabolic /hyperbolic Radon domain $(\tau - q)$, where $p = 1/v$, $q = 1/v^2$ and v is the velocity. Since the travel time curve for a primary reflection seismic event is hyperbolic in nature, therefore, hyperbolic Radon transform provides the best approximation and resolution. However, hyperbolic Radon transform is difficult to compute and computationally, it is quite expensive, therefore, the parabolic Radon transform is mostly used due to its effectiveness and low computational cost [5].

1.1 Thesis Contributions

In this thesis, three variants of Radon transforms are proposed, which produce high-resolution Radon transforms for 2-D and 3-D seismic data.

1.1.1 Angle-based Radon transform

The first proposed Radon transform proposes a new angle based parameter along with the traditional Radon transform to produce high-resolution Radon transform. The proposed method produces a sparse representation of seismic data in the Radon domain, without the need of normal move-out correction and works for far offset as compared to the existing parabolic Radon transform. Normal move-out correction is a tedious process requiring human interaction and is required for the parabolic Radon transform. The proposed method was applied to the synthetic data with different levels of noise and from the result, it is evident that the angle based Radon transform is robust and provide an accurate estimation of the seismic events. The method is also tested for the interpolation of seismic data and multiple attenuations for 2-D and 3-D seismic data.

1.1.2 Projections onto convex sets based Radon transform

In most cases, due to the certain limitations of the hardware, budgets, and computing power, it is not possible to collect large samples of seismic traces. Sometimes, due to poor conditions or the topological structures of Earths surface, it is not possible to place seismic sensors (geophones) resulting in missing traces in the acquired data. Hence, the interpolation of missing seismic traces is an important step of the seismic data processing and there are several different methods to solve this problem. The second proposed method uses the projections onto convex sets (POCS) along with Radon transform to find the missing seismic traces. The

problem of missing seismic traces is posed in terms of different convex sets and POCS is used to find the missing traces. Different conditions are applied both in time-offset and Radon domain to obtain the missing traces. The proposed method is applied to 2-D and 3-D seismic data sets with the different number of missing traces and different noise levels. The simulation results show that the proposed method is robust and provides better results than the existing Radon transform based interpolation methods.

1.1.3 An Efficient apex-shifted hyperbolic Radon transform

Travel time curves for seismic events are hyperbolic in nature, and hyperbolic Radon transform is the one that can provide the sparsest representation of these events. However, the hyperbolic Radon transform can only be calculated in the time domain, which is computationally expensive and there is a need to find ways for faster computation. One variant of the hyperbolic Radon transform is the apex-shifted hyperbolic Radon transform which is more robust, and computationally expensive than the existing hyperbolic Radon transform. The third contribution is an efficient way of calculating this apex-shifted hyperbolic Radon transform is proposed. The proposed algorithm utilizes the prior knowledge from the adjoint-based Radon transform (low resolution) to reduce the search space of the Radon parameters. The method is applied to 2-D and 3-D seismic data sets and the results show that the proposed method is robust and about k , number of

iterations, times faster than the traditional hyperbolic Radon transform.

1.2 Thesis Organization

The thesis is organized as follows. Chapter 2 provides information about the origin and history of Radon transform. It includes the properties and inversion methods for the Radon transform. It is followed by different types of Radon transforms used in the seismic processing. Continuous as well discrete versions, along with the properties and limitations of the existing transforms, are discussed in that chapter.

In Chapter 3, the first proposed method for the robust and high-resolution Radon transformation is presented. The method utilizes an angle based parameter, along with the traditional Radon transform, to produce a high-resolution Radon transform for 2-D and 3-D seismic data. Simulation results, for different datasets with different level of noise, are presented. A comparison with the existing high-resolution Radon transform is also included in the chapter.

Next proposed method, interpolation of missing seismic traces using projections onto convex sets, is presented in Chapter 4. It starts with a brief introduction of the POCS, which is followed by the mathematical formulation of the proposed method. Simulation results, for 2-D and 3-D seismic datasets with different level of noise, are also presented in Chapter 4.

Chapter 5 presents the proposed method for efficient implementation of apex-shifted hyperbolic Radon transform. Different variants of hyperbolic Radon trans-

form and importance of hyperbolic Radon transform is discussed. It is followed by the proposed method and its comparison with the traditional hyperbolic Radon transform.

Concluding remarks of this thesis and future work are presented in Chapter 6.

CHAPTER 2

BACKGROUND ON THE RADON TRANSFORM

2.1 Introduction

The Radon transform is named after Johann Karl August Radon. He was an Austrian mathematician who introduced the Radon transform in 1917 [11]. Initially, he only introduced the transform pair (forward as well as inverse transform) for straight lines. Later, Radon also presented the formulas for the transform in three-dimensions [30]. Now, Radon transform has been generalized to higher-dimensional Euclidean spaces [31]. Although initially the Radon transform was introduced without any practical application, the concept of Radon transforms, however, led to a Nobel-prize in 1979 for the groundbreaking concept of viewing organs from outside the body using Tomography [32]. The mathematical theory of Radon transform was discussed by Deans [33]. Also, fundamental properties of

the Radon transform were examined by Durrani Bisset [11].

2.1.1 Applications

Radon transform has been used a lot in recent past. The most common application is the process of reconstructing images. Removing multiples from the shot gathers data has been the biggest problem of exploration geophysics. As these reflections interferes with the primary reflections and decrease the resolution of the obtained data. For this purpose Radon transform has been used a lot.

Besides reflection seismology Radon transform is widely used in tomography. In tomography an image is obtained from the data scattered after the cross-sectional scans of an object [11]. Scattered data is represented in Radon domain. Inverse Radon transform is used to obtain the original image from the scattered data. Besides the use in tomography Radon transform is widely used in applications related to computer vision, line detection, computed axial tomography (CAT scan), bar-code scanners. Radon transform is also used for the Electron microscopy of viruses and protein complexes [10, 11, 13]. Recently, it has been used for the solution of hyperbolic partial differential equations [12, 13].

2.1.2 The generalized Radon transform

The Radon transform is an integral transform that integrates the data along a specific curve. It calculates the projections of an image along specified directions. In the case of a two-dimensional (2-D) function, the line integral is considered as

the projection of the function along x -axis or y -axis [34]. If the line integral of 2-D function $g(x, t)$ is taken along the vertical direction, then it is known as the projection onto the x -axis. On the other hand, the projection onto the y -axis, is the line integral in the horizontal direction (-see Figure 2.1). To completely represent an image, multiple, projections from different angles are recorded as shown in Figure 2.2.

The generalized Radon transform of a function $g(x, \phi(x; \eta))$ is defined as [35]:

$$\hat{g}(\eta) = \int_{-\infty}^{\infty} g(x, \phi(x; \eta)) dx, \quad (2.1)$$

where η spans the continuous parameter domain. In discrete form, Radon transform is represented as:

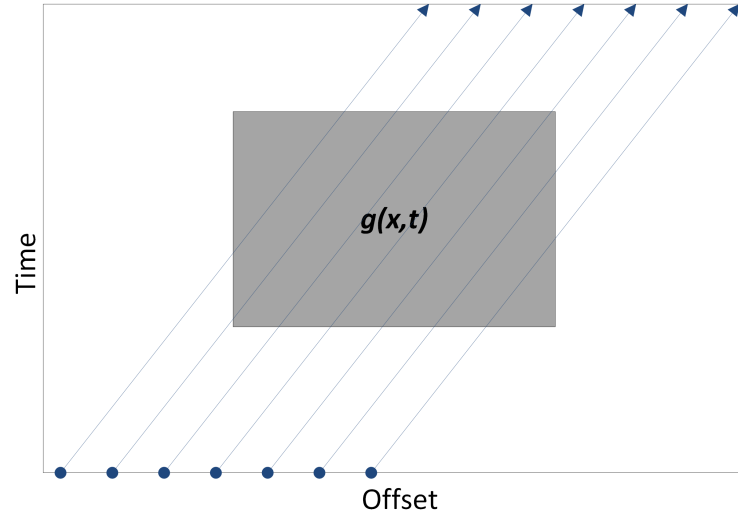
$$\hat{g}(\Omega) = \sum_{m=0}^{M-1} g(m, \phi(m; \Omega)), \quad (2.2)$$

here Ω spans the parameter domain.

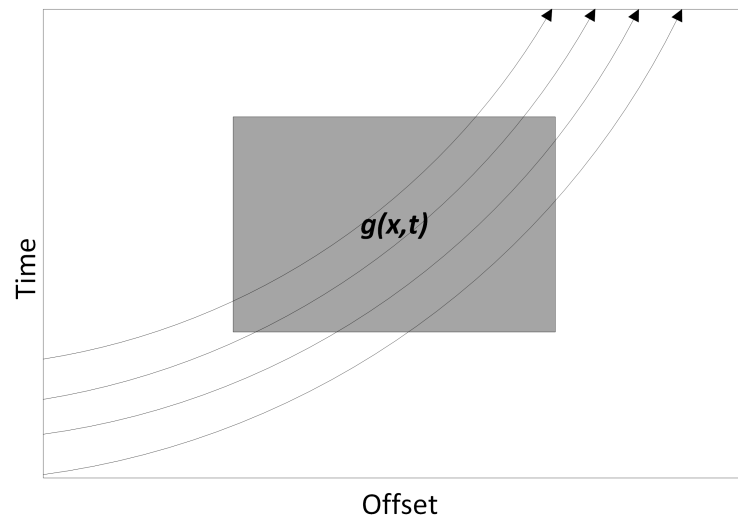
Figure 2.3 shows an example of the Radon transform of a square image. Figure 2.3(a) presents the data whose Radon transform is presented in Figures 2.3(b) and 2.3(c).

2.2 Properties of Radon transform

Some basic properties of the Radon transform are discussed here for 2-D function $g(x, t)$ [29]. For the sake of simplicity, let $\eta = \{p, \tau\}$ and $g(x, \phi(x; \eta)) = px + \tau$.



(a)



(b)

Figure 2.1: Projections of a function along (a) straight lines and (b) parabolic path.

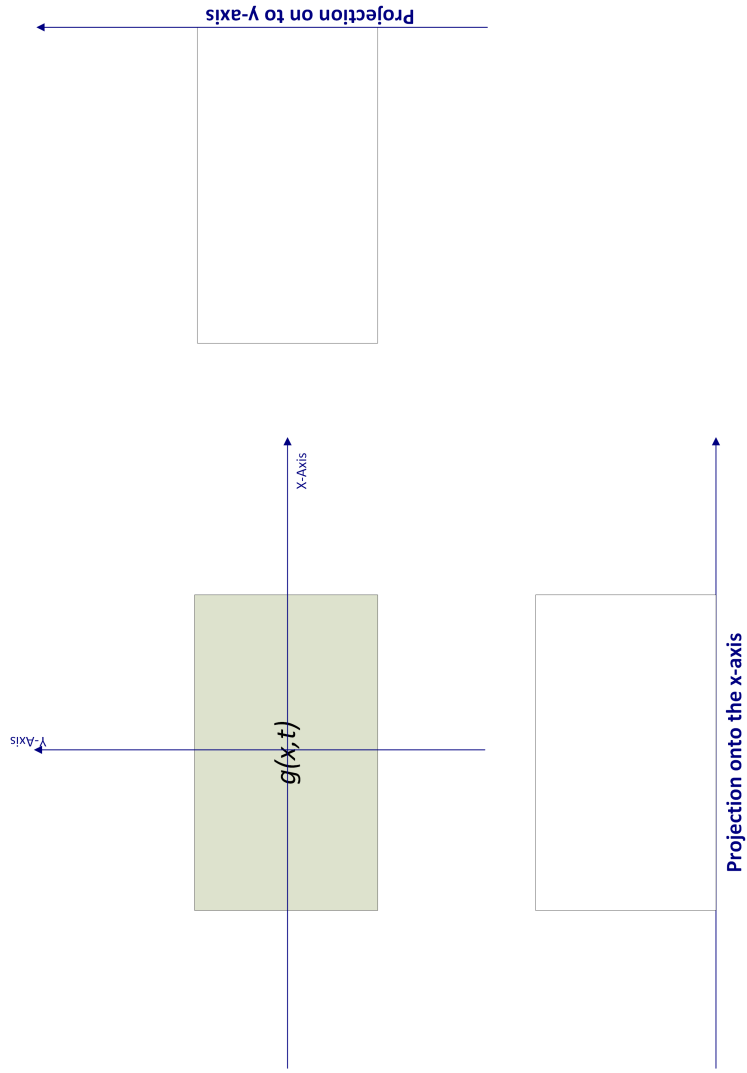
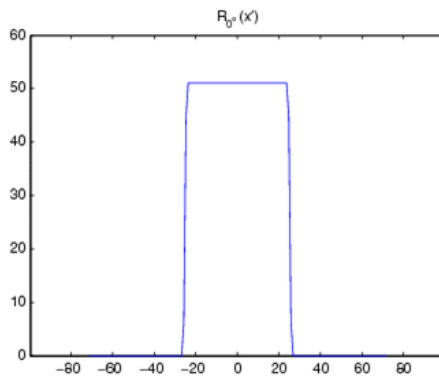


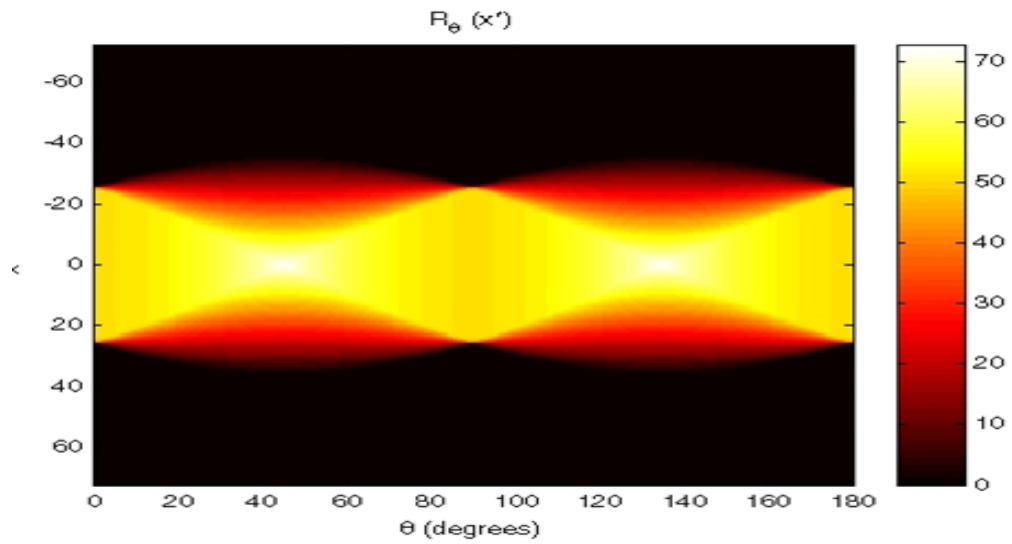
Figure 2.2: Projections along x,y-axis.



(a)



(b)



(c)

Figure 2.3: Generalized Radon transform: (a) Original Image (b) Projection 0 degree (c) Radon transform.

So, Radon transform Equation 2.1 become:

$$\hat{g}(p, \tau) = \int_{-\infty}^{\infty} g(x, \phi(x; px + \tau)) dx. \quad (2.3)$$

The above equation can also be written in terms of delta function:

$$\hat{g}(p, \tau) = \int_{-\infty}^{\infty} \int_{-\infty}^{\infty} g(x, t) \delta(y - px - \tau) dx dy.$$

Here delta function is given by:

$$\delta(t) = \begin{cases} 0 & t \neq 0 \\ \infty & t = 0 \end{cases} \quad (2.4)$$

Linearity

Radon transform is linear in nature. It means that the Radon transform of sum of function is equal to the sum of Radon transform of individual functions. Let $h(x, t)$ be the sum of the functions, $g_i(x, t)$ for which one want to evaluate the Radon transform; i.e. :

$$h(x, t) = \sum_i w_i g_i(x, t). \quad (2.5)$$

Taking the Radon transform of the previous equation:

$$\begin{aligned} \hat{h}(p, \tau) &= \sum_i w_i \int_{-\infty}^{\infty} \int_{-\infty}^{\infty} g_i(x, t) \delta(y - px - \tau) dx dt, \\ &= \sum_i w_i \hat{g}_i(p, \tau). \end{aligned} \quad (2.6)$$

$\hat{h}(p, \tau)$ is the sum of Radon transform of $g_i(x, t)$.

Shift

The Radon transform also obeys the shifting property [29], however, the slope of the line cannot be altered by shifting. So, in case of shifting a 2-D function, the only parameter that is changed in the Radon domain is the offset parameter. The shifting of a 2-D function $g(x, t)$ can be described as follows:

$$h(x, t) = g(x - x^*, t - t^*),$$

where x^*, t^* represents the shift. The Radon transform of $h(x, t)$ is given by:

$$\begin{aligned} \hat{h}(p, \tau) &= \int_{-\infty}^{\infty} g_i(x - x^*, px + \tau - t^*) dx, \\ &= \int_{-\infty}^{\infty} g_i(\tilde{x}, p(\tilde{x} + x^*) + \tau - t^*) d\tilde{x}, \\ &= \hat{g}(p, \tau - t^* + px^*). \end{aligned} \tag{2.7}$$

Scaling

A compression in the t direction results in a compression in the time intercept parameter (τ) of the Radon domain. Similarly scaling of the slope will result in scaling the Radon domain [29]. Mathematically, for a 2-D function $g(x, t)$, the scaling is defined as:

$$h(x, t) = g\left(\frac{x}{a}, \frac{t}{b}\right),$$

where a and b are the scaling parameter. Taking the Radon transform, we obtain:

$$\begin{aligned}
\hat{h}(p, \tau) &= \int_{-\infty}^{\infty} g\left(\frac{x}{a}, \frac{px + \tau}{b}\right) dx, \\
&= a \int_{-\infty}^{\infty} g(\tilde{x}, \frac{pa\tilde{x} + \tau}{b}) dx, \\
&= a\hat{g}\left(\frac{pa}{b}, \frac{\tau}{b}\right).
\end{aligned} \tag{2.8}$$

2.3 Inversion of the Radon transform

To go back from the Radon panel to the time offset domain, inverse Radon transform is used. The inverse transform can be obtained by several available techniques, but the most common inversion techniques are the Fourier Slice Theorem and Filtered Back Projection [36].

The Fourier Slice Theorem shows that the function $g(x, t)$ can be reconstructed by taking the 1-D Fourier transform of the Radon transform which will result in the 2-D Fourier spectrum of $g(x, t)$ [36].

The filtered back algorithm can be divided into two phases, namely, the projection and the filtration. The projection phase is similar to the forward Radon transform. The only difference is that now the line integrals are projected back onto the plane.

For example, consider the phantom image shown in Figure 2.4(a) and its Radon transform in Figure 2.4(b). Filtered back projection is used for the inversion of the 2.4(b) and the results are presented in Figure 2.5. From Figure 2.5, one can see the shapes in the reconstructed image, but the resolution is very low and the

image is blurred. To reduce the blurriness of the reconstructed image, a high pass filter is applied in the frequency domain. So the complete procedure is to take the 1-D Discrete Fourier transform (DFT) of the sinogram data for each angle, then multiply the obtained results with the high pass filter, and finally use the inverse DFT to get the original data back from the Radon domain. The simplest form of high pass filter is a ramp. Applying the ramp filter significantly improves the quality of the reconstructed image. This Filtered Back-projection formula for computing the inverse Radon transform implies that the parameter domain is filtered with the absolute frequency in the t -direction for all values of x , on the other hand, back projection part integrates up along a line [37]:

$$g(x, t) = \int_{-\infty}^{\infty} \bar{g}(p, t - px) dp \quad (2.9)$$

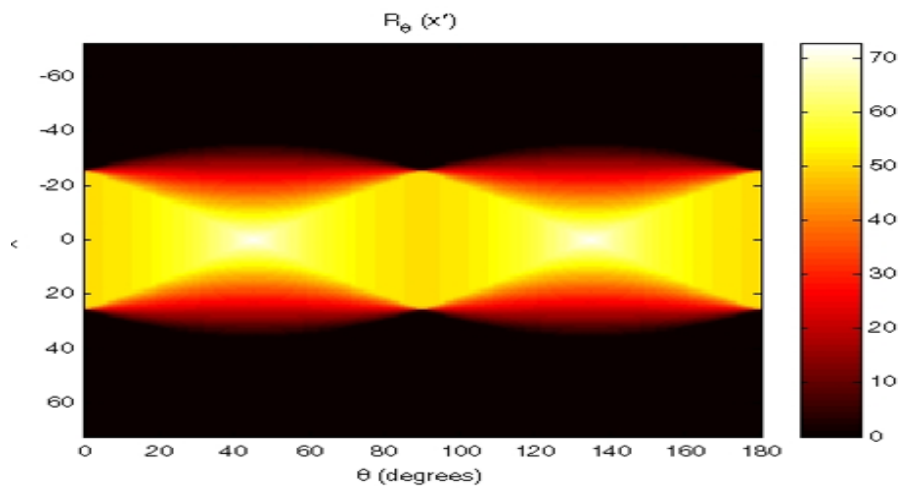
Equation (2.9) shows the result of the filtered back projection. The Figure 2.6 shows the result after the filtration and with no of projections 18, 36, 90, respectively.

2.4 Radon transform in Seismology

One of the critical and important steps of the seismic exploration is the seismic data processing. For seismic data processing, different approaches have been proposed and applied, including the industry standard Radon transformation, which has attracted the attention of seismic data processing engineers and scientists



(a)



(b)

Figure 2.4: Radon transform: (b) Radon transform for the phantom image in (a).

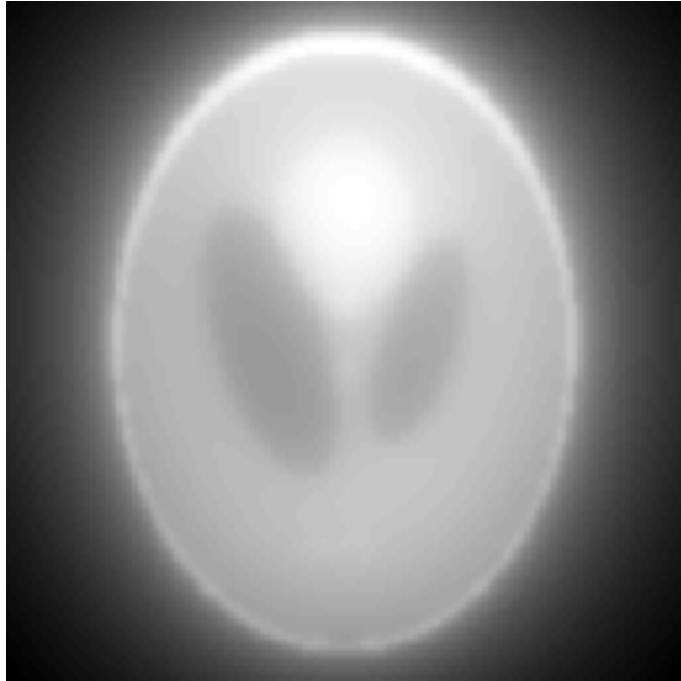
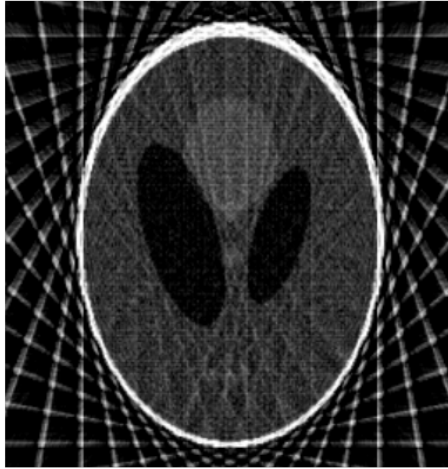


Figure 2.5: Radon transform: Unfiltered inverse Radon transform of 2.4(b).

during the last two decades. There exist three types of Radon transform that are used for seismic data processing [29]. These transforms are the linear Radon transformation (slant-stack), the hyperbolic Radon transform, and the parabolic Radon transform. The parabolic Radon transform is mostly used due to its effectiveness as compared to the linear Radon transform and the low computational cost [5]. The Radon transform transforms the data from the time-space domain (t, x) to the linear Radon domain $(\tau - p)$ or parabolic or hyperbolic Radon domain $(\tau - q)$. One of the distinct features of the Radon transform is that the $\tau - p$ and $\tau - q$ domains provide the sparse representation of the linear and parabolic (or hyperbolic) seismic events, respectively [29]. Besides low-resolution Radon transform, high resolution along with sparse fast, high-resolution Radon transform has been proposed and used in the industry. The concept of sparse Radon trans-



(a)



(b)



(c)

Figure 2.6: Filtered Inverse Radon transform: (a)-(c) 18, 36, and 90 projections, respectively.

form was introduced by [20], who presented, a low-resolution Radon transform using least squares. High-resolution Radon transform in frequency domain was proposed by [23] which utilized the regularization technique. Although the regularization method enhanced the focusing power of the transform, however, matrix transforms into a non-Toeplitz matrix which makes the inversion computationally expensive.

Yilmaz used the t^2 stretch to transform the travel time equation from hyperbolic to parabolic and applied the parabolic Radon transform [12]. Thorson and Claerbout introduced the least-squares solution. It was Foster and Mosher, who applied hyperbolic Radon transform after normal move-out correction. Shifted hyperbolic Radon transform was suggested by Oppert [38]. Due to the high computational cost of hyperbolic Radon transform, different, faster versions of parabolic Radon transform have been proposed for the multiple attenuation [19]. Greenhalgh and Zhou proposed the convolution operators for the linear Radon transform and the parabolic Radon transform [23]. High resolution Radon transform was suggested by Ulrych and Sacchi [5, 26].

Mathematical Model

Let $g(x, t)$ represent the seismic data in offset ' x ' and time ' t '. Then, the generalized Radon transform [35] pair for this seismic data $g(x, t)$ is given as following:

$$u(q, \tau) = \int_{-\infty}^{\infty} g(x, t = \tau + q\phi(x))dx, \quad (2.10)$$

$$\hat{g}(x, t) = \int_{-\infty}^{\infty} u(q, \tau = t - q\phi(x))dq, \quad (2.11)$$

where q and τ are representing some parameters of the curve. Similarly, $\phi(x)$ is the function of the offset parameter ‘ x ’ and depends on the path of integration.

In discrete form these can be represented as

$$u(q, \tau) = \sum_x g(x, t = \tau + q\phi(x)), \quad (2.12)$$

$$\hat{g}(x, t) = \sum_q u(q, \tau = t - q\phi(x)). \quad (2.13)$$

2.5 Linear Radon transform

As the name suggests the linear Radon transform integrates the data along planar surfaces. It transforms linear events to single points in the transformed Radon panel. Linear seismic events are periodic in linear Radon domain (slant stack) and we can use the deconvolution in Radon domain to attenuate these multiples. Forward linear Radon transform was developed by Beylkin when he also applied the filter in the inverse Radon transform domain [39]. Kostov used Toeplitz structure for the least squares solution of the Radon transform [31]. To achieve better resolution, Zhou and Greenhalgh suggested applying the rho filter in the forward Radon transform [40].

Linear Radon transform is obtained by replacing $\phi(x) = x$ and $q = p$ in the generalized Radon transform (Equation 2.10). The linear Radon transform

equations in continuous domain are:

$$u(p, \tau) = \int_{-\infty}^{\infty} g(x, t = \tau + px) dx, \quad (2.14)$$

$$\hat{g}(x, t) = \int_{-\infty}^{\infty} u(p, \tau = t - px) dp. \quad (2.15)$$

Similarly, the discrete form of these equations is obtained from Equation 2.12.

$$u(p, \tau) = \sum_x g(x, t = \tau + px), \quad (2.16)$$

$$\hat{g}(x, t) = \sum_p u(p, \tau = t - px), \quad (2.17)$$

here x is the offset, $g(x, t)$ is representing the seismic data $p = \frac{\sin \theta}{v} = \frac{\Delta t}{\Delta x}$ and $u(p, \tau)$ linear Radon domain. In frequency domain, the linear Radon transform can be represented as:

$$U(p, \omega) = \int_{-\infty}^{\infty} G(x, \omega) e^{i\omega px} dx, \quad (2.18)$$

where, $G(x, \omega)$ represent the data in Fourier domain.

2.5.1 Types of Linear Radon transform

The linear Radon transform, can be sub-divided into following two types:

- Forward Slant Stack
- Inverse Slant Stack

Forward Slant Stack

The first type of Radon transform is known as Forward Slant Stack. It can be obtained by substituting frequency domain equation of the inverse Radon transform (Equation ??) into forward Radon transform Equation 2.18.

$$\hat{G}(x, \omega) = \int_{-\infty}^{\infty} \int_{-\infty}^{\infty} G(\acute{x}, \omega) e^{i\omega p \acute{x}} d\acute{x} e^{-i\omega p x} dp.$$

The above equation can be simplified as shown below:

$$\begin{aligned} \hat{G}(x, \omega) &= \int_{-\infty}^{\infty} \int_{-\infty}^{\infty} G(\acute{x}, \omega) e^{i\omega p(\acute{x}-x)} d\acute{x} dp, \\ &= \int_{-\infty}^{\infty} d\acute{x} G(\acute{x}, \omega) \int_{-\infty}^{\infty} e^{i\omega p(\acute{x}-x)} dp. \end{aligned} \tag{2.19}$$

Let rho, ρ , be a filter given by:

$$\rho(x, \omega) = \int_{-\infty}^{\infty} e^{-\omega p x} dp = \frac{2\pi}{|\omega|} \delta(x). \tag{2.20}$$

Replacing the ρ filter in Equation 2.19, the following convolution equation is obtained:

$$\begin{aligned} \hat{G}(x, \omega) &= \int_{-\infty}^{\infty} G(\acute{x}, \omega) \rho(x - \acute{x}, \omega) d\acute{x}, \\ &= G(x, \omega) * \rho(x, \omega). \end{aligned} \tag{2.21}$$

Further simplifying convolution model:

$$\hat{G}(x, \omega) = F(x, \omega) * \rho(x, \omega) = \frac{2\pi}{|\omega|} G(x, \omega), \quad (2.22)$$

$$G(x, \omega) = \frac{|\omega|}{2\pi} \hat{G}(x, \omega). \quad (2.23)$$

The final Radon transform equations for the forward slant stack Radon transform, as follow:

$$U(p, \omega) = \int_{-\infty}^{\infty} G(x, \omega) e^{i\omega p x} dx, \quad (2.24)$$

$$G(x, \omega) = \frac{|\omega|}{2\pi} \int_{-\infty}^{\infty} U(p, \omega) e^{-i\omega p x} dp. \quad (2.25)$$

But in practice, one does not have infinite p . For the finite p case, rho filter becomes

$$\rho(x, \omega) = \int_{P_{min}}^{P_{max}} e^{-\omega p x} dp = \begin{cases} \frac{1}{i\omega x} (e^{-i\omega P_{min} x} - e^{i\omega P_{max} x}) & \omega x \neq 0, \\ P_{max} - P_{min} & \omega x = 0. \end{cases} \quad (2.26)$$

Further simplifying:

$$\rho(x, \omega) = \begin{cases} 2P_{max} \frac{\sin(\omega P_{max} x)}{\omega P_{max} x} & \omega x \neq 0, \\ 2P_{max} & \omega x = 0. \end{cases} \quad (2.27)$$

Inverse slant stack

In 1994, the inverse slant stack operator was introduced by Zhou and Greenhalgh.

In the case of inverse slant stack transform, first the inverse τ - p transform is

applied, then for the proper inversion of the slant-stack forward transform is performed. Inverse slant stack using the same procedure as for forward slant stack is given by:

$$U(p, \omega) = \frac{|\omega|}{2\pi} \int_{-\infty}^{\infty} G(x, \omega) e^{i\omega px} dx, \quad (2.28)$$

$$G(x, \omega) = \int_{-\infty}^{\infty} U(p, \omega) e^{-i\omega px} dp. \quad (2.29)$$

Comparison

There is not much difference between the forward slant stack Radon transform and the inverse slant stack Radon transform. Deconvolution procedure is required in both cases. But the direction of the deconvolution is different in both the cases. In the case of Forward slant stack transform, the deconvolution is required to recover the data from the $\tau - p$ space and is performed on the inverse transform that is in the x-direction. On the other hand, in the inverse slant stack operator, the deconvolution process is required to estimate the $\tau - p$ space and is performed on the forward transform that is in p -direction. So to increase the resolution of $\tau - p$ domain inverse slant stack transform should be used.

2.5.2 Linear Radon transform of different curves

Point Source

A point source is modeled as a product of two delta functions. Initially, the point source is placed in the origin of the coordinate system:

$$g(x, t) = \delta(x)\delta(t), \quad (2.30)$$

$$u(p, \tau) = \int_{-\infty}^{\infty} \delta(x)\delta(px + \tau)dx = \delta(\tau). \quad (2.31)$$

By using the shifting property, above equation can be rewritten as:

$$g(x, t) = \delta(x - \acute{x})\delta(t - \acute{t}), \quad (2.32)$$

$$u(p, \tau) = \delta(\tau - \acute{t} + p\acute{x}), \quad (2.33)$$

$$g(x, t) = \int_{-\infty}^{\infty} \int_{-\infty}^{\infty} d(\acute{x}, \acute{t})\delta(x - \acute{x})\delta(t - \acute{t})d\acute{x}d\acute{t}. \quad (2.34)$$

By taking the Radon transform of the shifted point source, we obtain:

$$\begin{aligned} u(p, \tau) &= \int_{-\infty}^{\infty} \int_{-\infty}^{\infty} \int_{-\infty}^{\infty} d(\acute{x}, \acute{t})\delta(x - \acute{x})\delta(\tau - \acute{t} + px)d\acute{x}d\acute{t}dx, \\ &= \int_{-\infty}^{\infty} \int_{-\infty}^{\infty} d(\acute{x}, \acute{t})\delta(\acute{t} - \tau - p\acute{x})d\acute{x}d\acute{t}. \end{aligned} \quad (2.35)$$

This result shows that the point in $t - x$ domain will transform into an infinite line in the linear Radon domain.

Line

A line in terms of the δ can be represented by the following equation:

$$g(x, t) = \delta(t - \acute{p}x - \acute{\tau}). \quad (2.36)$$

The linear Radon transform of the line is given by:

$$\begin{aligned} u(p, \tau) &= \int_{-\infty}^{\infty} \int_{-\infty}^{\infty} \delta(t - \acute{p}x - \acute{\tau}) \delta(t - px - \tau) dx dy, \\ &= \int_{-\infty}^{\infty} \delta((p - \acute{p})x + \tau - \acute{\tau}) dx, \\ &= \begin{cases} \frac{1}{|p - \acute{p}|} & \text{for } p \neq \acute{p}, \\ 0 & \text{for } p = \acute{p} \text{ and } \tau \neq \acute{\tau}. \end{cases} \end{aligned} \quad (2.37)$$

The results shows that the Radon transform of a straight line will produce a single point in the $\tau - p$ domain.

Curve

For the following curve:

$$\tau = t - \phi(x), \quad (2.38)$$

the curvature can be found by using the following equations:

$$\psi(p, \tau; x) = t(x) - \phi(x) - \tau = 0, \quad (2.39)$$

$$\frac{\partial \psi(p, \tau; x)}{\partial x} = \frac{dt}{dx} - \frac{(d\phi(x))}{dx} = 0. \quad (2.40)$$

Travel time curves for seismic events are mostly hyperbolic in nature. Let the travel time curve be represented by:

$$t^2(x) = a + bx^2. \quad (2.41)$$

Taking the derivative of the above equation and using the Equations 2.39 and 2.40, we obtain:

$$\frac{dt}{dx} = p = \frac{bx}{t}, \quad (2.42)$$

$$\psi(p, \tau; x) = \sqrt{a + bx^2} - px - \tau = 0, \quad (2.43)$$

$$\frac{\partial\psi(p, \tau; x)}{\partial x} = \frac{bx}{t} - p = 0, \quad (2.44)$$

Now, our aim is to eliminate the x and τ . To achieve this, square the τ and substitute t form Equation 2.41.

$$\tau^2 = t^2 - 2ptx + p^2x^2, \quad (2.45)$$

or

$$\tau^2 = a + bx^2 + p^2x^2. \quad (2.46)$$

In the similar way, x can be eliminated by:

$$p = \frac{dt}{dx} = \frac{bx}{\sqrt{a + bx^2}}, \quad (2.47)$$

$$bx^2 = p^2(a + bx), \quad (2.48)$$

$$-p^2 \frac{a}{b} = x^2(p^2 - b). \quad (2.49)$$

Substituting this in Equation 2.46 will give us:

$$\frac{\tau^2}{a} + \frac{p^2}{b} = 1. \quad (2.50)$$

The above equation represents an ellipse. So an hyperbolic event in $t - x$ domain will transform in the ellipse into the $\tau - p$ domain.

2.6 Hyperbolic Radon transform

On common shot point gathers, seismic events are not linear in nature but they are hyperbolic in nature. Typically, refractions and direct waves are linear and reflections and diffractions are hyperbolic in nature. For the hyperbolic events, hyperbolic Radon transform can be used. The hyperbolic Radon transform maps the hyperbolic events of the common midpoint (CMP) gathers to points. But direct hyperbolic transforms are too expensive to realize due to their complexity. Therefore, hyperbolic Radon transform are not used in practice.

Thorson suggested a time domain hyperbolic least-squares method which can give a high resolution result at the expense of very large matrix computation. Mosher and Foster performed the hyperbolic Radon transform on normal move-out (NMO) corrected data, followed by frequency domain implementation of the hyperbolic Radon transform. To accommodate the shift in apex, apex shifted hyperbolic Radon transform was developed by Oppert and Brown (2002) [38].

Recently, a lot of research has been conducted for the fast computation of hyperbolic Radon transform [41–46].

Mathematically, in case of hyperbolic Radon transform we have

$$t = \sqrt{\tau^2 + qx^2}, \quad (2.51)$$

where $q = \frac{1}{v_{rms}^2}$ and v_{rms} is the root mean square velocity. Hyperbolic Radon transform in mathematical form is given by

$$u(q, \tau) = \sum_x g(x, t = \sqrt{\tau^2 + qx^2}). \quad (2.52)$$

2.6.1 NMO Corrected Radon transform

According to Mosher, to keep the computational cost low, the stacking surface should be time-invariant so that we can perform operations in frequency domain. Moreover the matrix operators should be in toeplitz form so we can use fast algorithm for matrix manipulation. We already have introduced the generalized Radon transform in time domain and frequency domain as:

$$u(q, \tau) = \sum_x g(x, t = \tau + q\phi(x)), \quad (2.53)$$

$$U(q, \omega) = \int_{-\infty}^{\infty} G(x, \omega) e^{i\omega q\phi(x)} dx, \quad (2.54)$$

Here g is the CMP shot gather, t is the two way time, u is transform domain, q is representing the curvature, and τ is the time intercept. Discrete frequency representation of the last equation is given by:

$$U(q_j, \omega) = \sum_{k=1}^N G(x_k, \omega) e^{i\omega q_j \phi(x_k)} \Delta x_k. \quad (2.55)$$

Mosher proposed the following phase shift factor:

$$\phi(x_k) = \sqrt{x_k^2 + z_{ref}^2} - z_{ref}, \quad (2.56)$$

where $x(k)$ is the offset receiver position, and the reference depth is defined by a constant parameter z_{ref} .

2.6.2 The Shifted-Hyperbolic Radon transform

A variant of the hyperbolic Radon transform was suggested by Castle and Malovichko. They proposed the shifted hyperbolic Radon transform with the following NMO equation:

$$t = \tau_s + \sqrt{\tau_0^2 + \frac{h^2}{v^2}}, \quad (2.57)$$

where

$$\tau_s = \tau_0 + (S - 1), \quad (2.58)$$

$$\tau_0 = \frac{t_0}{S}, \quad (2.59)$$

$$v^2 = SV_{rms}^2, \quad (2.60)$$

$$S = \frac{\mu_4}{\mu_2^2}, \quad (2.61)$$

$$\mu_n = \sum_{i=1}^N \Delta t_i V_i^n / \sum_{i=1}^N \Delta t_i. \quad (2.62)$$

The shifted-hyperbolic curve represents shifted Dix NMO equation (see Fig. 2.7).

$$t = t_0 + \sqrt{\frac{t_0^2 \mu_2^4}{\mu_4^2} + \frac{x^2 \mu_2^2}{\mu_4 V_{rms}^2}} - \frac{t_0^2 \mu_2^2}{\mu_4}, \quad (2.63)$$

or further simplifying:

$$t = t_0 - \frac{t_0}{S} + \sqrt{\frac{t_0^2}{S} + \frac{x^2}{S V_{rms}^2}}. \quad (2.64)$$

Figure 5.1 shows the application of hyperbolic Radon transform. The data is presented in Figure 5.1(a) and its hyperbolic Radon transform is presented in Figure 5.1(b). From the results, it is evident that the hyperbolic Radon transform provides best approximation for the seismic events.

2.7 Parabolic Radon transform

In parabolic Radon transform, a parabolic curve in time domain will be mapped to a single point in the $\tau - q$ or Radon domain. In case of the parabolic Radon transform the integral is taken along a parabolic curve. Hampson proposed an efficient frequency domain least-squares parabolic transform method [47]. The time domain semblance weighted Gauss-Seidel parabolic Radon transform was

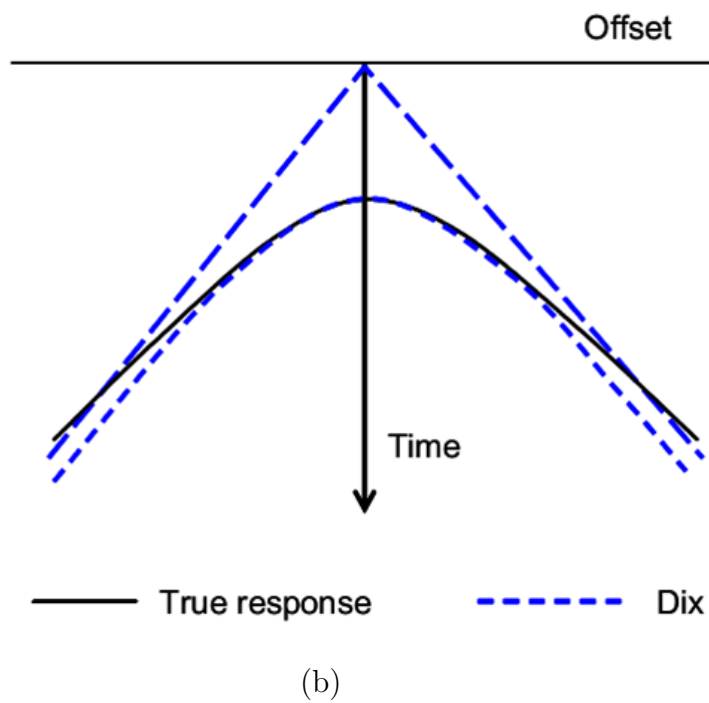
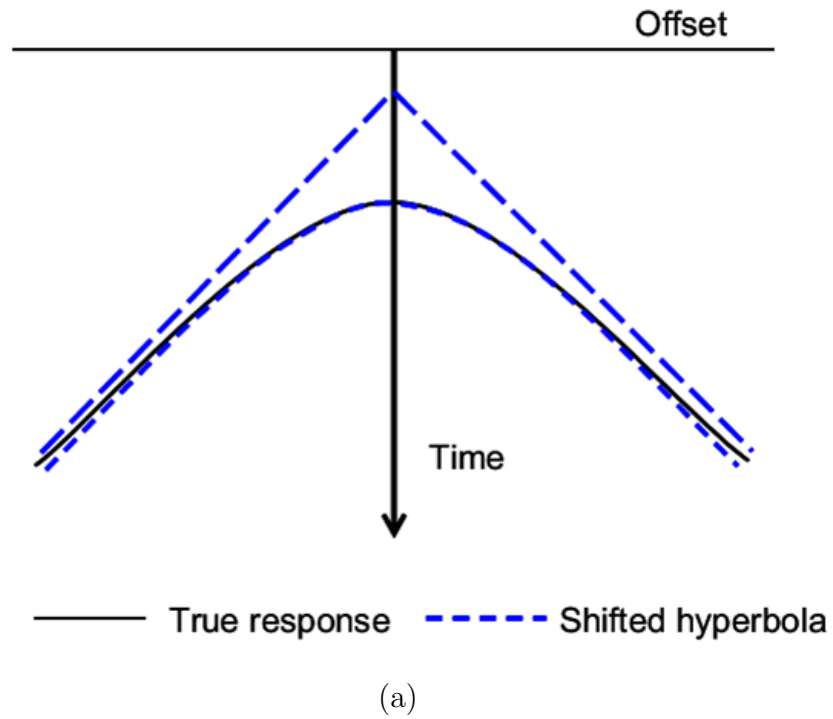
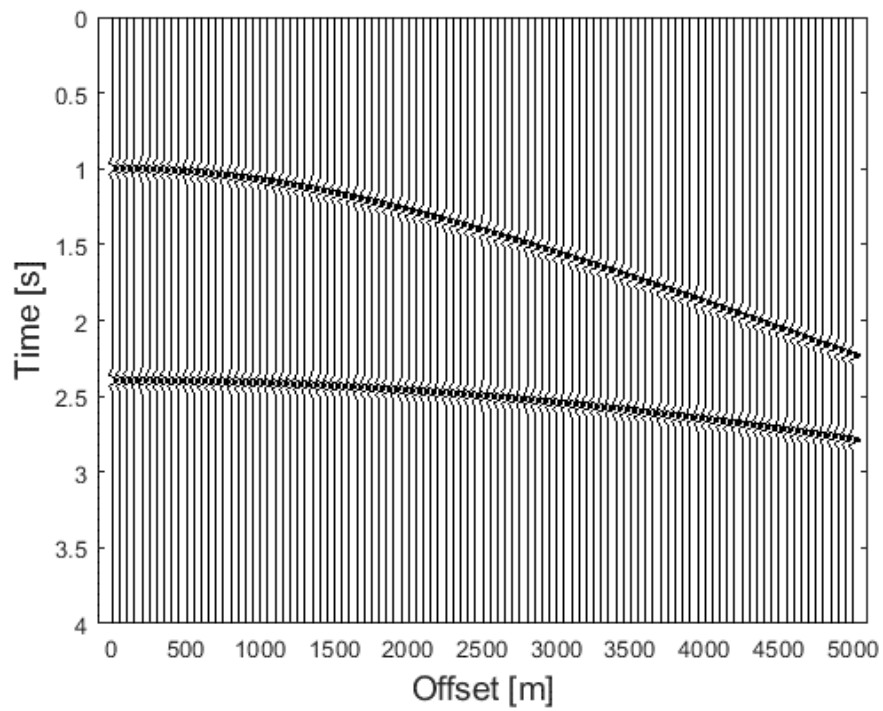
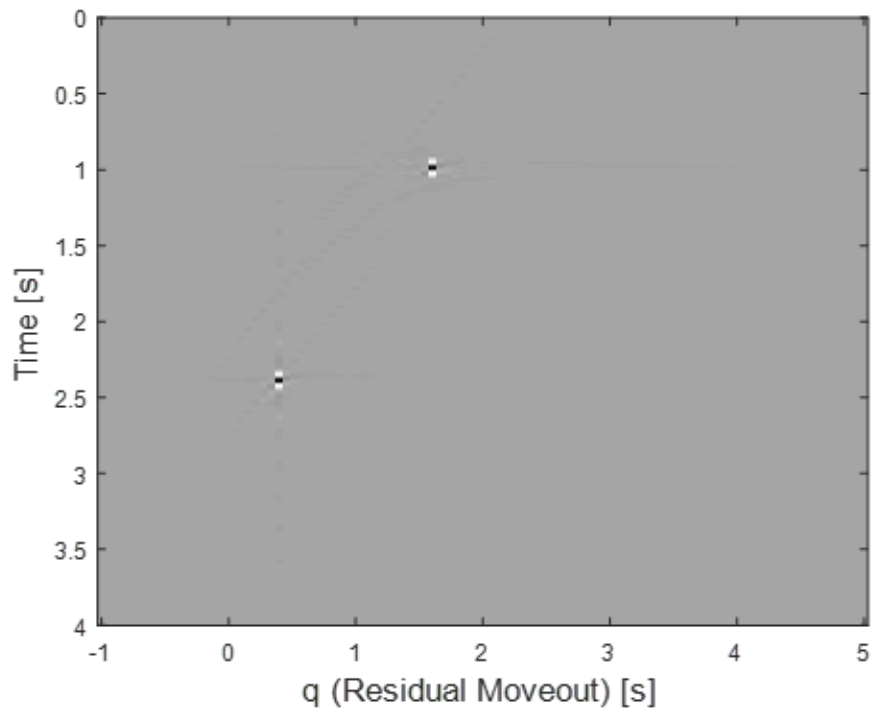


Figure 2.7: Hyperbola approximation using (a) shifted hyperbolic approximation and (b) Dix approximation.



(a)



(b)

Figure 2.8: (a) The synthetic seismic reflected data. (b) The hyperbolic Radon transform of (a).

proposed by Bradshaw [48]. The t^2 -stretching of the time axis was proposed by Yilmaz. The Hampson's frequency method was improved by Sacchi [26]. They incorporated the priori information for the formulation of High resolution parabolic Radon transform. Cary introduced the robust high-resolution parabolic Radon transform by posing the problem in the TX domain [24]. Sacchi and Porsani proposed a method to achieve an effective high-resolution Radon solution, by means of conjugate gradients. Trad proposed the robust high-resolution parabolic Radon by posing the problem in the FX domain [5,49]. Some variants of weighted Parabolic Radon transforms are discussed in [11, 21, 50, 51].

Mathematically, parabolic Radon transform can be obtained by substituting $\phi(x) = x^2$ in the generalized Radon transform Equation(2.10). The forward and inverse parabolic Radon transform become:

$$u(q, \tau) = \sum_x d(x, t = \tau + qx^2), \quad (2.65)$$

$$\hat{d}(x, t) = \sum_q u(q, \tau = t - qx^2), \quad (2.66)$$

where x is the offset and $q = 1/v^2$ represent the curvature of the curve.

2.7.1 Types of Parabolic Radon transform

Different types of parabolic Radon transform are discussed in this section.

Hampson parabolic Radon transform

In general, seismic events are hyperbolic in nature but we can approximate small portions of these events as parabolas. On the NMO-corrected data, the parabolic Radon transform was performed by Hampson [47]. Following Equation gives the hyperbolic move out of the NMO-corrected input data:

$$t_n = \sqrt{t^2 - \frac{x^2}{v_n^2}}, \quad (2.67)$$

where v_n is the corrected velocity, t is the recorded time, t_n is the corrected time. The resulting events can be approximated by parabolas. Squaring both sides of the above equation, we obtain the following equation:

$$t^2 = t_0^2 + \frac{x^2}{v^2}, \quad (2.68)$$

or in terms of error, we obtain:

$$t_{err}^2 = t_0^2 + \frac{x^2}{v_{err}^2}, \quad (2.69)$$

$$t_{err}^2 = t^2 + \frac{x^2}{v_{err}^2} - \frac{x^2}{v^2}, \quad (2.70)$$

$$\frac{t_{err}^2}{t^2} = 1 + \frac{x^2}{t^2} \left(\frac{1}{v_{err}^2} + \frac{1}{v^2} \right), \quad (2.71)$$

$$\frac{t_{err}}{t} = \sqrt{1 + \frac{x^2}{t^2} \left(\frac{1}{v_{err}^2} + \frac{1}{v^2} \right)}, \quad (2.72)$$

$$\frac{t_{err}}{t} \approx 1 + \frac{x^2}{2t^2} \left(\frac{1}{v_{err}^2} + \frac{1}{v^2} \right), \quad (2.73)$$

further simplifying, we obtain:

$$t = \tau + qx^2. \quad (2.74)$$

Parabolic Radon transform t^2 stretched input data

Yilmaz proposed that after application of the t^2 -stretch all the hyperbolic events in the time-offset domain can be transformed to exact parabolas [52]. Events on the CMP gather have hyperbolic travel times defined by:

$$t^2 = \tau^2 + \frac{x^2}{v^2}. \quad (2.75)$$

Applying $\tilde{t} = t^2$ and $\tilde{\tau} = \tau^2$, we obtain:

$$\tilde{t} = \tilde{\tau} + \frac{x^2}{v^2}. \quad (2.76)$$

Transformed equation is parabolic and can be defined as:

$$u(q, \tilde{\tau}) = \int_{-\infty}^{\infty} d(x, \tilde{t} = \tilde{\tau} + qx^2) dx, \quad (2.77)$$

$$\hat{d}(x, \tilde{t}) = \int_{-\infty}^{\infty} u(q, \tilde{\tau} = \tilde{t} - qx^2) dq. \quad (2.78)$$

Or in discrete form,

$$u(q, \tilde{\tau}) = \sum_x d(x, \tilde{t} = \tilde{\tau} + qx^2), \quad (2.79)$$

$$\hat{d}(x, \tilde{t}) = \sum_q u(q, \tilde{\tau} = \tilde{t} - qx^2). \quad (2.80)$$

2.7.2 Inverse Parabolic Radon

In the frequency domain, parabolic Radon transform can be represented as:

$$D(x, \omega) = \int_{-\infty}^{\infty} U(q, \omega) e^{-i\omega qx^2} dq, \quad (2.81)$$

$$\hat{U}(q, \omega) = \int_{-\infty}^{\infty} D(x, \omega) e^{i\omega qx^2} dx. \quad (2.82)$$

Replacing forward Radon transform into inverse Radon transform following equation is obtained:

$$\hat{U}(q, \omega) = \int_{-\infty}^{\infty} \int_{-\infty}^{\infty} U(\acute{q}, \omega) e^{-i\omega \acute{q}x^2} d\acute{q} e^{-i\omega qx^2} dx. \quad (2.83)$$

The above relation can be further simplified:

$$\hat{U}(q, \omega) = \int_{-\infty}^{\infty} \int_{-\infty}^{\infty} U(\acute{q}, \omega) e^{i\omega x^2(q-\acute{q})} d\acute{q} dx = \int_{-\infty}^{\infty} d\acute{q} U(\acute{q}, \omega) \int_{-\infty}^{\infty} e^{i\omega x^2(q-\acute{q})} dx. \quad (2.84)$$

Let $\sigma(q, \omega)$ be equal to $\int_{-\infty}^{\infty} e^{i\omega x^2(q-\acute{q})} dx$. Replacing the value of $\sigma(q, \omega)$ in above equation, following convolution equations are obtained:

$$\hat{U}(q, \omega) = U(q, \omega) * \sigma(q, \omega), \quad (2.85)$$

$$U(k_q, \omega) = \frac{\hat{U}(k_q, \omega)}{\sigma(k_q, \omega)} = \frac{\sqrt{\omega} \hat{U}(k_q, \omega)}{\hat{\sigma}(k_q)}. \quad (2.86)$$

$\sigma(q, \omega)$ can be simplified as:

$$\sigma(q, \omega) = [1 + i \operatorname{sign}(q)] \sqrt{\frac{\pi}{2\omega|q|}}, \quad (2.87)$$

$$U(k_q, \omega) = \frac{\sqrt{\omega k_p} \hat{U}(k_q, \omega)}{2\pi}. \quad (2.88)$$

Velocity-stack representation

Parabolic Radon transform in the velocity domain was introduced by Yilmaz [52].

$$u(v, \tau) = \sum_x d(x, t = \tau + 4\frac{x^2}{v^2}), \quad (2.89)$$

$$\hat{d}(x, t) = \sum_q u(v, \tau = t - 4\frac{x^2}{v^2}). \quad (2.90)$$

2.7.3 Parabolic Radon transform of different curves

The envelope of a certain curve ' C ' can be found by solving the set of equations:

$$\psi(p, \tau; x) = t(x) - \phi(x) - \tau = 0, \quad (2.91)$$

$$\frac{\partial \psi(p, \tau; x)}{\partial x} = \frac{dt}{dx} - \frac{d\phi(x)}{dx} = 0. \quad (2.92)$$

For Parabola $\phi(x) = qx^2$.

Point Source

Consider linear curve, 'C',

$$t(x) = \beta x, \quad (2.93)$$

$$\frac{dt}{dx} = \beta. \quad (2.94)$$

So a single point on C is represented as a line in the transform domain.

Parabolic Curve

Consider a parabolic curve 'q'. The curvature can be found by solving the Equation 2.91:

$$q = \frac{\beta}{2x}, \quad (2.95)$$

$$\tau = \frac{\beta x}{2}. \quad (2.96)$$

Eliminating x , we obtain:

$$q\tau = \frac{\beta^2}{4}. \quad (2.97)$$

The parabolic Radon transform of typical hyperbolic seismic events is given by:

$$t^2(x) = a + bx^2, \quad (2.98)$$

using previous equation, we get:

$$q(x) = \frac{b}{2t(x)}, \quad (2.99)$$

$$\tau(x) = \frac{t(x)}{2} + \frac{a}{2t(x)}, \quad (2.100)$$

eliminating $t(x)$, we get:

$$\tau = \frac{b}{4q} + \frac{aq}{b}, \quad (2.101)$$

Let $a = \frac{2h}{c}$ and $b = \frac{1}{c^2}$, we get:

$$ct^2 = x^2 + 2h^2, \quad (2.102)$$

$$\tau = \frac{1}{2c^2q}q + 2h^2q. \quad (2.103)$$

Curvature of the hyperbolic event is given by:

$$k(x) = \frac{\partial^2 t / \partial x^2}{(1 + (\partial t / \partial x)^2)^{3/2}} = \frac{dp(x)/dx}{1 + p^2(x)^{3/2}}, \quad (2.104)$$

$$dt/dx = p(x) = 2xq, \quad (2.105)$$

$$q_a = \frac{b}{2\sqrt{a}}, \quad (2.106)$$

$$\tau_a = \sqrt{a}, \quad (2.107)$$

$$K_a = \frac{d^2\tau}{dq^2|_a} = \frac{b}{2q_a^3} = \frac{\tau_a}{q_a^2} = \frac{4t(0)}{K^2(0)}. \quad (2.108)$$

So a parabolic curve C is represented as a point in the transform domain.

2.8 Conclusion

In this chapter, the theory of generalized Radon transform and its applications have been presented. Different types of Radon transform that are used for seismic data processing have been covered with different examples. Through proper mathematical derivations it is shown that $\tau - p$ and $\tau - q$ domain provides sparse representation of the linear and parabolic (or hyperbolic) seismic events, respectively. Furthermore, it has been shown that hyperbolic Radon transform is best suited for seismic data processing, however, due to large computational costs, it is not feasible.

CHAPTER 3

ANGLE BASED RADON TRANSFORM

Radon transform is the part of the seismic processing workflow for last three decades and as the amount of acquired data is increasing, therefore, there is a need for robust, efficient, high-resolution Radon transform, which can be computed efficiently. This chapter presents a new angle-based 3-D Radon transform that results in a high-resolution Radon transform. The proposed transform introduces a new angle-based parameter to the existing Radon transform, which produces high-resolution Radon transform. To prove the concept, the newly proposed method has been applied for the interpolation and attenuation of multiple reflections from the recorded seismic data. The angle-based Radon transform is robust under the noisy condition and has been tested on synthetic and real seismic data set, with various levels of additive white Gaussian noise. Furthermore, it has been compared with existing methods for low as well as high Radon transforms.

In contrast to existing methods, the proposed method produces high-resolution Radon transform without the need of normal move-out correction and works for far offset.

In the first two sections of this chapter, the proposed method along with the mathematical theory is presented. In the third section of the chapter, the application of the proposed method is presented and compared with the existing technique. It is followed by the section discussing the interpolation of missing seismic traces, along with the application of the proposed transform on 2-D and 3-D seismic data. The last section of the chapter presents the application of the proposed method for the multiplication removal of the seismic data.

3.1 Introduction

As described in Chapter 2, although there are many different types of Radon transform that are used for seismic data processing, they can be classified into linear Radon transform, the hyperbolic Radon transform, and the parabolic Radon transform [5]. Since, seismic events are hyperbolic in nature, therefore, hyperbolic Radon transform is the one that produces high resolution Radon transform, however, it is computationally expensive and there is a need for fast, robust, efficient Radon transform which can be used for 2-D and 3-D seismic data.

Let $g(x, t)$ represent the seismic data in offset ' x ' and time ' t '. Then, the Generalized Radon Transform [35] pair for this seismic data $g(x, t)$ is given as

following:

$$u(q, \tau) = \int_{-\infty}^{\infty} g(x, t = \phi(x; q, \tau)) dx, \quad (3.1)$$

$$\hat{g}(x, t) = \int_{-\infty}^{\infty} u(q, \tau = \phi(q; x, t)) dq, \quad (3.2)$$

where q and τ are representing some parameter of the curve. Similarly, $\phi(\cdot)$ is the function of the offset parameter 'x' and depend on the path of integration. Depending upon the type of Radon transform the $\phi(x; q, \tau)$ has value $\tau + px$, $\tau + qx^2$, and $\sqrt{\tau^2 + qx^2}$ for linear, parabolic and hyperbolic Radon transform, respectively. Similarly, $\phi(q; x, t)$ has value $t - px$, $t - qx^2$, and $\sqrt{t^2 - qx^2}$ for linear, parabolic and hyperbolic Radon transform, respectively.

Similarly, in discrete form, Radon transform is represented as:

$$u(q, \tau) = \sum_x g(x, t = \phi(x; q, \tau)), \quad (3.3)$$

$$\hat{g}(x, t) = \sum_q u(q, \tau = \phi(q; x, t)). \quad (3.4)$$

In the discrete frequency domain, for different values of the angular frequency ω , the parabolic Radon transform $g_p(q, \omega)$ for seismic data $g(x_n, \omega)$ can be represented as follows [5]:

$$g_p(q, \omega) = \sum_{n=1}^N g(x_n, \omega) e^{i\omega q x_n^2}, \quad (3.5)$$

where x_n represents the offset position.

Similarly, the linear Radon transform which transforms the data from (x, t) to

the linear Radon domain $g_l(p, \omega)$ is represented as follows [5]:

$$g_l(p, \omega) = \sum_{n=1}^N g(x_n, \omega) e^{i\omega p x_n}. \quad (3.6)$$

Representing Equations (3.5) and (3.6) in algebraic form results, respectively, in the following equations:

$$\mathbf{g}_p = \begin{bmatrix} e^{i\omega q_1 x_1^2} & e^{i\omega q_2 x_1^2} & \dots & e^{i\omega q_N x_1^2} \\ e^{i\omega q_1 x_2^2} & e^{i\omega q_2 x_2^2} & \dots & e^{i\omega q_N x_2^2} \\ \vdots & \vdots & \vdots & \vdots \\ e^{i\omega q_1 x_N^2} & e^{i\omega q_2 x_N^2} & \dots & e^{i\omega q_N x_N^2} \end{bmatrix} \begin{bmatrix} s_1 \\ s_2 \\ \vdots \\ s_N \end{bmatrix}, \quad (3.7)$$

and

$$\mathbf{g}_l = \begin{bmatrix} e^{i\omega p_1 x_1} & e^{i\omega p_2 x_1} & \dots & e^{i\omega p_N x_1} \\ e^{i\omega p_1 x_2} & e^{i\omega p_2 x_2} & \dots & e^{i\omega p_N x_2} \\ \vdots & \vdots & \vdots & \vdots \\ e^{i\omega p_1 x_N} & e^{i\omega p_2 x_N} & \dots & e^{i\omega p_N x_N} \end{bmatrix} \begin{bmatrix} s_1 \\ s_2 \\ \vdots \\ s_N \end{bmatrix}, \quad (3.8)$$

where $s_n = g(x_n, \omega)$.

The Radon transform can be posed as an inverse problem and based on the inversion theory [30], the Radon domain has higher resolution by first defining the inverse transform and then deriving the forward transform. The inverse Radon transform can be written in matrix form as:

$$\mathbf{g} = \mathbf{L}\mathbf{u}, \quad (3.9)$$

where \mathbf{g} is the data, \mathbf{L} is the Radon transform operator, and \mathbf{u} is the Radon model. Similarly, the forward operator can be described as:

$$\hat{\mathbf{u}} = \mathbf{L}^T \mathbf{g}, \quad (3.10)$$

The estimated model $\hat{\mathbf{m}}$ and the original model \mathbf{m} are clearly not identical because Radon transforms are not an orthogonal transformations. The estimation of the Radon model must then be posed as an inversion problem conditioned by a regularization (penalty) term. The general form of the cost function, J , to be minimized to obtain sparse Radon coefficients is given by:

$$J = \|\mathbf{g} - \mathbf{L}\mathbf{m}\|_2^2 + \mu\|\mathbf{m}\|_1, \quad (3.11)$$

where, μ is the trade-off parameter.

Although expressed in the frequency domain, the concept may also be applied in the time domain as described by Trad et al. [5]. However, in time domain case the problem becomes much larger because instead of solving a small least squares problem for each frequency slice, separately, we solve for the full $\tau - q$ or $\tau - p$ model in one iteration. One more problem with the $\tau - q$ or $\tau - p$ transform is that its basis is not orthogonal. As a result, it requires a large p -range and small p -increment (i.e., the model space is large, especially for high dimensions) to represent the input data accurately. Also, instead of utilizing the $\tau - q$ or $\tau - p$, angle can be utilized to improve the resolution of the transform. By combining

the above facts, a 3-D Radon transform has been presented which produces high resolution results and computationally efficient.

3.2 Mathematical Formulation

A typical travel time curve is represented by following equation:

$$t = \sqrt{t^2 + (x_s - x_d)^2/v^2} + \sqrt{t_d^2 + (x_d - x_r)^2/v^2}, \quad (3.12)$$

where t_d is the travel time, x_d is the diffraction location, x_s and x_r are the locations of sources and receiver, respectively.

As Equation 3.12 shows that the travel time curve is considered as a hyperbolic curve, therefore, hyperbolic Radon transform produces the high resolution Radon transform with better focusing of the non-linear seismic events. However, it will require to integrate over three different parameters and if size of the parameter is N then the complexity of the single iteration of the hyperbolic Radon transform will be $O(N^3)$. Due to the large size of the seismic data it is not feasible to perform the integration or invert the matrices. To reduce the search space and provide better focusing power than the linear and parabolic Radon transform, an additional parameter θ is introduced in the conventional Radon transform and two separate operators are used to enhance the focusing of the parabolic Radon transform.

The first operator is the same as used in the traditional Radon transform and

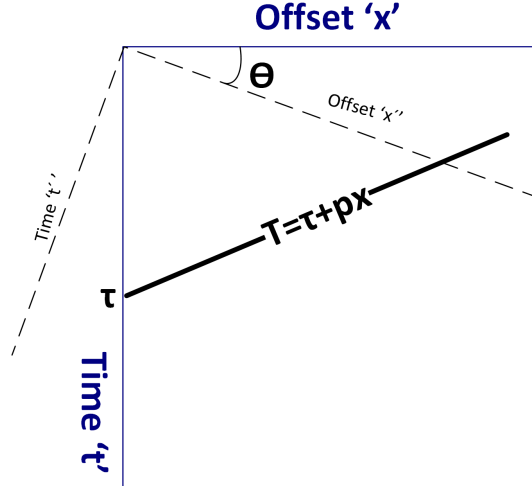


Figure 3.1: Representation of line in term of θ .

it is given by:

$$u_1(q, \tau) = \int_{-\infty}^{\infty} g(x, \Phi(t)) dx. \quad (3.13)$$

For the second operator consider the fact that a line can be represented in terms of angle θ and normal to line 'r'. By considering the Figure 3.1, one can write the line in following mathematical expression:

$$r = x \cos \theta + t \sin \theta. \quad (3.14)$$

Another way of representing the line is presented in Figure 3.1, based on which the Radon transform is given by:

$$u_2(\theta) = \int_{-\infty}^{\infty} g(\acute{x} \cos \theta - \acute{t} \sin \theta, \acute{x} \sin \theta + \acute{t} \cos \theta) d\acute{t}, \quad (3.15)$$

where

$$\begin{bmatrix} \acute{x} \\ \acute{t} \end{bmatrix} = \begin{bmatrix} \cos \theta & \sin \theta \\ -\sin \theta & \cos \theta \end{bmatrix} \begin{bmatrix} x \\ t \end{bmatrix}. \quad (3.16)$$

Collectively, both these operators can be combined together as a double integral as presented in equation below:

$$u(q, \tau, \theta) = \int_0^\pi \int_{-\infty}^\infty g(x, t) dx d\theta, \quad (3.17)$$

$$\hat{g}(x, t) = \int_0^\pi \int_{-\infty}^\infty u(q, \tau, \theta) dq d\theta. \quad (3.18)$$

The above two equations describe the angle based Radon transform in continuous time domain. For the calculation of the angle based Radon transform the integration is performed along the different angles as presented in Figure 3.1. The discrete version of the above transform can be obtained from the following equation pair:

$$u(q, \tau, \theta) = \sum_{\theta} \sum_x g(x, t), \quad (3.19)$$

$$\hat{g}(x, t) = \sum_{\theta} \sum_q u(q, \tau). \quad (3.20)$$

3.2.1 3-D angle based Radon Transform

The angel based Radon transform (Equations 3.17 - 3.20) can be expanded to 3-D seismic data by integrating over the in-line and cross-line Radon domains. The

3-D traditional Radon transform is presented in Equations 3.21 and 3.22.

$$u_1(q_x, q_y, \tau) = \int_{-\infty}^{\infty} dx \int_{-\infty}^{\infty} g(x, y, t = \tau + q_x\phi(x) + q_y\phi(y)) dy, \quad (3.21)$$

$$\hat{g}(x, y, t) = \int_{-\infty}^{\infty} dq_x \int_{-\infty}^{\infty} u(q_x, q_y, \tau = t - q_x\phi(x) - q_y\phi(y)) dq_y. \quad (3.22)$$

Here, x, y represent the in-line and cross-line dimensions of the 3-D seismic data, respectively. The curve parameters for the in-line and cross-line dimensions are represented by q_x and q_y , respectively. Similarly, the discrete version of the above 3-D Radon transform are as follows:

$$u_1(q_x, q_y, \tau) = \sum_x \sum_y g(x, y, t = \tau + q_x\phi(x) + q_y\phi(y)), \quad (3.23)$$

$$\hat{g}(x, t) = \sum_{q_x} \sum_{q_y} u(q_x, q_y, \tau = t - q_x\phi(x) - q_y\phi(y)). \quad (3.24)$$

As for the 2-D angle based Radon transform, we can introduce new operator for each in-line and cross-line direction. Let θ_x and θ_y be the angular parameter for the in-line and cross-line dimensions, respectively. Based on these parameters the 3-D Radon transform can be obtained via following integrals:

$$u_{2_a}(\theta_x) = \int_{-\infty}^{\infty} g(\acute{x} \cos \theta_x - \acute{t} \sin \theta_x, \acute{x} \sin \theta_x + \acute{t} \cos \theta_x) d\acute{t},$$

where

$$\begin{bmatrix} \acute{x} \\ \acute{t} \end{bmatrix} = \begin{bmatrix} \cos \theta & \sin \theta \\ -\sin \theta & \cos \theta \end{bmatrix} \begin{bmatrix} x \\ t \end{bmatrix}. \quad (3.25)$$

Likewise, for cross-line:

$$u_{2_a}(\theta_y) = \int_{-\infty}^{\infty} g(\acute{y} \cos \theta_y - \acute{t} \sin \theta_y, \acute{y} \sin \theta_y + \acute{t} \cos \theta_y) d\acute{t}, \quad (3.26)$$

$$\begin{bmatrix} \acute{y} \\ \acute{t} \end{bmatrix} = \begin{bmatrix} \cos \theta & \sin \theta \\ -\sin \theta & \cos \theta \end{bmatrix} \begin{bmatrix} y \\ t \end{bmatrix}. \quad (3.27)$$

Now, combining both these operators, we have

$$u(q_x, q_y, \tau, \theta_x, \theta_y) = \int_0^\pi \int_0^\pi \int_{-\infty}^{\infty} \int_{-\infty}^{\infty} g(x, y, t) dx dy d\theta_x d\theta_y, \quad (3.28)$$

$$\hat{g}(x, y, t) = \int_0^\pi \int_0^\pi \int_{-\infty}^{\infty} \int_{-\infty}^{\infty} u(q, \tau, \theta) dq_x dq_y d\theta_x d\theta_y. \quad (3.29)$$

Now, for the discrete case

$$u(q_x, q_y, \tau, \theta_x, \theta_y) = \sum_{\theta_x} \sum_{\theta_y} \sum_y \sum_x g(x, t), \quad (3.30)$$

$$\hat{g}(x, y, t) = \sum_{\theta_x} \sum_{\theta_y} \sum_{q_x} \sum_{q_y} u(q, \tau). \quad (3.31)$$

3.3 Application

For parabolic Radon transform, the angle-based Radon transform can be simplified as follows:

$$u_1(q, \tau) = \sum_x g(x, t = \tau + qx^2), \quad (3.32)$$

$$u_2(\theta) = \sum_\theta g(x, t), \quad (3.33)$$

3.3.1 Performance Metrics

For testing and comparison following performance parameters were used:

- To test the efficiency of the proposed algorithm, it was compared with existing methods for Radon transforms. The comparison was performed with both low-resolution and fast high-resolution Radon transforms. For the low-resolution Radon transform, the least squares method [20] (solved by a Levinson solver) was used. Similarly, for the high-resolution Radon transform, complex gradient methods with fast Fourier transform (CG-FFT) was utilized [5, 26].
- To test the robustness of the proposed method, different level of noise was added. The term robustness is used for the effect of noise on the performance of the transform. In plain words, the transform is said to be robust in nature, if it works for a high level of noise. Similarly, by noise level, it means that the percentage of noise as compared to the peak seismic trace value.
- To compare the accuracy of the proposed method the original synthetic data was compared quantitatively with, the proposed and existing methods of Radon transforms. Mean square error (MSE) was used to assess the performance of the proposed algorithm. MSE estimates the error between the original data and the recovered seismic data.

3.3.2 Synthetic Data

For testing, the seismic synthetic data was generated using a Ricker wavelet of 10 Hz and two reflection events (see Figure 3.2(a)). The total number of traces in the data were 101 with spatial sampling interval 75 *m* and sampling interval 4 *ms*. Radon transform domain for angle-based Radon transform formulation as proposed in the previous section, is presented in Figure 3.2(b), where both reflection events have been compressed into two single points. From the Figure 3.2(b) it is evident that the angle based Radon transform produces high-resolution Radon domain without the need of normal moveout correction as required for the traditional Radon transform. Inverse parabolic Radon transform was used to convert data from the angle-based Radon domain to the time-offset domain and result is shown in Figure 3.2(c).

Comparison with Existing Methods:

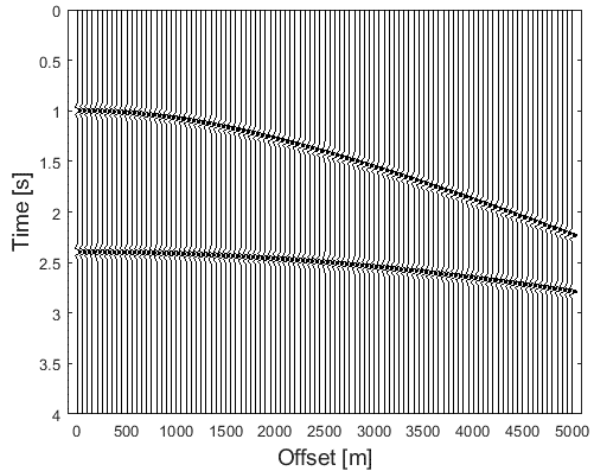
To test the efficiency of the proposed algorithm, it was compared with both low-resolution and fast high-resolution Radon transforms. Figures 3.3(a) and 3.3(b) shows the original data and data after NMO correction with muting, which is essential for the parabolic Radon transform. High resolution Radon domain for CG-FFT is presented in Figure 3.3(c) which shows that the events are mapped as points in the transformed domain. Finally, the data after the inverse parabolic Radon transform is presented in Figure 3.3(d) and after the NMO correction is represented in Figure 3.3(e). Similar result for low-resolution Radon transform is presented in Figure 3.4. From Figure 3.4(c), it is evident that resolution of

the low-resolution Radon transform is low, however, due to the simplicity of the data the recovered data (Figure 3.4(e)) is almost identical to the high resolution Radon transform (Figure 3.3(e)). Furthermore, to make the computational cost low, only three iterations of the CG-FFT based high resolution Radon transform were computed.

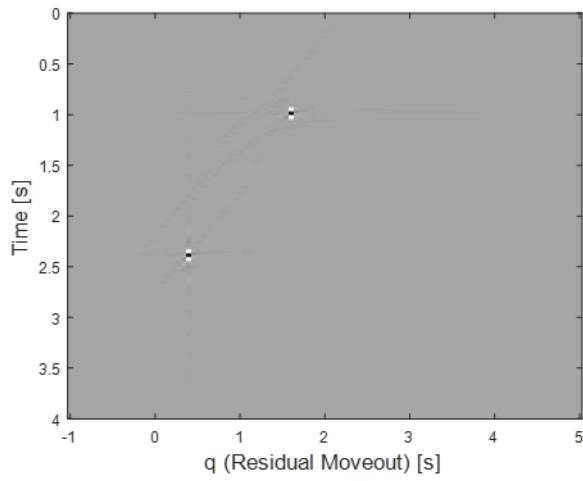
Noise Analysis:

To test the robustness of the proposed setup, data with different noise level is tested. The results after the addition of the noise with 0.1 standard deviation are presented in Figure 3.5. The Figure 3.5(a) present the data after addition of the Gaussian noise with 10% noise. Figures 3.5(b)-(c) presents the angle based Radon domain and its inverse. The comparison for the existing high resolution Radon transform in Figure 3.6, which also produces almost perfect reconstruction with first applying the NMO.

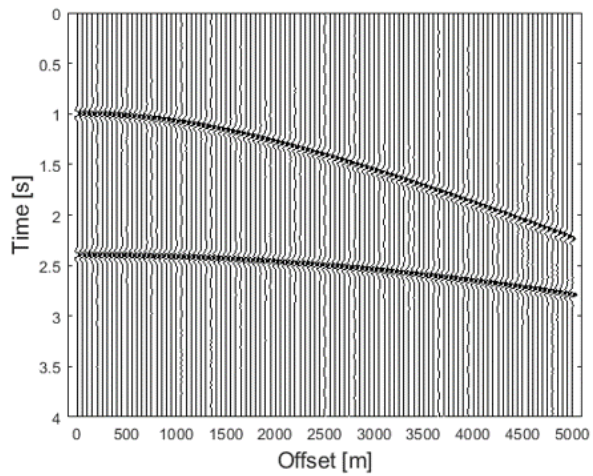
To further test the effect of noise the proposed algorithm was also tested with more noise level. Figure 3.7 presents the result after the addition of 20 % noise. Once again the results are as expected with high resolution Radon transform. Similarly, Figure 3.8 shows the result for the 40% noise. In that case, even it is very difficult to see the data, however, the angle-based Radon transform produces high resolution results. It is evident from the Figures 3.5-3.8 that the proposed angle-based Radon transform is robust in nature and even works for high levels of noise.



(a)



(b)



(c)

Figure 3.2: (a) The synthetic seismic reflected data. (b) The angle based Radon transform of (a). (c) The data after the application of inverse Radon transform.

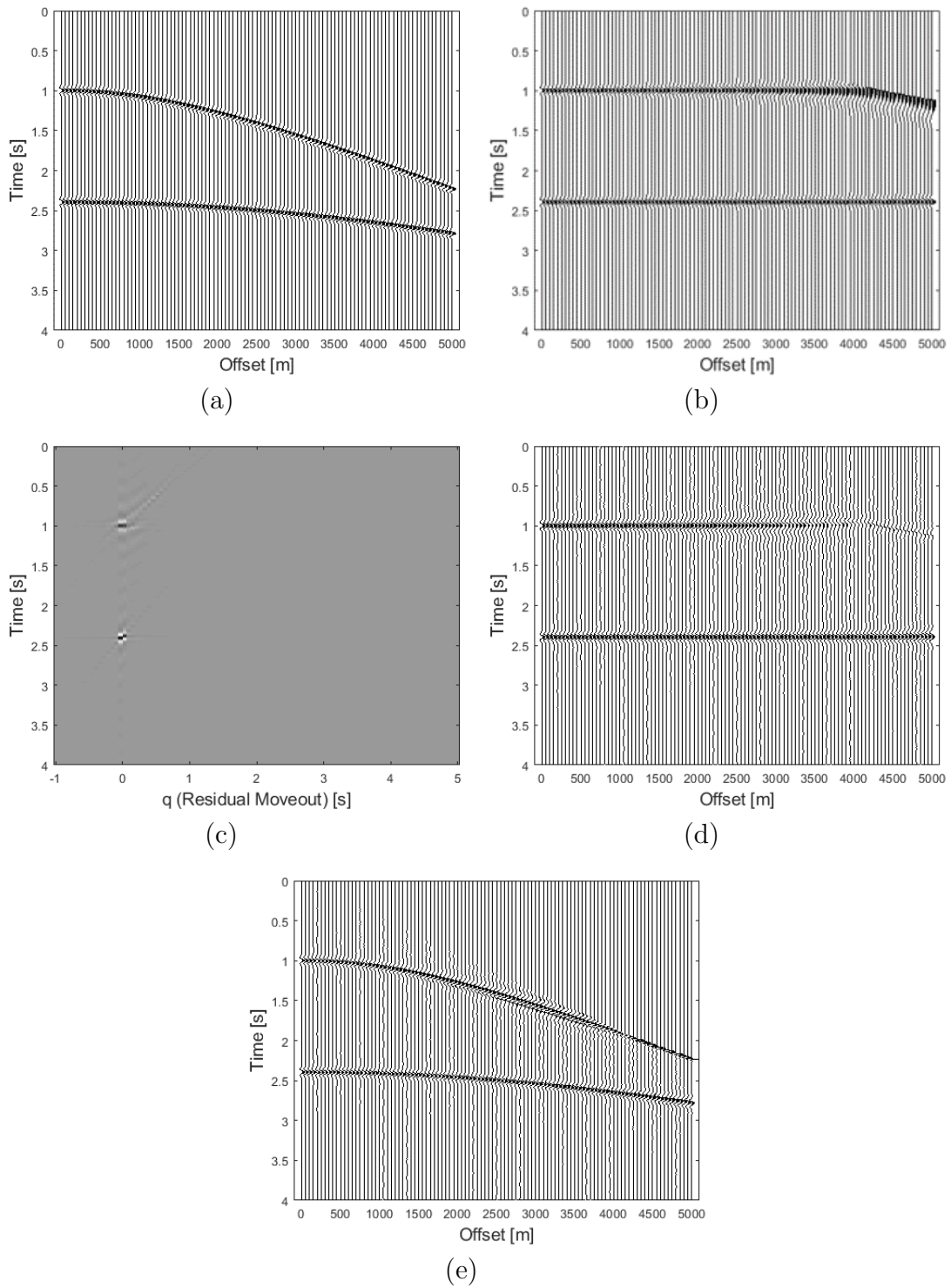


Figure 3.3: (a) The synthetic seismic reflected data. (b) The NMO corrected data. (c) The CG-FFT based Radon transform of (b). (d) The data after the application of inverse Radon transform and (e) after performing the NMO correction.

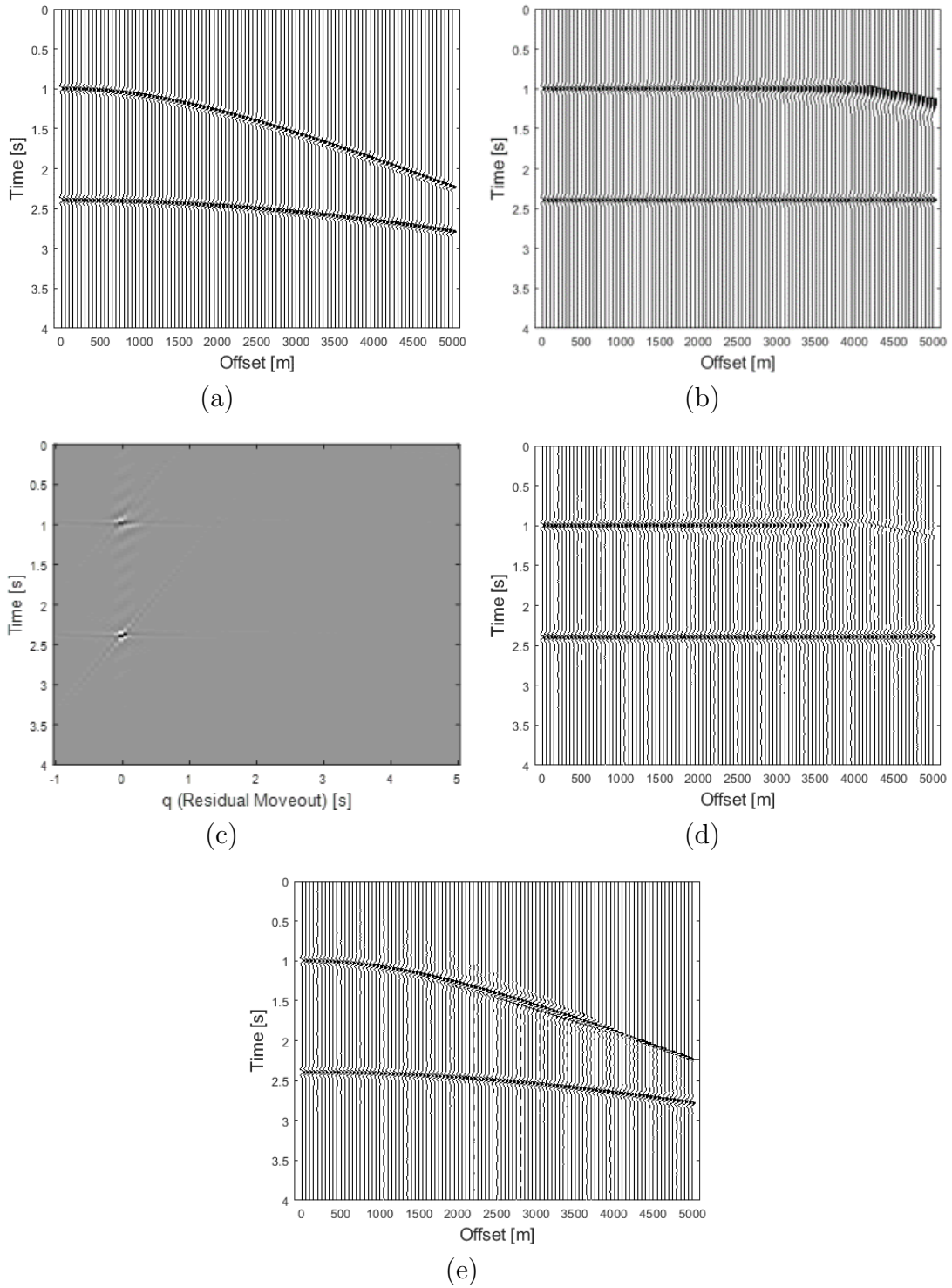
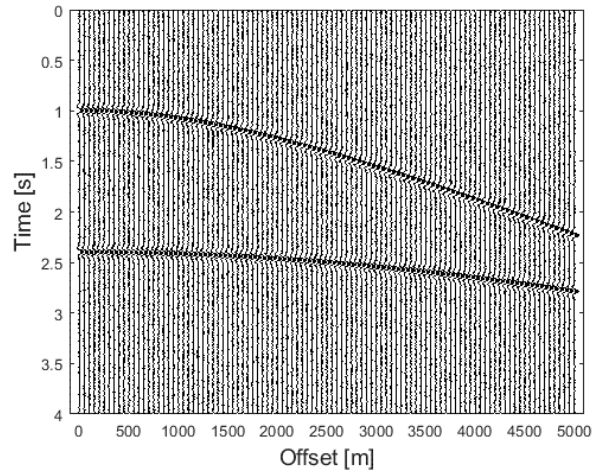
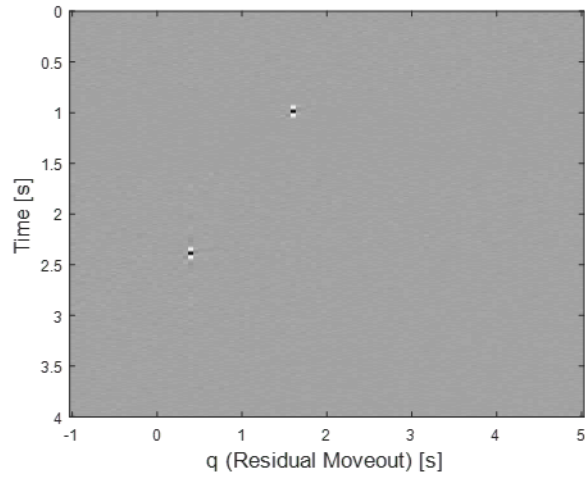


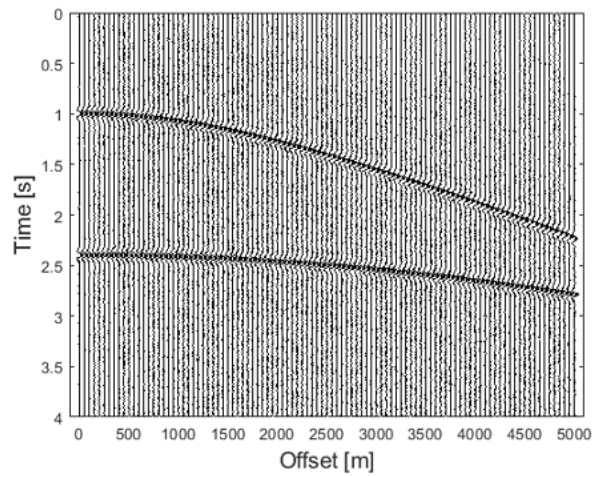
Figure 3.4: (a) The synthetic seismic reflected data. (b) The NMO corrected data. (c) The Least square based Radon transform of (b). (d) The data after the application of inverse Radon transform and (e) after performing the NMO correction.



(a)

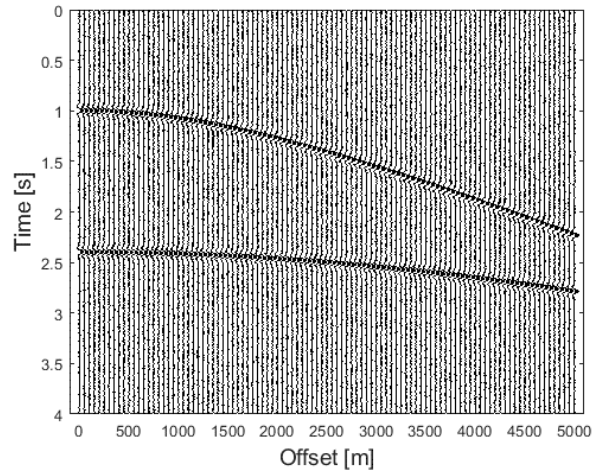


(b)

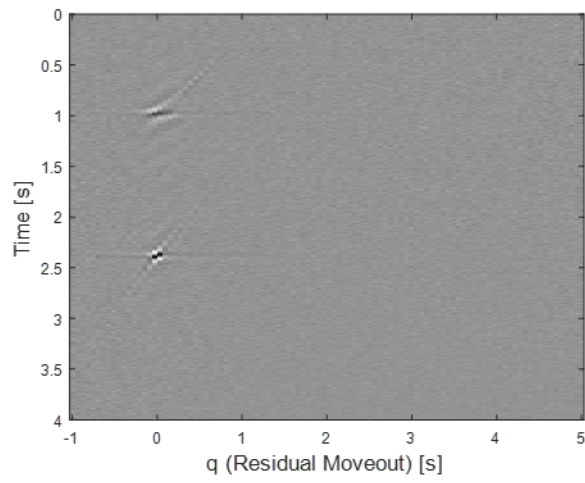


(c)

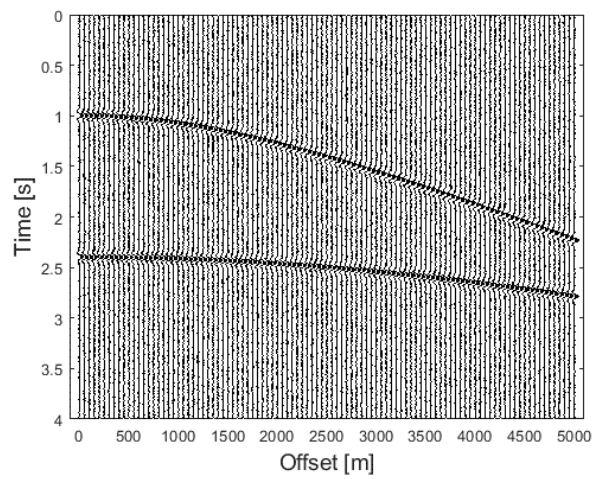
Figure 3.5: (a) The synthetic seismic reflected data with 10% Noise. (b) The angle based Radon transform of (a). (c) The data after the application of inverse Radon transform.



(a)

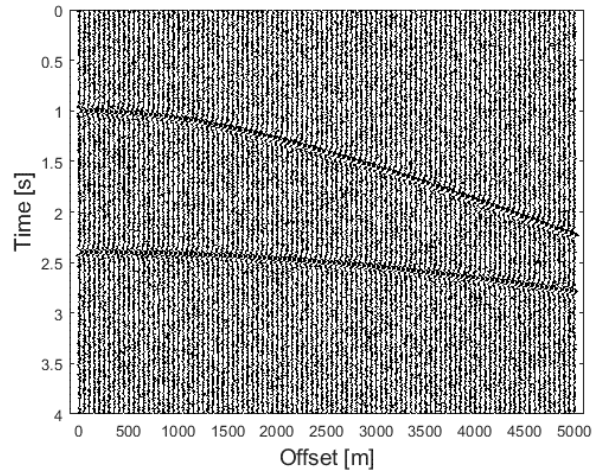


(b)

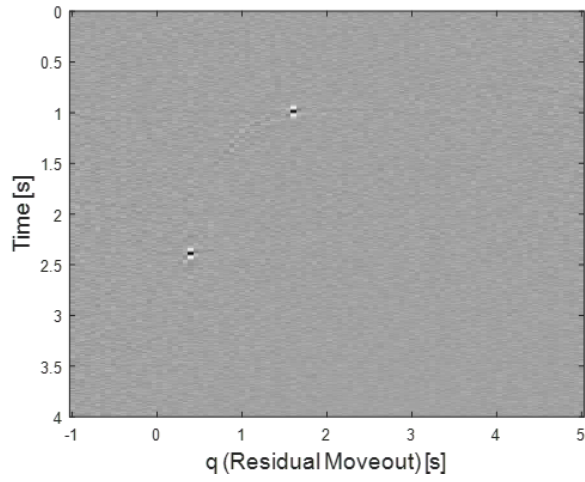


(c)

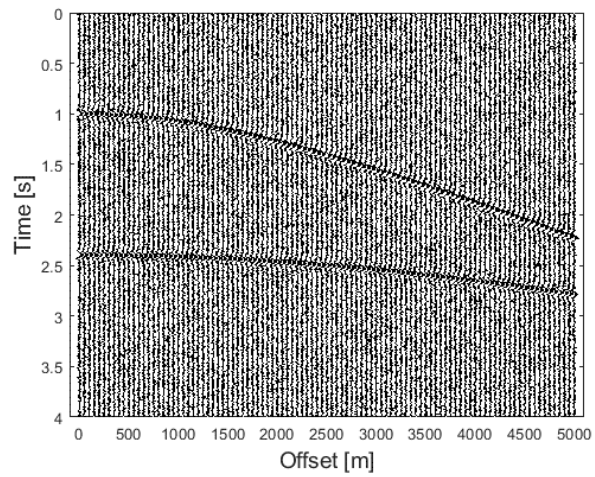
Figure 3.6: (a) The synthetic seismic reflected data with 10% Noise. (b) The CG based Radon transform of (a). (c) The data after the application of inverse Radon transform.



(a)

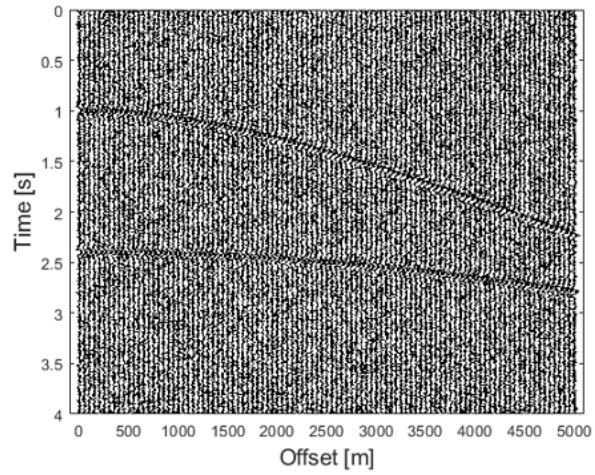


(b)

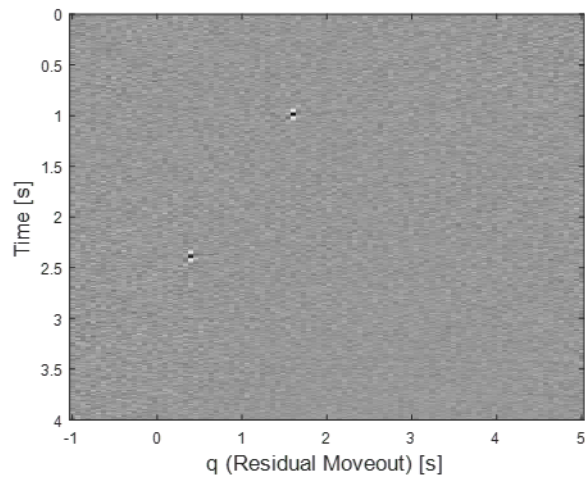


(c)

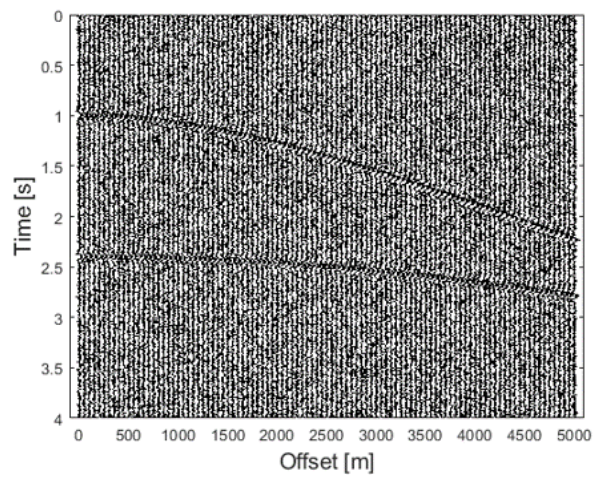
Figure 3.7: (a) The synthetic seismic reflected data with 20% Noise. (b) The angle based Radon transform of (a). (c) The data after the application of inverse Radon transform.



(a)



(b)



(c)

Figure 3.8: (a) The synthetic seismic reflected data with 40% Noise. (b) The angle based Radon transform of (a). (c) The data after the application of inverse Radon transform.

Table 3.1: Mean squared error for the angle-based Radon transform method versus other Radon transform methods for Figure 3.2a.

Method	Noise	MSE
Angle-based Radon transform	-	0.0053
Low-resolution Radon transform (Levinson, Least Squares)	-	0.0075
Fast high-resolution Radon transform (CG-FFT)	-	0.0068
Angle-based Radon transform	10%	0.0055
Low-resolution Radon transform (Levinson, Least Squares)	10%	0.0084
Fast high-resolution Radon transform (CG-FFT)	10%	0.0071
Angle-based Radon transform	30%	0.0054
Low-resolution Radon transform (Levinson, Least Squares)	30%	0.013
Fast high-resolution Radon transform (CG-FFT)	30%	0.0073

Quantitative Analysis:

To compare the accuracy of the proposed method, the original data (Figure 3.2(a)) was compared quantitatively with the proposed and existing methods of Radon transforms. The results are summarized in Table 3.1, which presents the mean squared error (MSE). From Table 3.1, it is evident that the results for the proposed method are more accurate than those of existing methods for Radon transforms and are comparable to the high-resolution Radon transform.

The proposed method is, in general, more accurate than the existing techniques. Besides its accuracy, another advantage is the removal of pre-processing and post processing steps of normal move-out and inverse normal move-out correction.

3.4 Interpolation of Missing Seismic Events

Interpolation/reconstruction of missing seismic traces is one of the most key pre-processing steps, whereby the resolution of the data is increased. During the last a few years, the demand for denser seismic traces has significantly increased. In most cases, due to the certain limitations of hardware, budgets, and computing power, it is not possible to collect large samples of seismic traces. Sometimes, due to poor conditions or the topological structures of the Earth's surface, it is not possible to place seismic sensors (geophones) resulting in missing traces in the acquired data. Thus, reducing the amount of acquired data, as well as effective reconstruction of complete seismic data from acquired incomplete seismic data, are very important issues.

Most famous methods are based on transformation of seismic data into sparse domain by using transforms like wavelet, Radon, or curvelet as discussed in [5, 53, 54]. Similarly, there are some techniques based on filters as discussed in [55]. Low rank-based interpolation is presented in [56]. Energy of the primary reflections can also be used for the interpolation as discussed in [57]. The same energy concept is extended in [58]. Interferometric interpolation of missing seismic data is discussed in [59]. Compressive sensing-based interpolation, using the curvelet transform, are presented in [60, 61]. Recently, a new technique based on the weighted l_1 -norm minimization was proposed in [62].

Here, a technique for the interpolation of missing seismic traces, based on angle based high resolution Radon transform, is presented.

Algorithm

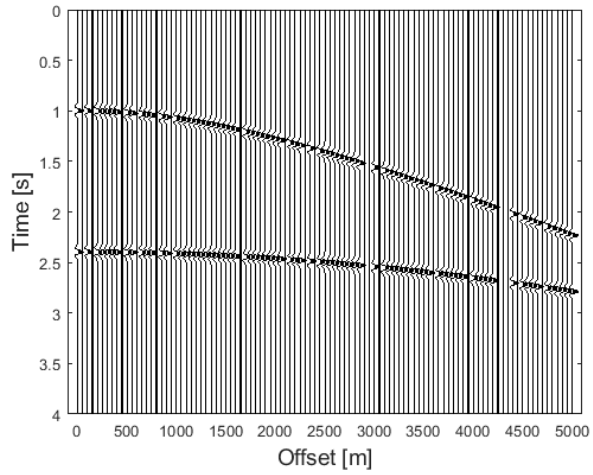
Given a seismic record, the proposed algorithm for interpolation of missing seismic traces is stated as follows:

1. Use the angle based Radon transform as described previously in this chapter to obtain the Radon domain.
2. Apply the inverse linear Radon transform to the previous step result.
3. Repeat the step 1-2 depending upon the complexity of the data.

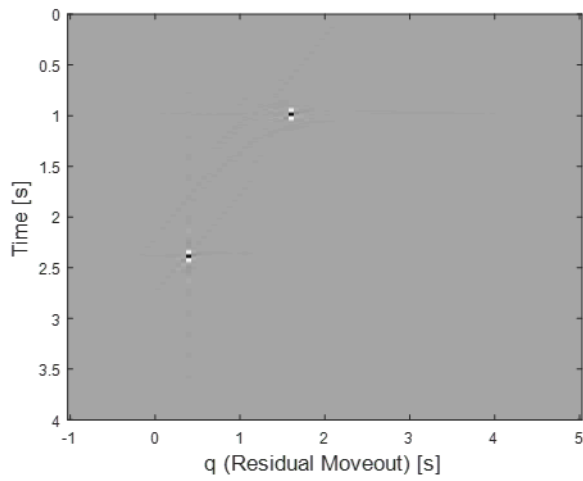
3.4.1 Simulation Result

The parameters of the synthetic seismic shot gather are same as used in the previous section. It contain two events with 10 missing seismic traces, as shown in Figure 3.9(a). Angle-based high resolution Radon transform is used for the interpolation of missing seismic traces. Figure 3.9(b) shows the Radon domain. Now, since a point in Radon domain will be hyperbolic in the time-offset domain, therefore, by taking the inverse Radon transform of Figure 3.9(b), the interpolated seismic data is produced. Figure 3.9(c) presents the data after the interpolation. The resulted image contains the interpolated data.

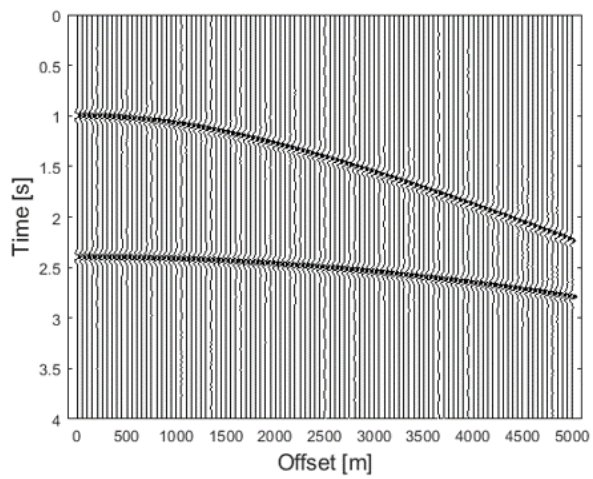
To further test the efficiency of proposed Radon transform for the interpolation of the seismic events Figure 3.10 shows the missing traces estimation with 40% compression. As expected the Radon transform work flawlessly for the interpolation of the events present in the data as shown in Figure 3.10(c). Likewise,



(a)



(b)



(c)

Figure 3.9: (a) The synthetic seismic reflected data with 10 missing traces. (b) The Radon transform of (a). (c) The interpolated data after applying the inverse transform on (b).

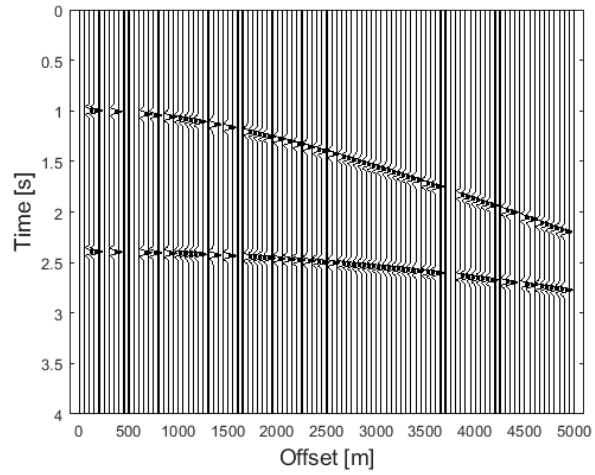
the proposed method was also tested for the initial missing traces, for which the results are presented in Figure 3.11.

To test the robustness of the proposed setup, data with different noise level is tested. Total number of traces and number of missing traces remains same. The results after the addition of the noise with 0.1 standard deviation and 30% compression are presented in Figure 3.12.

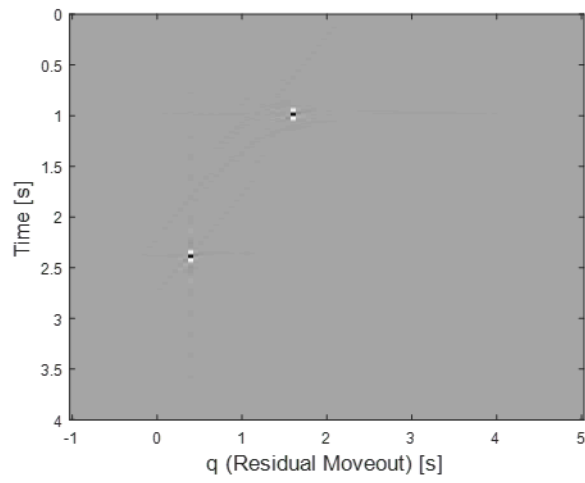
Similar comparison after the addition of white noise with standard deviation 0.4 is presented in the Figure 3.13, respectively. With this high level of noise, the events are completely missing from Figure 3.13(a), which makes manual interpolation virtually impossible. However, the interpolated events are fairly clear in Figure 3.13(b), which presents the results after the interpolation using angle-based Radon transform.

2-D Synthetic Data 2

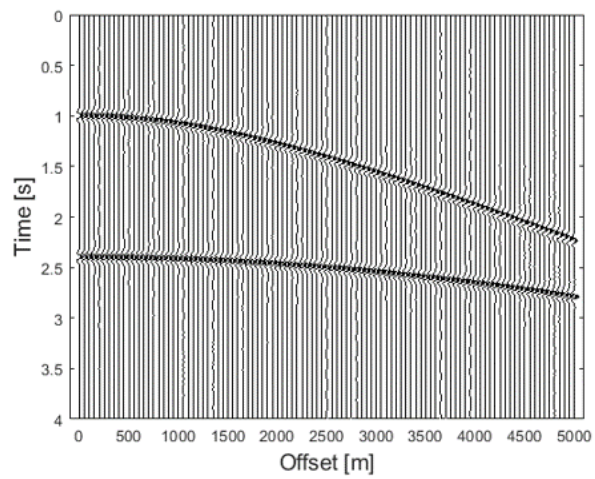
To further test the performance of the proposed Radon transform, it was applied to a more challenging data with 10 seismic events with some of them are overlapping and having same value of t , as shown in Figure 3.14(a). Total number of samples are 100 with spatial sampling of 50 m and sampling time 4 ms . The data with 10 missing traces is presented in Figure 3.14(b). The Radon domain and the interpolated data is presented in Figures 3.14(c)-(d). Figure 3.14(c) shows the peaks corresponding to all the events are distinct and well focused. The final interpolation result, Figure 3.14(d), shows that all the events are perfectly interpolated. Similarly, the result after the application of the angle-based Radon



(a)

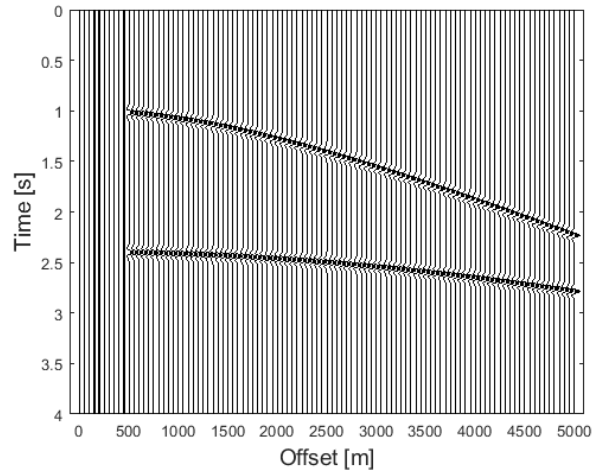


(b)

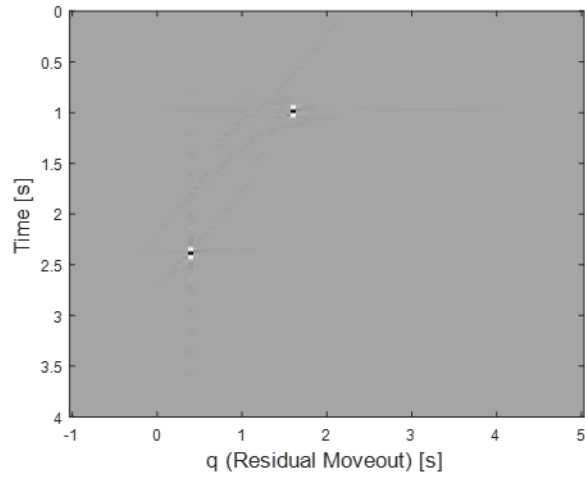


(c)

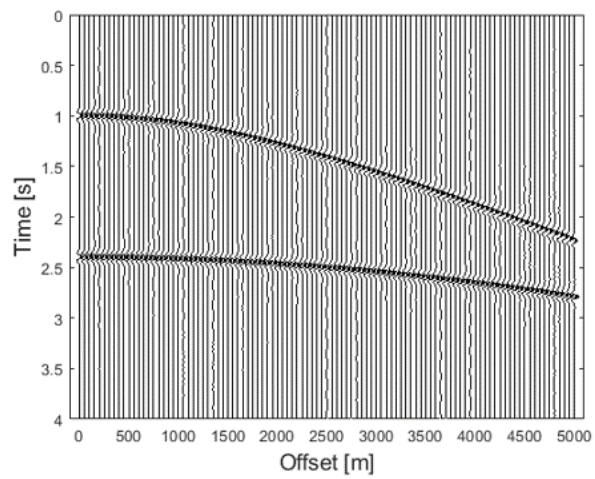
Figure 3.10: (a) The synthetic seismic reflected data with 40% missing traces. (b) The Radon transform of (a). (c) The interpolated data after applying the inverse transform on (b).



(a)

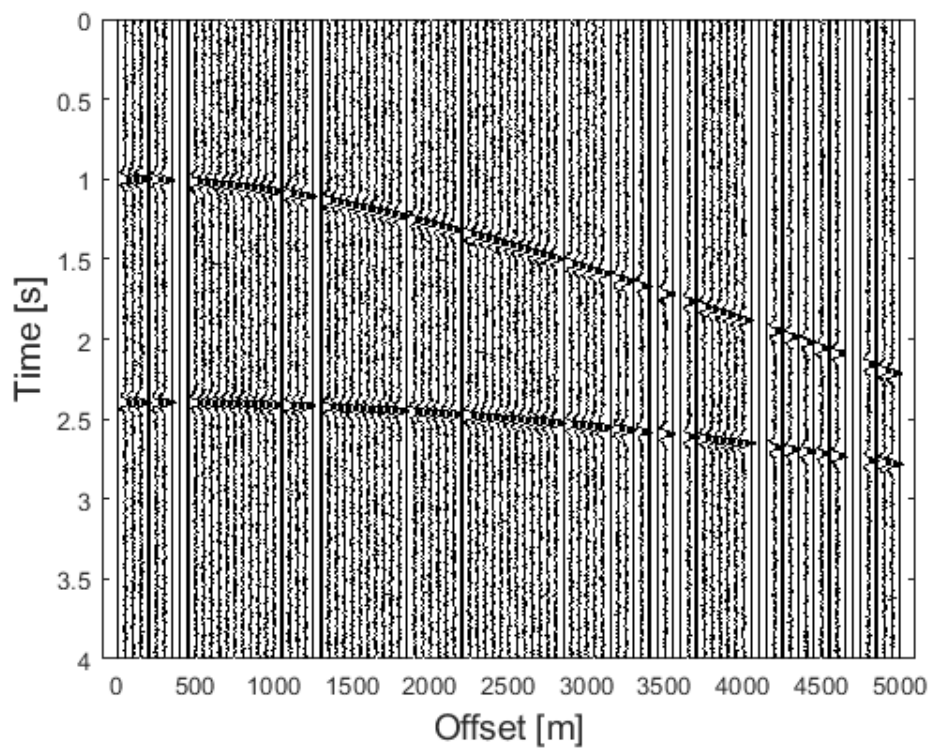


(b)

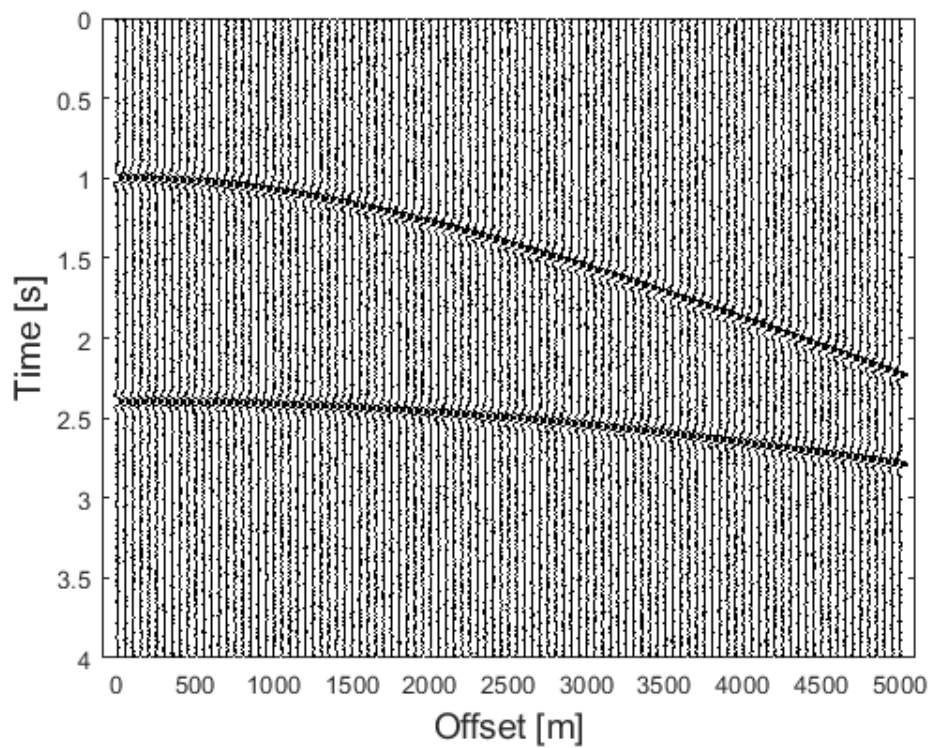


(c)

Figure 3.11: (a) The synthetic seismic reflected data with 10% missing traces. (b) The Radon transform of (a). (c) The interpolated data after applying the inverse transform on (b).

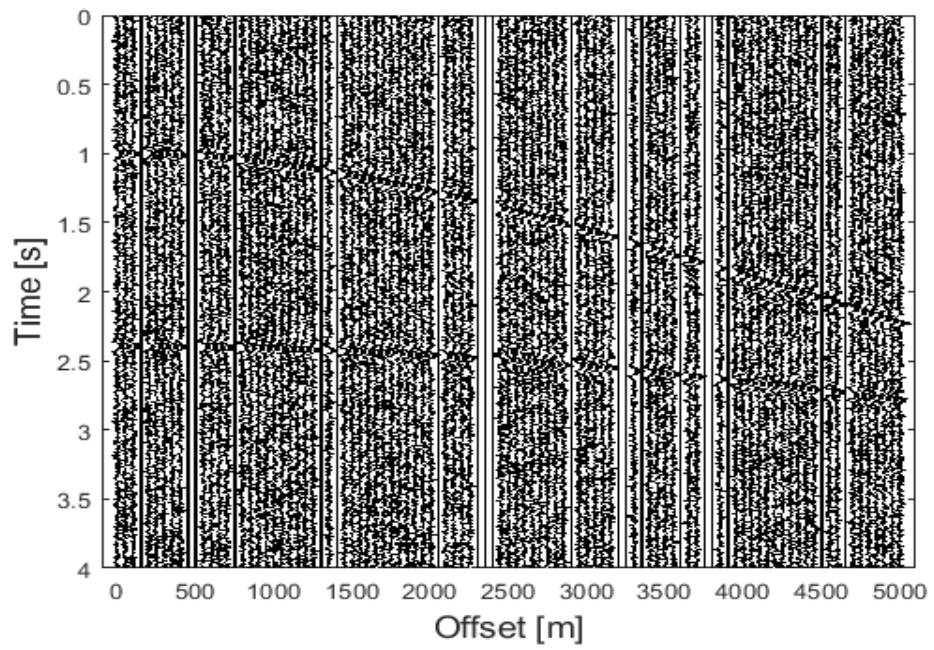


(a)

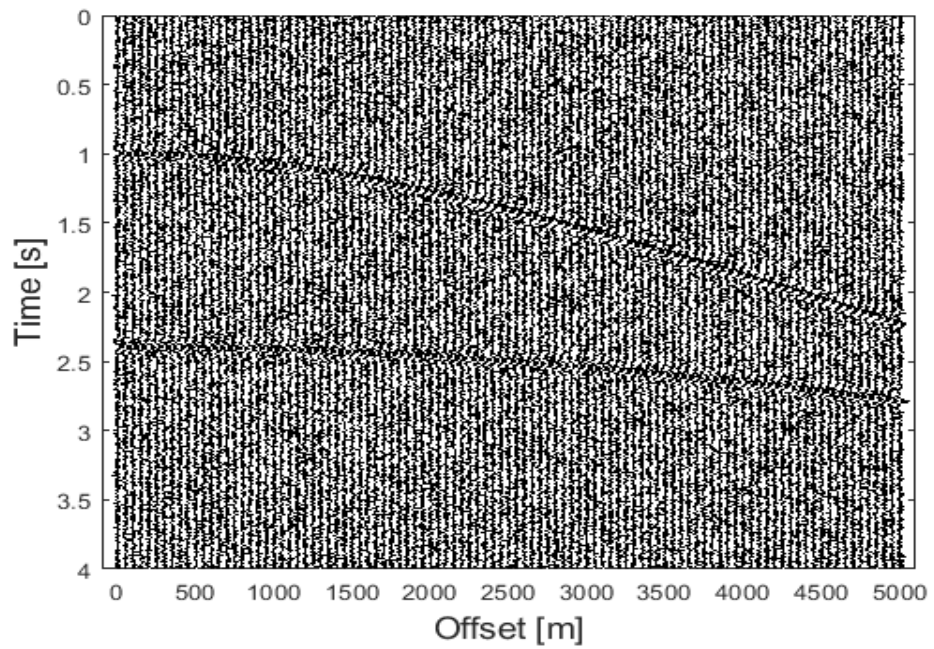


(b)

Figure 3.12: (a) The synthetic seismic reflected data with 10% random Gaussian noise and 30% compression. (b) The interpolated data after taking the inverse Radon transform.



(a)



(b)

Figure 3.13: (a) The synthetic seismic reflected data with 40% random Gaussian noise. (b) The interpolated data after taking the inverse Radon transform.

transform for the 30 missing traces is presented in Figure 3.15, which also shows the perfect reconstruction of the missing traces.

Comparison with Existing Methods:

To test the effectiveness of the proposed method it was compared with the existing Radon transform. Figure 3.16 presents the result after the application of the CG-FFT based high resolution Radon transform. The results shows that there are some artifact at the far offset and the interpolation data is not accurate (Figure 3.16(d)). One thing to note here is the fact that for the traditional method NMO is required. Similar results for a low- resolution Radon transform are presented in Figure 3.17. From Figure 3.17, it can be seen that the resolution of interpolated seismic data is low and events have low amplitudes. From the results in Figures 3.15 and 3.16 it is clear that the proposed method outperforms the traditional methods without the need of NMO correction. Furthermore, the proposed method is suitable for far-offset seismic data where the existing techniques does not work.

Noise Analysis:

Furthermore, to test the robustness of the proposed method, it was tested with the different levels of noise. The result for the 10% and 30% noise is presented in Figures 3.18 and 3.19. From the result in Figure 3.19 it is clear that the proposed method is robust in nature and works for high level of noise.

Quantitative Analysis:

To compare the accuracy of the proposed method, the original data (Figure 3.14(a)) was compared quantitatively with the proposed and existing methods

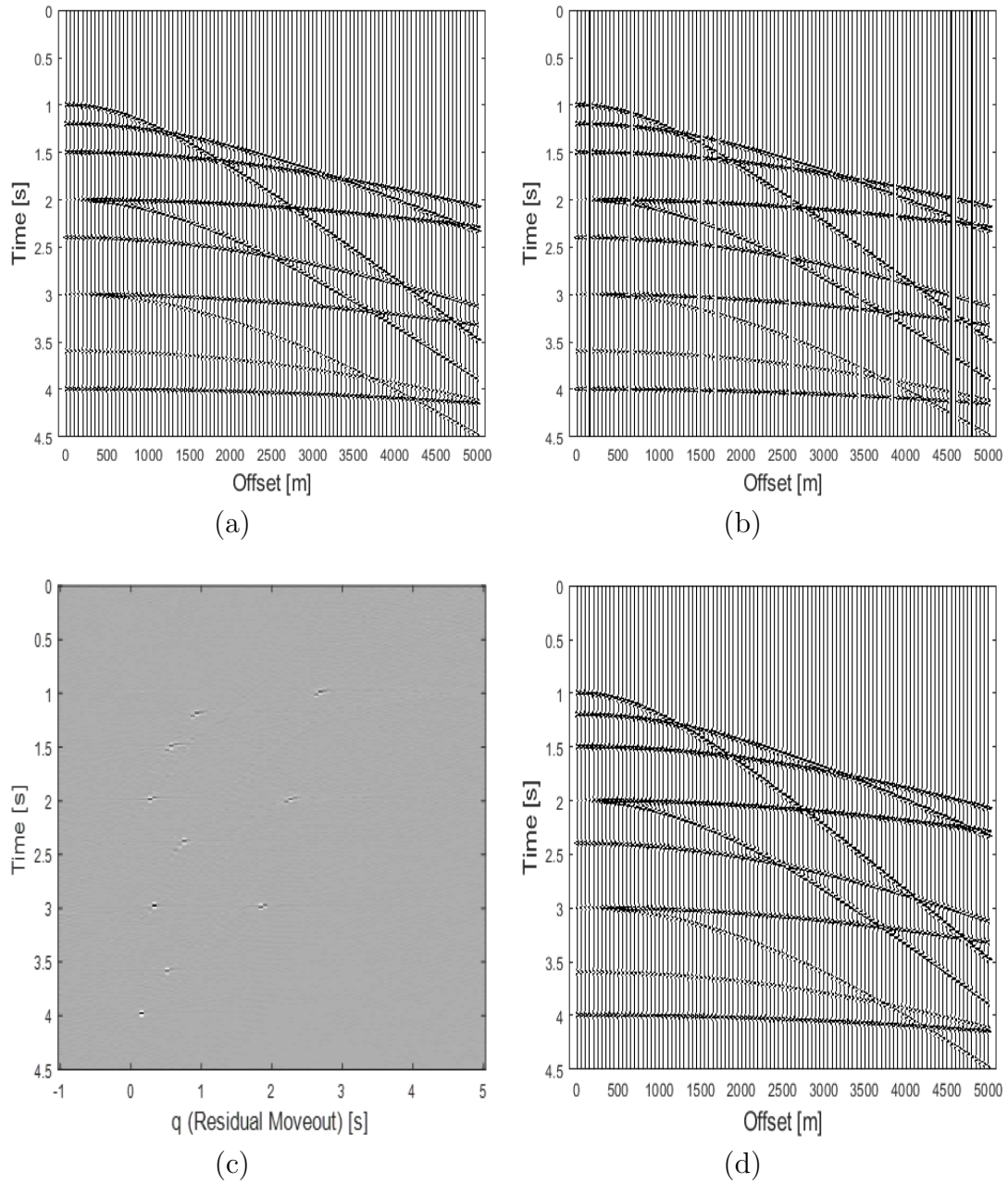


Figure 3.14: (a) The synthetic seismic reflected data. (b) The data with 10 missing traces and its angle-based Radon domain is shown in (c). (d) The interpolated data after applying the inverse transform on (c).

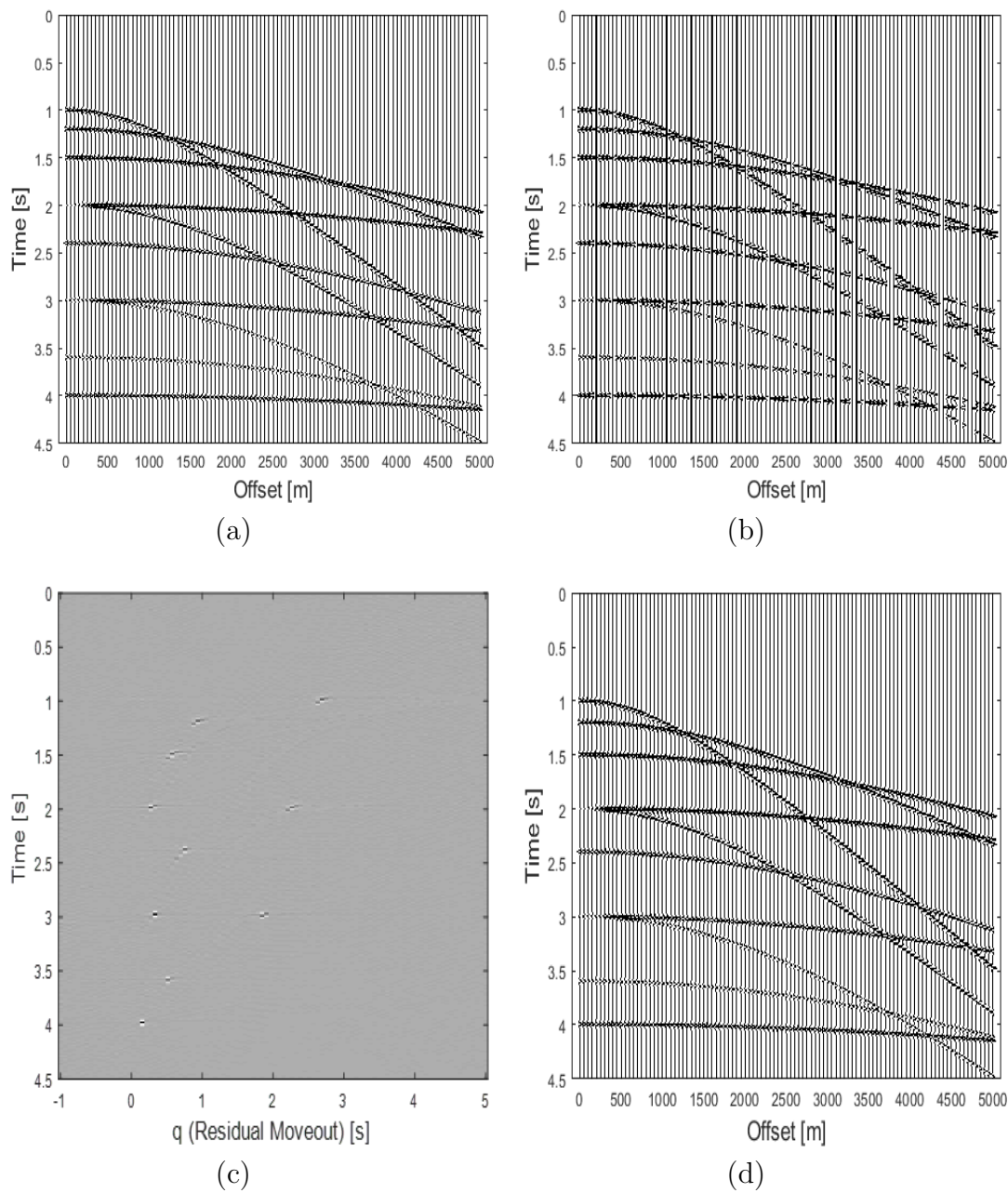
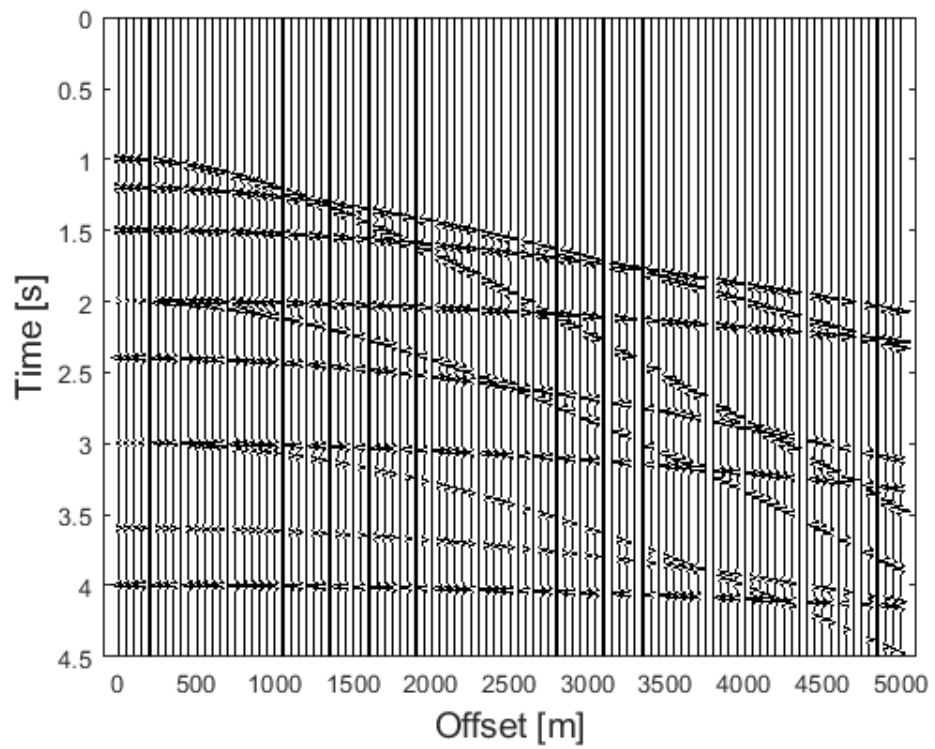
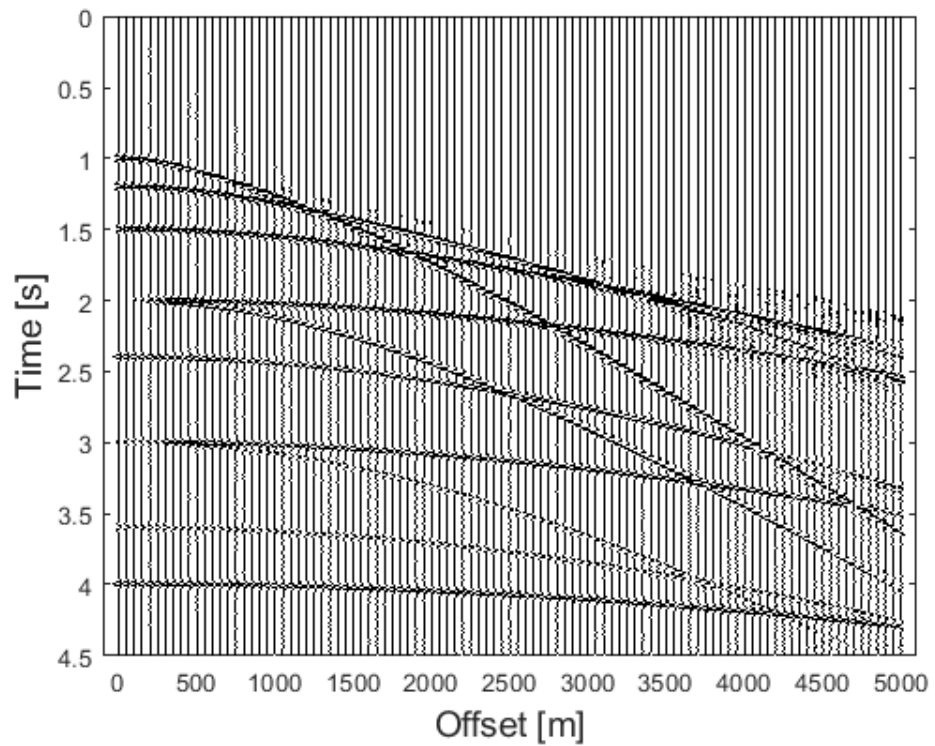


Figure 3.15: (a) The synthetic seismic reflected data. (b) The data with 30 missing traces and its angle-based Radon domain is shown in (c). (d) The interpolated data after applying the inverse transform on (c).

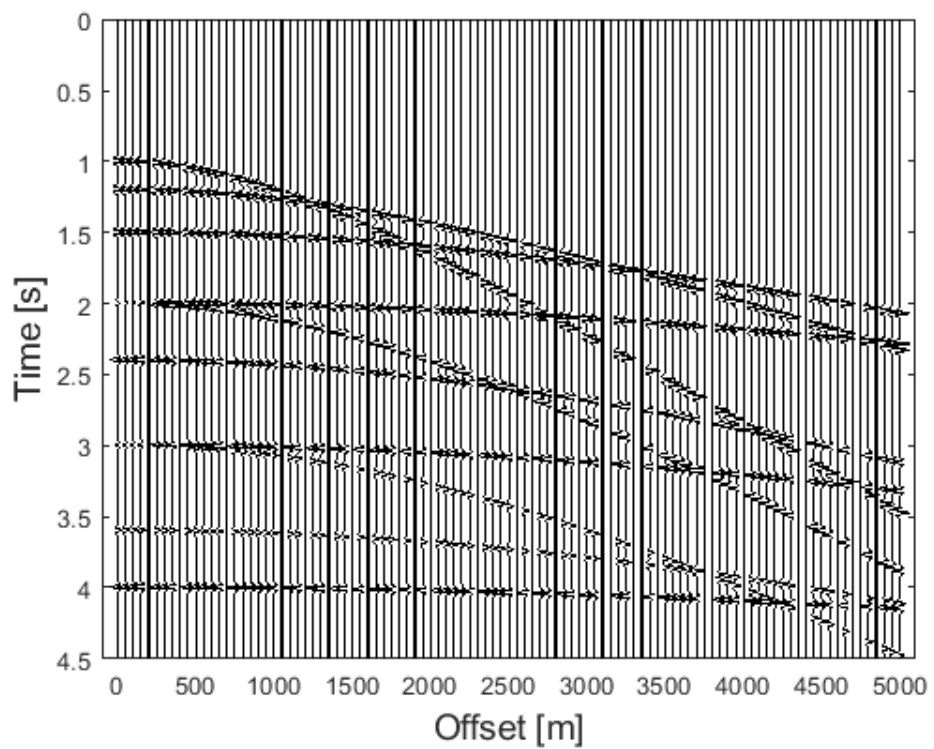


(a)

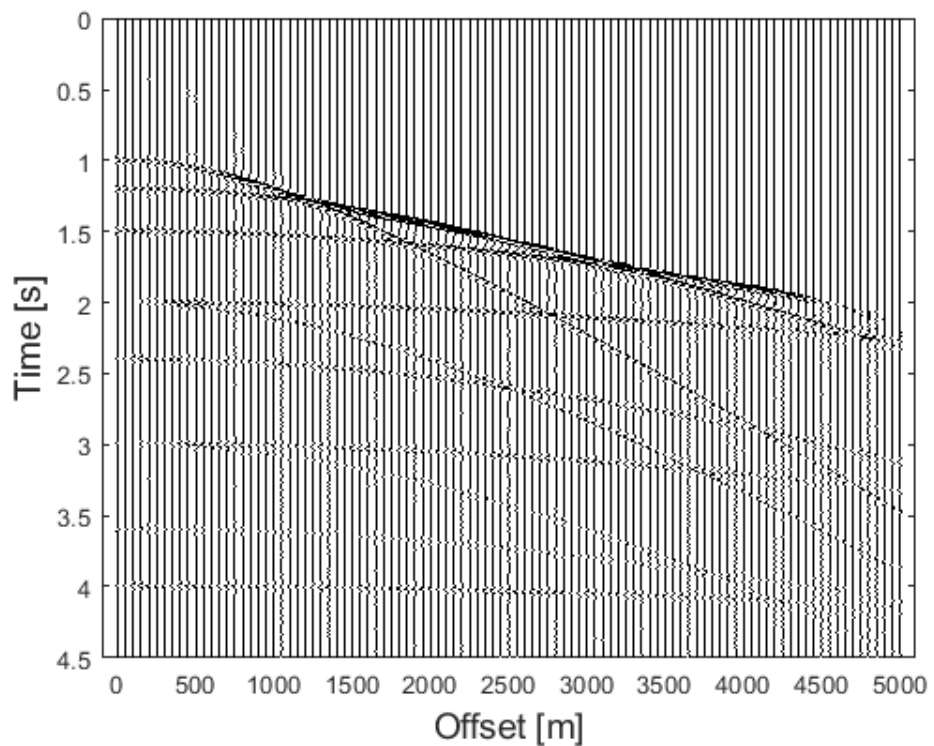


(b)

Figure 3.16: (a) The synthetic seismic reflected data with 30% compression and its interpolated version using CG-FFT based Radon transform is presented in (b).

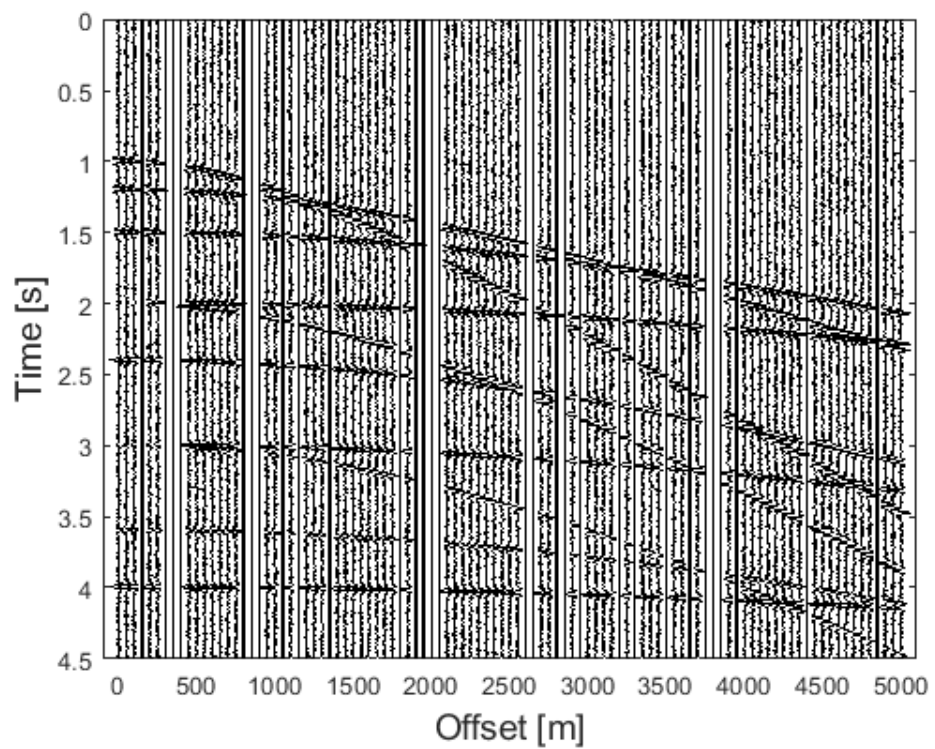


(a)

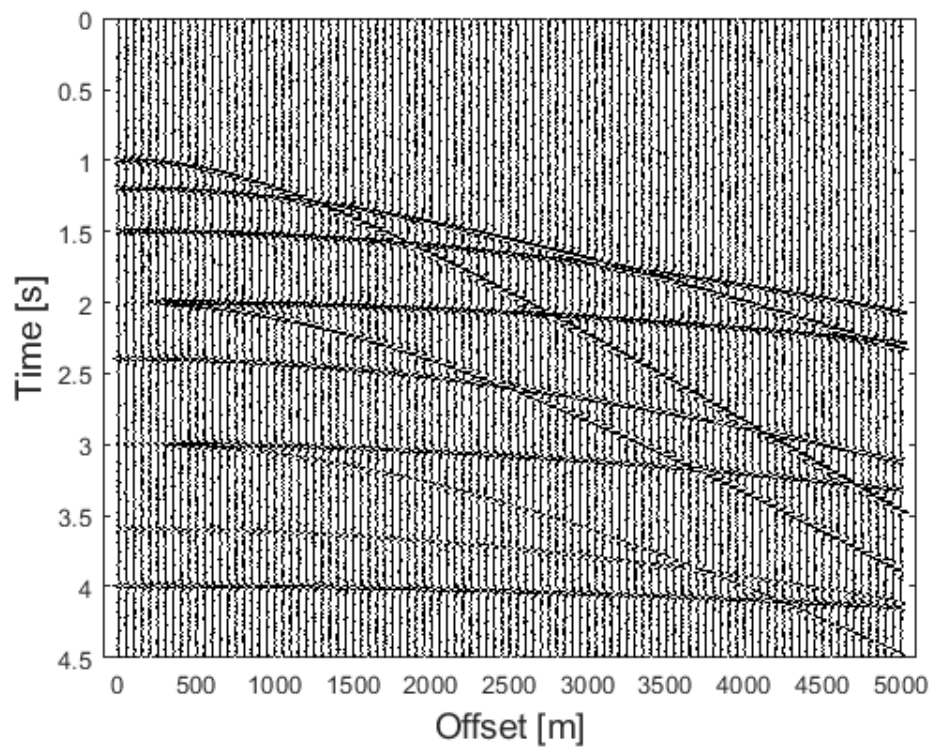


(b)

Figure 3.17: (a) The synthetic seismic reflected data with 30% compression and its interpolated version using least square Radon transform is presented in (b).

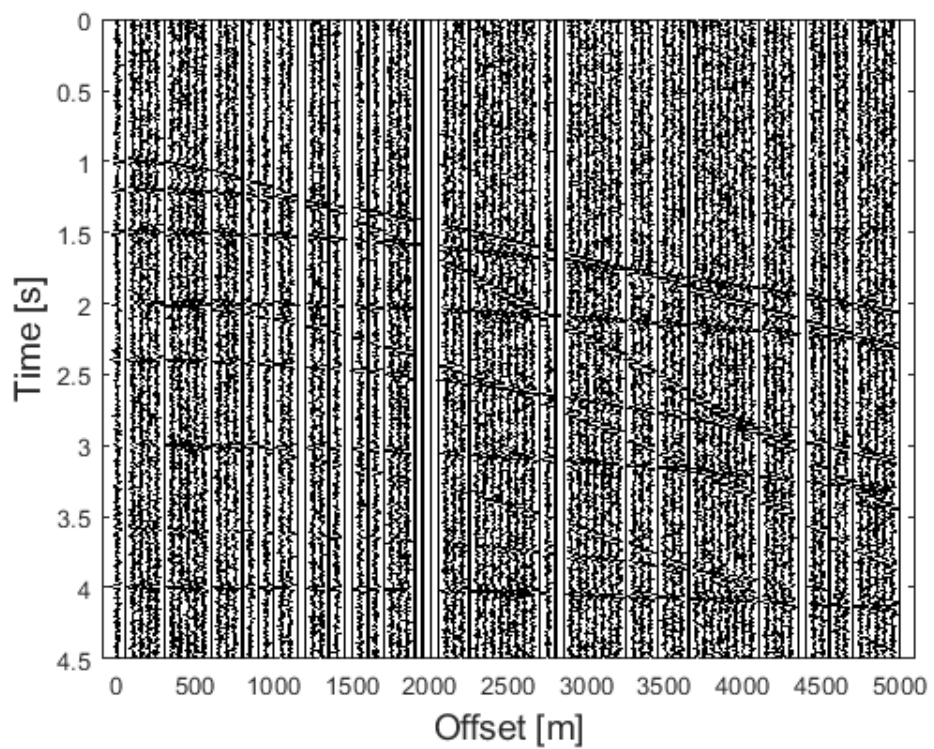


(a)

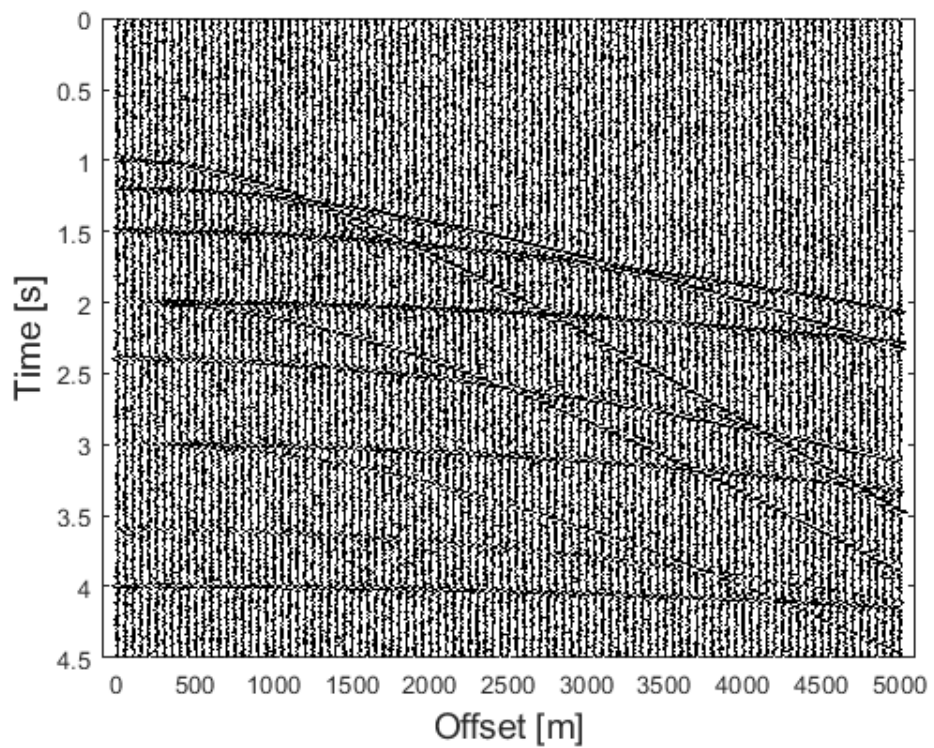


(b)

Figure 3.18: (a) The synthetic seismic reflected data with 10% noise and its interpolated version is presented in (b).



(a)



(b)

Figure 3.19: (a) The synthetic seismic reflected data with 30% noise and its interpolated version is presented in (b).

Table 3.2: Mean squared error for the angle-based Radon transform method versus other Radon transform methods for Figure 3.14(a).

Method	Noise	MSE
Angle-based Radon transform	-	0.0083
Low-resolution Radon transform (Levinson, Least Squares)	-	0.065
Fast high-resolution Radon transform (CG-FFT)	-	0.0095
Angle-based Radon transform	10%	0.0083
Low-resolution Radon transform (Levinson, Least Squares)	10%	0.070
Fast high-resolution Radon transform (CG-FFT)	10%	0.0097
Angle-based Radon transform	30%	0.0084
Low-resolution Radon transform (Levinson, Least Squares)	30%	0.04
Fast high-resolution Radon transform (CG-FFT)	30%	0.0105

of Radon transforms. The results are summarized in Table 3.2. From Table 3.2, it is evident that the results for the proposed method are more accurate than those of existing methods for Radon transforms and are comparable to the high-resolution Radon transform.

The proposed method is, in general, more accurate than the existing techniques. Furthermore, the propose method does not need NMO correction and works for far-offsets.

3-D Real Data

The same method was applied for the interpolation of the 3-D real seismic data. For the 3-D data, the interpolation was performed along the cross-line and in-line direction using the proposed method. The real data from Waihapa, New Zealand ¹

was used for the testing of the interpolation. The data is presented in Figure 3.20. The proposed method was applied to in-line and cross-line dimension, separately. The in-line 211 data is shown in Figure 3.21(a). The data with 20 % missing traces is presented in Figure 3.21(b). By applying the forward and inverse angle based Radon transform the interpolated data is presented in Figure 3.21(c). By looking at the 3.21(c), it can be seen that there are some traces which are missing. This is due to the complexity and the large number of traces. The performance can be enhanced by reapplying the proposed method and the results after the 3 iterations is presented in Figure 3.21(d). The interpolated data in the Figure 3.21(d) is quite close to the original in-line data 3.21(a). Although, multiple iterations of the Radon transform is quite common in high-resolution Radon transform, however, another way to improve the interpolation result without the utilization of several iteration is to perform the propose method on different sections of the data separately.

Similarly, the interpolation was also applied to the cross-line number 153 of the 3-D data base. The data and the missing data are presented in Figures 3.22(a)-b. The result after the interpolation of the missing data is shown in Figure 3.22(c).

For the comparison, the same data base is used with CG-FFT based Radon transform. The results for cross-line direction are presented in Figures 3.23. From the simulation results for the CG-FFT based Radon transform, it is evident that it is not efficient as compared to the proposed Radon transform model. To put the results quantitatively, the error was calculated between the actual data and the

Table 3.3: Mean squared error for the proposed angle-based Radon transform method versus other Radon transform methods for 3-D Real Dataset.

Method	MSE
Angle-based Radon transform	0.0115
Low-resolution Radon transform (Levinson, Least Squares)	0.155
Fast high-resolution Radon transform (CG-FFT)	0.0145

interpolated data. Table 3.3 shows the error for the proposed method and traditional Radon transform which also shows that the proposed method outperforms the traditional methods.

3.5 Multiple Removal

The captured data along with primary reflections contain many undesired components such as multiple reflections, refractions, diffractions etc [52]. Furthermore, due to the complex geological conditions, different kinds of multiple reflections are generated; these reflections significantly reduce the resolution of recorded seismic data as they get mixed with primary waves. These reflections interfere with the primary reflections, which in turn make the processing of seismic data more difficult. Migrations and inversion schemes also require seismic data without these multiple reflections. Besides difficulty in identification of primary reflections we also face difficulties in the data analysis and interpretation. Attenuation of multiple reflections from the recorded seismic data is one of the key issues in the field of seismic data processing, so we can obtain the accurate description of the concerned surface as accurately as possible.

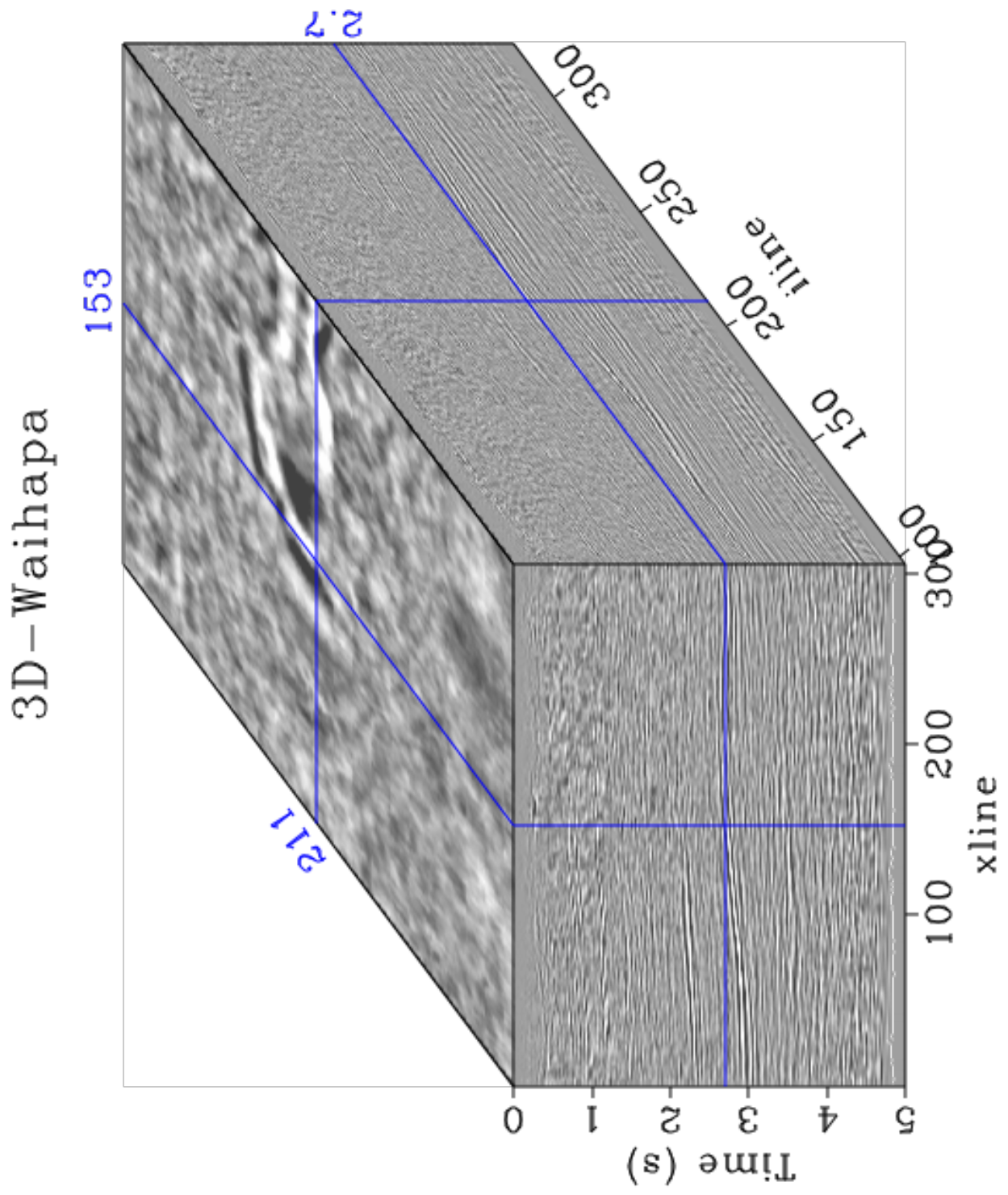


Figure 3.20: 3-D Real Data from Waihapa, New Zealand (Courtesy of New Zealand Petroleum and Minerals (NZPM)).

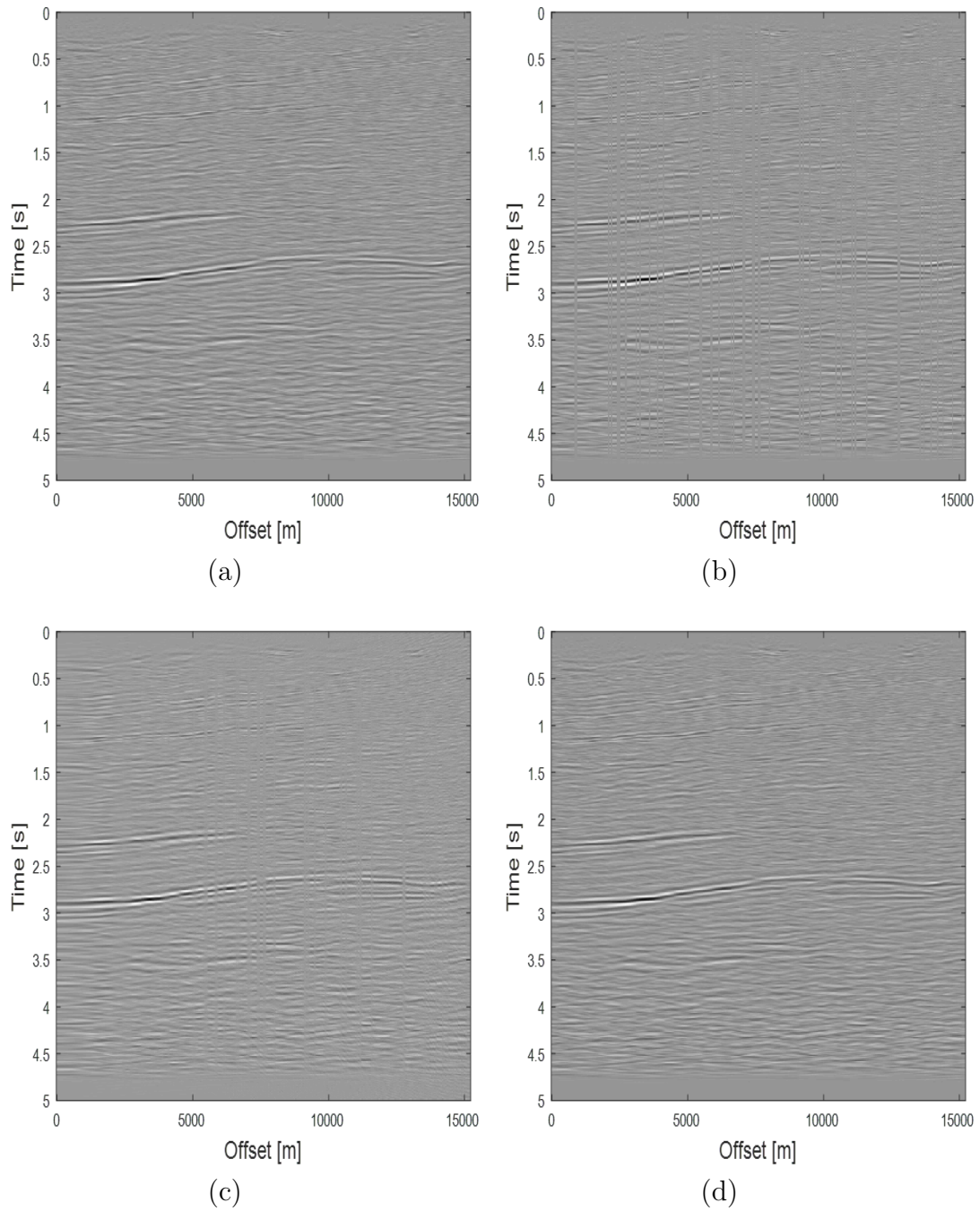
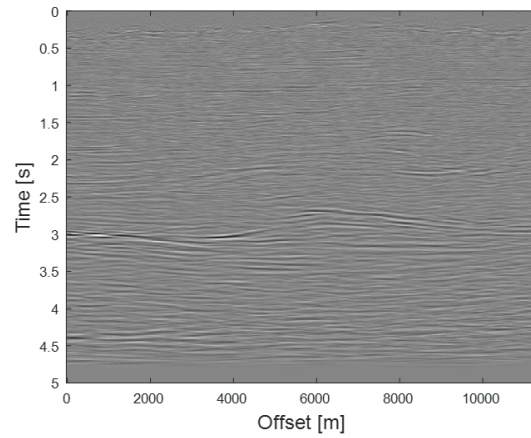
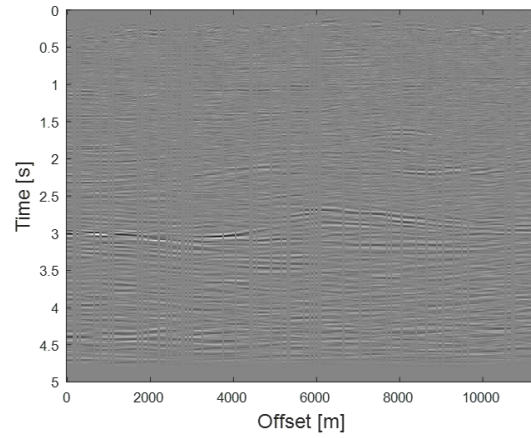


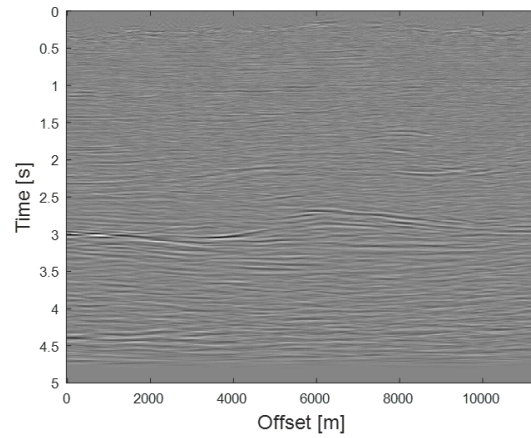
Figure 3.21: Reconstruction of missing traces with 20% compression using angle-based Radon transform: (a) The real in-line data from the Waihapa, New Zealand (Courtesy of New Zealand Petroleum and Minerals (NZPM)). (b) The data with 20 % missing traces. (c) The interpolated data after 1 iteration. (d) The interpolated data after 3 iterations.



(a)

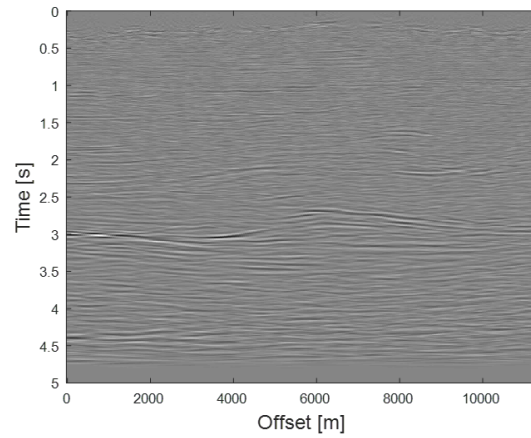


(b)

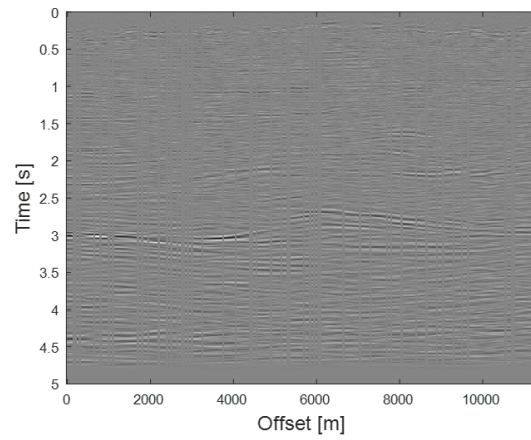


(c)

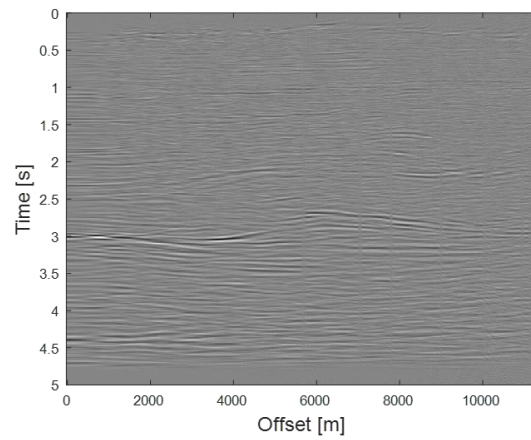
Figure 3.22: Reconstruction of missing traces with 20% compression using angle-based Radon transform: (a) The real cross-line data from the Waihapa, New Zealand (Courtesy of New Zealand Petroleum and Minerals (NZPM)). (b) The data with 20 % missing traces. (c) The interpolated data after 3 iterations.



(a)



(b)



(c)

Figure 3.23: Reconstruction of missing traces with 20% compression using CG-FFT Radon transform: (a) The real cross-line data from the Waihapa, New Zealand (Courtesy of New Zealand Petroleum and Minerals (NZPM)). (b) The data with 20 % missing traces. (c) The interpolated data after 10 iterations.

Many algorithms have been presented for the multiple attenuation. Methods depending upon the moveout and different transform have been discussed in [7, 57, 63]. In transformed domain, the unwanted regions are muted and we end up with only the primary reflections. Methods based on prediction and extraction of multiples are also presented. Wave-field extrapolation and predictive deconvolution are the example of these techniques. These techniques work well with surface-related multiple removal. These techniques are presented in [64] and [65]. These methods are time consuming so adaptive algorithms are presented in [57, 66, 67]. There are some techniques which use independent component analysis for the multiple removal as discussed in [68–70].

Algorithm

Given a seismic record, the proposed method for multiple reflections removal is stated as follows:

1. Use the angle based Radon transform to obtain the Radon domain.
2. Use the following facts to generate an automatic mask (zero for the primary reflections):
 - (a) In the Radon domain, primary reflection and multiple reflections can be partitioned by a line.
 - (b) The multiple reflection lies below the line and can be extracted.
3. Multiply the mask with the Radon domain. This will leave only the multiple reflections in the Radon domain.

4. Apply the inverse Radon transform to the previous step result to extract the multiples.
5. Finally, subtract the multiples from the original data to extract the primaries.

3.5.1 Simulation Results

To test the proposed Radon transform, it was applied to a dataset with 10 seismic events with some of them are overlapping and having same value of t , as shown in Figure 3.24(a). The data contain 4 primary seismic events, as shown in Figure 3.24(b). Total number of samples are 100 with spatial sampling of 50 m and sampling time 4 ms. The Radon domain is presented in Figures 3.24(c). Figure 3.24(c) shows that the peaks corresponding to all the events are distinct and well focused. Furthermore, a line can be drawn to separate the primary and multiple events, as shown in Figure 3.24(d). Now, the result after muting the primaries and taking the inverse Radon transform is shown in Figure 3.24e. Figure 3.24(e) presents the estimated multiples from the original data. Finally, subtract the estimated multiples from the original data (Figure 3.24(a)), to obtain the Figure 3.24(f). Figure 3.24(f) shows the data after the multiple removal. The difference between the estimated primary and real primary is minute and the proposed algorithm can efficiently perform the multiple removal.

Comparison with Existing Methods:

As mentioned earlier, Radon transform is mostly used for the multiple attenuation

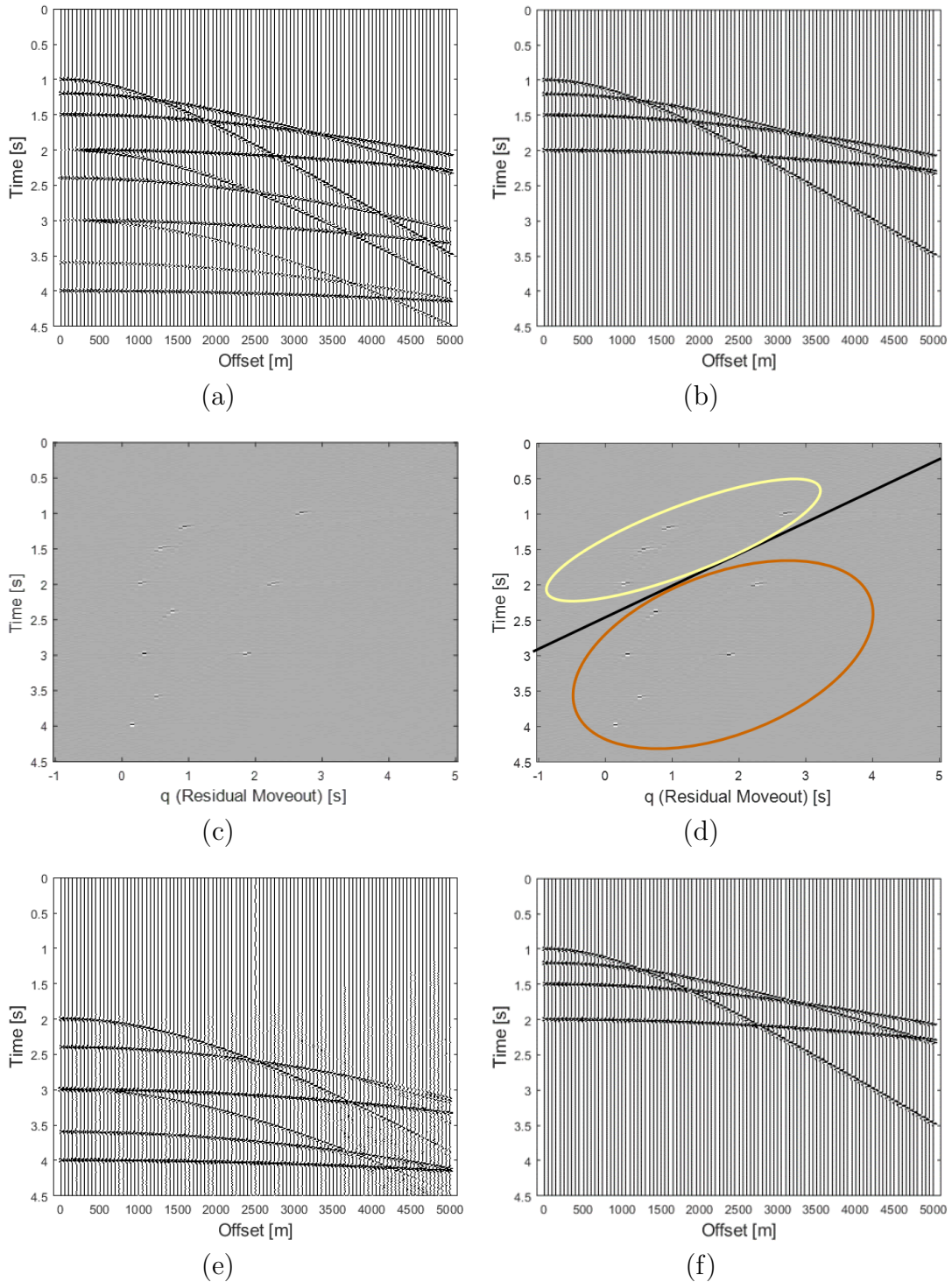


Figure 3.24: (a) The synthetic seismic reflected data with multiples. (b) The original primary reflection of the (a). (c) The angle based Radon transform of (a). (d) Separation of multiples and primaries in Radon domain. (e) Estimated multiples of (a). (f) The primary reflection.

of seismic data and the best Radon transform to achieve this is high-resolution Radon transform. The same data was tested with the existing high resolution CG-FFT based technique and results are presented in Figure 3.25. From the Figure 3.25, it is evident that for the noisy data the existing method doesn't provide good estimate of the primaries and it fails at far-offset.

Noise Analysis:

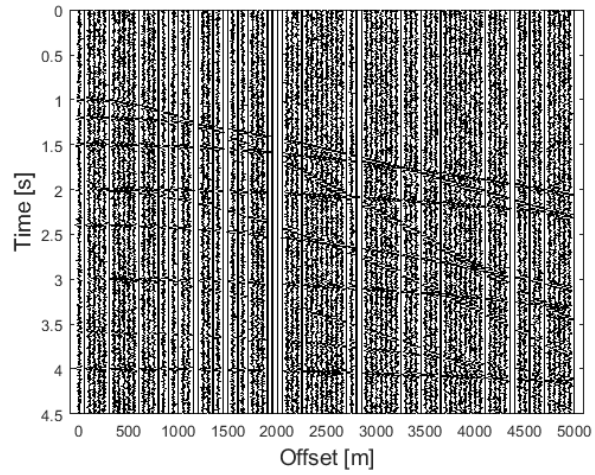
To test the robustness of the proposed method, white noise was introduced in the original data of Figure 3.24(a) and the result is shown in Figure 3.26(a). The result after the muting is presented in Figure 3.26 which shows that the proposed method is robust in nature and can be used for multiple removal, effectively.

Quantitative Analysis:

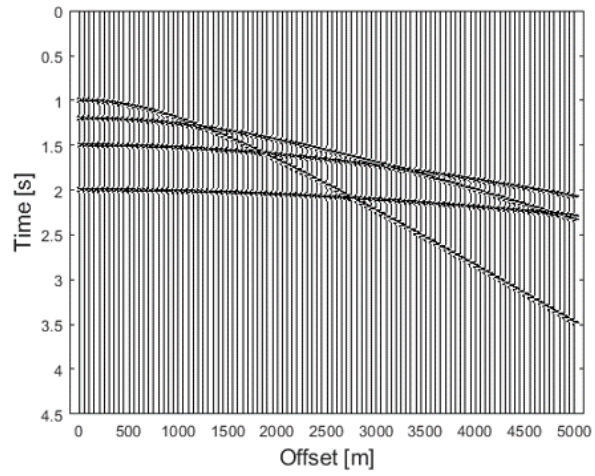
To compare the accuracy of the proposed method, the original primary reflection (Figure 3.24(b)) was compared quantitatively with the proposed and existing methods of Radon transforms. The results are summarized in Table 3.4, which presents the mean squared error (MSE). From Table 3.4, it is evident that the results for the proposed method are more accurate than those of existing methods for Radon transforms and are comparable to the high-resolution Radon transform.

2-D Real Data

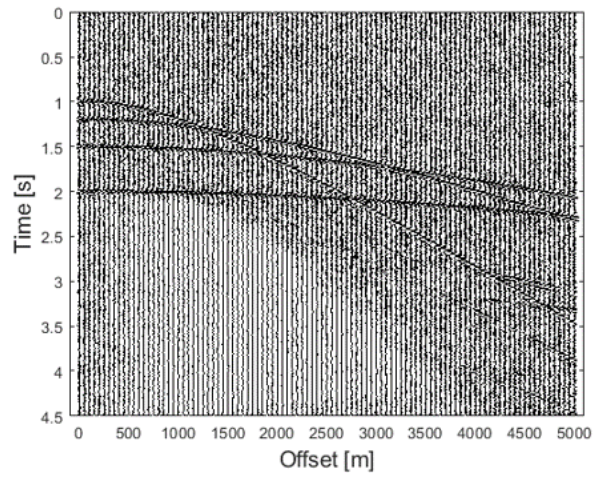
Finally, the proposed angle-based, high-resolution Radon-transform-based algorithm for multiple-reflection attenuation was tested on a real dataset from the Gulf of Mexico [5]. An NMO corrected CMP gather for this marine dataset² is presented in Figure 3.27(a). The sampling interval for the data was 4 ms and it



(a)

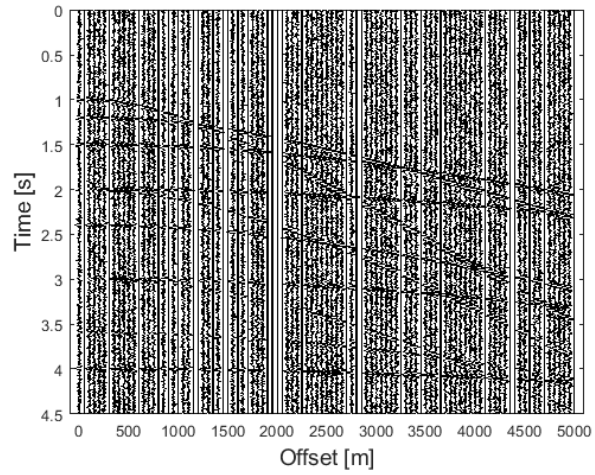


(b)

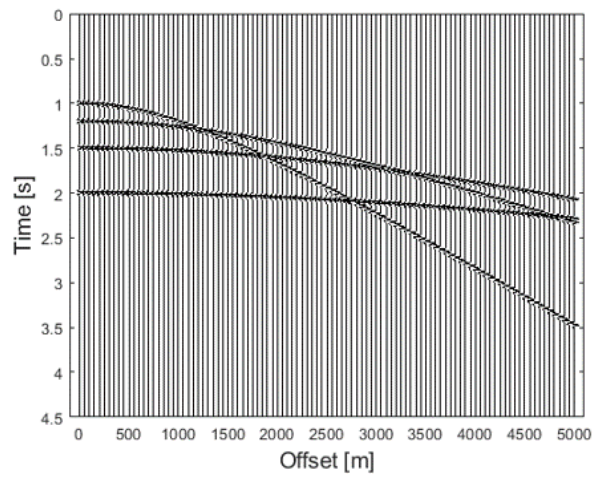


(c)

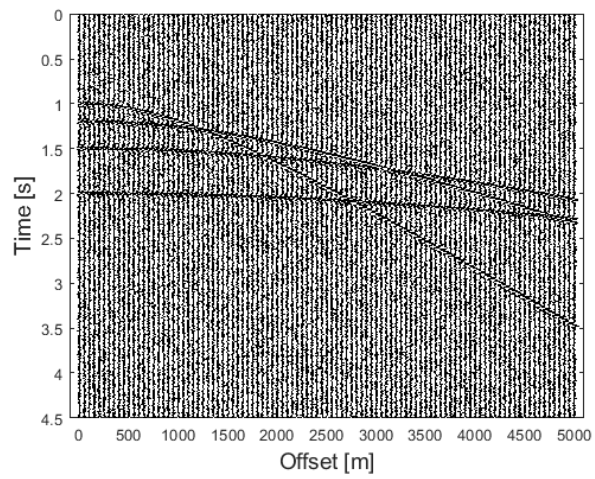
Figure 3.25: (a) The synthetic seismic reflected data with multiples and 20% noise. (b) The original primary reflection of the (a). (c) The estimated primary reflection using CG-FFT based Radon transform.



(a)



(b)



(c)

Figure 3.26: (a) The synthetic seismic reflected data with multiples and 20% noise. (b) The original primary reflection of the (a). (c) The estimated primary reflection.

Table 3.4: Mean squared error for the proposed angle-based Radon transform method versus other Radon transform methods for Figure 3.24(b).

Method	Noise	MSE
Angle-based Radon transform	-	0.0072
Low-resolution Radon transform (Levinson, Least Squares)	-	0.0127
Fast high-resolution Radon transform (CG-FFT)	-	0.0089
Angle-based Radon transform	10%	0.0073
Low-resolution Radon transform (Levinson, Least Squares)	10%	0.0242
Fast high-resolution Radon transform (CG-FFT)	10%	0.0095
Angle-based Radon transform	30%	0.0075
Low-resolution Radon transform (Levinson, Least Squares)	30%	0.0351
Fast high-resolution Radon transform (CG-FFT)	30%	0.0098

contained 92 traces ($N = 92$). The result after the application of the proposed method for multiple attenuation is presented in Figure 3.27(b). Similarly, Figures 3.27(c)-(f) present results for the adjoint, least squares, Cholesky, CG-FFT, and Radon transform methods, respectively. Clearly, as expected, the high-resolution and proposed Radon transforms outperform the low-resolution Radon transform results. From the results, it is evident that the proposed Radon transform outperforms all other techniques.

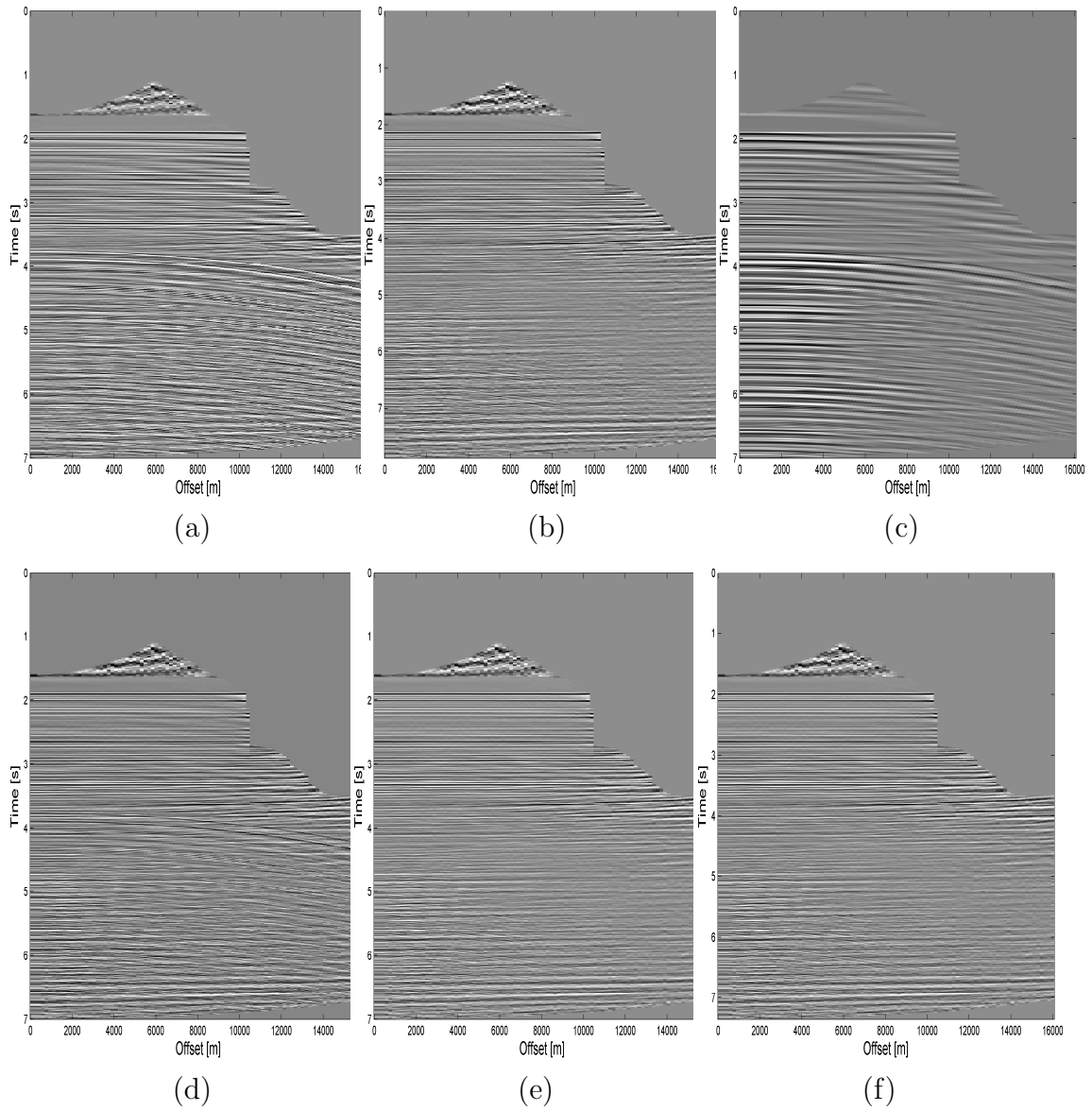


Figure 3.27: Multiple-reflection attenuation by Radon transform. (a) Real dataset from the Gulf of Mexico with a total of 92 traces ($N=92$). (b)-(f) presents the data after multiple attenuation using different versions of Radon transforms: the proposed , adjoint, least squares, Cholesky, and CG FFT methods, respectively.

3.6 Conclusion

In this chapter, a new method for angle-based high resolution Radon transform is presented. The proposed technique produces better results to the existing techniques but without NMO correction as required for the existing techniques. The method was tested for the interpolation and multiple attenuation. From the simulation results, it is clear that angle-based Radon transform produces high resolution Radon transform and interpolate seismic data, and attenuate multiple reflections, effectively. The proposed technique was compared with well known method for high resolution Radon transform. For the tested data, the proposed method is better than the most accurate Radon transform method.

CHAPTER 4

PROJECTIONS ONTO CONVEX SETS BASED RADON TRANSFORM

The demand for high resolution seismic data is increasing, however, due to poor conditions or the topological structures of the Earth's surface, it is not possible to place seismic sensors resulting in missing traces in the acquired data. Finding these missing traces is a key step in seismic data processing and there are many different techniques are used to interpolate the missing traces. In this chapter, a new technique is proposed which uses projections onto convex sets and Radon transform to estimate the missing traces. The proposed method is robust and provides better estimates than the existing Radon transform based techniques. First a brief introduction of projections onto convex sets is presented. The second section presents the proposed method of interpolation. The method was tested

on 2-D and 3-D datasets and results are presented in last section of the chapter.

4.1 Introduction

Due to its many attractive properties [71], projections onto convex sets (POCS) theory has been used for several signal and image processing applications. For example, it was used for the design of explicit depth $f - x$ wavefield extrapolation operators [72], filter design [73–76], image recovery and restoration [77, 78], deconvolution [71, 79, 80], kernel synthesis for time-frequency analysis [81], inversion of cross borehole imaging [82], image compression [71], and many more. For more details on the POCS theory, it is recommended to read the book by Stark [71]. In general, the POCS can handle any number of constraints including linear and convex types. Additionally, it is very flexible since crucial requirements can be conveniently incorporated. Finally, the resulting operators will satisfy all predefined constraint sets, as long as the imposed constraints are not contradictory and mutually exclusive [71].

4.1.1 Projections onto convex sets

In mathematics, projections onto convex sets (POCS), sometimes also known as the alternating projection method, is a method to find a point in the intersection of two or more closed convex sets. In a vector space, a set C is convex iff $\forall \mathbf{x} \in C$

and $\mathbf{y} \in C$, then

$$\lambda \mathbf{x} + (1 - \lambda) \mathbf{y} \in C \quad \forall \quad 0 \leq \lambda \leq 1,$$

also lies in C . Graphically, it can be seen from Figure 4.1. Some examples of convex and non convex sets are presented in Figure 4.2.

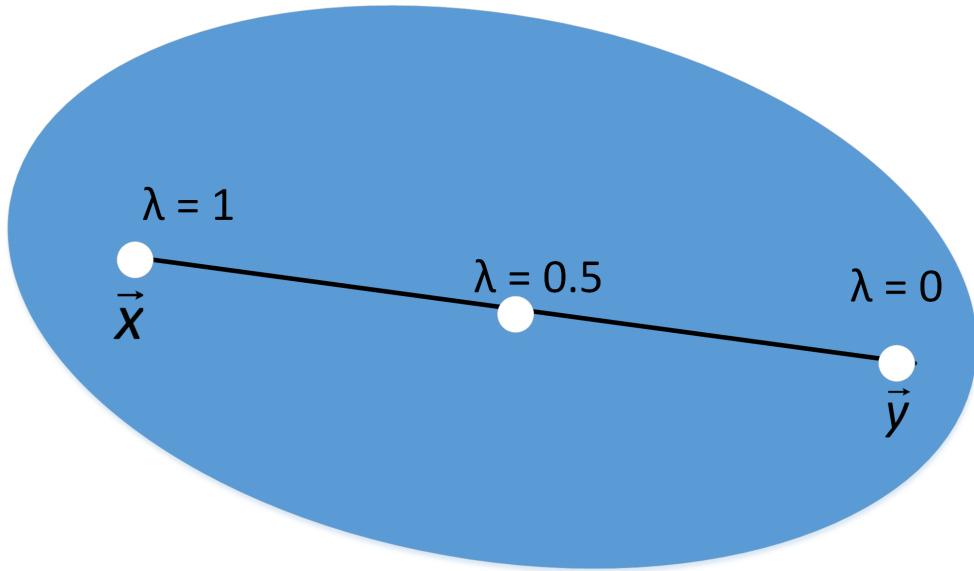
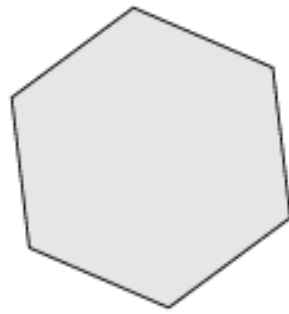


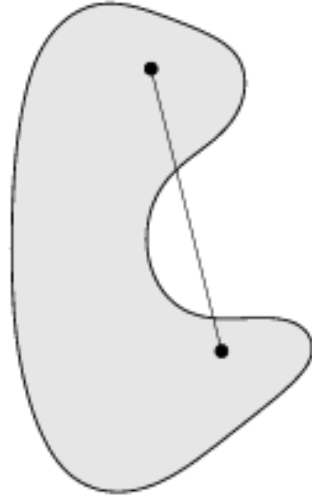
Figure 4.1: Example of convex set.

The theory of Projections onto Convex Sets (POCS) is briefly reviewed to help facilitate a better understanding of this proposed method. To begin, let all the operators of interest be elements of a Hilbert space \mathbf{H} , and consider a closed convex set C , which is a subset of \mathbf{H} . Then, for any vector $\mathbf{h} \in \mathbf{H}$, the projection $P_C \mathbf{h}$ of \mathbf{h} onto C (where P_C is an operator) is the nearest neighbour element in C to \mathbf{h} (i.e., \mathbf{y}) and is determined by:

$$\|\mathbf{h} - P_C \mathbf{h}\| = \min_{\mathbf{y} \in C} \|\mathbf{h} - \mathbf{y}\|, \quad (4.1)$$



convex



not convex



not convex

Figure 4.2: Example of convex and concave sets.

where $\|\cdot\|$ is the Euclidean norm. Without ambiguity, the operator P_C is in general a nonlinear projection operator that maps any vector $\mathbf{h} \in \mathbf{H}$ to a vector that belongs to C . The basic idea of POCS follows: every known property (e.g., say the i^{th} property) of the unknown $\mathbf{h} \in \mathbf{H}$ will restrict \mathbf{h} to lie in a closed convex set, say $C_i \in \mathbf{H}$. Assume that C_1, C_2, \dots, C_m denote m (for m known properties) closed convex sets in a Hilbert space \mathbf{H} , and C_o denotes their intersection set given by

$$C_o = \bigcap_{i=1}^m C_i. \quad (4.2)$$

The set C_o , which is considered as the solution set, will contain elements that satisfy all the constraint sets and will therefore represent feasible solutions. For each $i = 1, 2, \dots, m$, let P_{C_i} denote the projection operator onto the set C_i . Then, the Fundamental Theorem of POCS is given as follows [71]:

Theory 1 *Assume that C_o is non-empty. Then, for every $\mathbf{h} \in \mathbf{H}$ and $i = 1, 2, \dots, m$, the sequence $\{P_n \mathbf{h}\}$ converges weakly to a point of C_o .*

In other words, theorem 1 states that the vector iterates $\{\mathbf{h}_k\}$ generated by

$$\mathbf{h}_{k+1} = \prod_{i=1}^m P_{C_i} \mathbf{h}_k, \quad (4.3)$$

with an arbitrary starting point \mathbf{h}_0 , will converge weakly to a point of C_o , and since the Hilbert space is of finite dimension, the algorithm will strongly converge to a point within C_o [74]. The intersection of different convex sets is also convex

and alternating POCS will converge to a point common to both sets as shown in Figure 4.3.

Some properties of Projections onto convex sets are summarized below:

- Alternating POCS among N convex sets with a non-empty intersection will converge to a point common to all.
- Alternating POCS among two non intersecting convex sets will converge to the point in each set closest to the other.
- Alternating POCS among three or more convex sets with an empty intersection will converge to a limit cycle.

In simple terms, POCS can be used to find the intersection points of the convex and closed sets by projecting one onto another. Different convex sets are defined and with each iteration they converges to the point of intersection. This process is continued until a feasible solution is achieved or number of iterations are exceeded. In the following section, POCS is used along with Radon transform to find the missing seismic traces.

4.2 The proposed POCS based Radon transform

For the second proposed version of the Radon transform, projections onto convex sets is used for the interpolation of the missing seismic traces. During the last

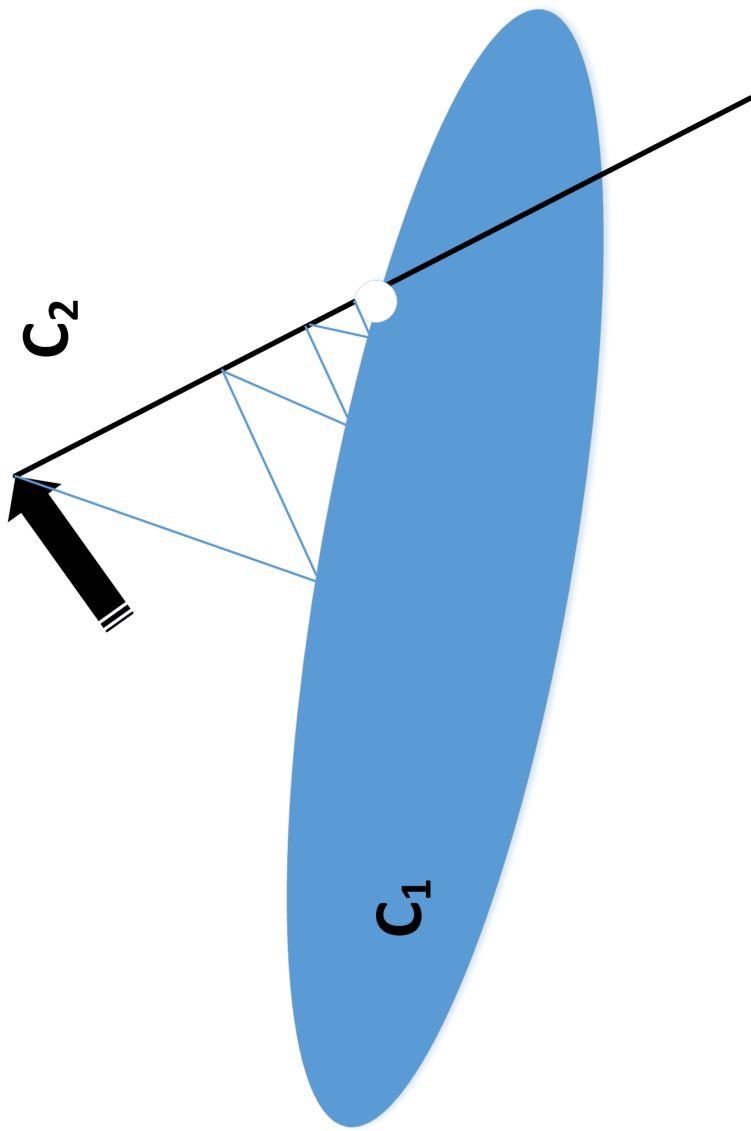


Figure 4.3: Projections onto convex sets example for two closed and convex sets C_1 and C_2 .

few years the demand for denser seismic traces has increased a lot. Most famous methods are based on transformation of seismic data into another domain like the Radon or curvlet. Transform based methods are discussed in [5, 53, 54]. Similarly there are some techniques based on filters as discussed in [55]. Berkhout and Verschuur uses the primary reflection energy for the interpolation [57]. Interferometric interpolation of missing seismic data is discussed in [59]. Compressive sensing has been also proposed for the interpolation of seismic traces some examples are in [60, 61, 83–85].

Here, a new method of interpolation is proposed for the seismic data $g(x, t)$. Let the size of the \mathbf{g} be $MN \times 1$, where \mathbf{g} is the algebraic form of data $g(x, t)$. Also, L traces are missing from the total N traces. The proposed method is based on POCS and it involves the following sets:

- Set C_1 is the set of all real values sequences of length $MN \times 1$ and with at most K nonzero members in the Radon domain ‘ \mathbf{m} ’, where, mathematically:

$$C_1 = \{ \mathbf{g} \in \mathbb{R} \quad \text{with} \quad \mathbf{g} \leftrightarrow \mathbf{m} : m[i, j] = m[i, j] \quad \text{for} \quad n \in S \quad \text{and} \quad (4.4)$$

$$m[i, j] = 0 \quad \text{for} \quad n \in S^c \}$$

where $S = 0, 1, \dots, K - 1$, S^c is the compliment of S and $1 \leq i \leq p_s, 1 \leq j < \tau_s$ with p_s and τ_s represent the total number of elements in p and τ direction.

- Set C_2 is the set of all real values sequences of length $MN \times 1$ and with

bound on Radon domain ‘ \mathbf{m} ’. Mathematically,

$$C_2 = \mathbf{g} \in \mathbb{R} \quad \text{with} \quad \mathbf{g} \leftrightarrow \mathbf{m} : \gamma \leq m[i, j] \leq \beta \quad (4.5)$$

where $1 \leq i \leq p_s, 1 \leq j < \tau_s$ with p_s and τ_s presenting the total number of elements in p and τ direction, respectively. Furthermore, γ and β are the thresholding operators, which depends upon the iterations. The thresholding operators are calculated linearly with each iteration and as the number of iterations increases, the error decreases and hence the thresholding parameter increases. For this application, following values of γ and β were used:

$$\gamma_k = \frac{c}{k}, \quad \beta_k = \max(|\mathbf{m}|),$$

where k is the iteration number and c is a constant which depend on the number of non-zero element in \mathbf{m} .

- Set C_3 is the set of all real values sequences of length $MN \times 1$ with L location of missing indexes. Mathematically:

$$C_3 = \{\mathbf{g} \in \mathbb{R} : g_{orig}[m, n] = g[m, n] \quad \text{for} \quad n \in T \quad \text{and} \quad (4.6)$$

$$g_{orig}[m, n] = g_{orig}[m, n] \quad \text{for} \quad n \in T^c\}$$

where $T = 0, 1, \dots, L - 1$, and T^c is the compliment of T . Furthermore, $1 \leq m \leq M, 1 \leq n \leq N$ and g_{orig} is the original seismic data.

Now, one can show that all three sets are convex and closed. According to the

projections on to the convex sets theory, the missing traces can be obtained by the following:

$$\mathbf{g}_{k+1} = P_{C_3}P_{C_2}P_{C_1}\mathbf{g}_k, \quad (4.7)$$

where k is the number of iterations. Now, Projection of \mathbf{g}_k onto C_1 is given by:

$$\mathbf{f}_{1,k} = P_{C_1}\mathbf{g}_k \leftrightarrow \begin{cases} m[i, j] = 0 & \text{if } nnz(\mathbf{m}) > K \\ m[i, j] = m[i, j] & \text{if } nnz(\mathbf{m}) < K \end{cases} \quad (4.8)$$

where $nnz(\cdot)$ represents the number of non zero elements.

Projection of $\mathbf{f}_{1,k}$ onto C_2 is given by:

$$\mathbf{f}_{2,k} = P_{C_2}\mathbf{f}_{1,k} \leftrightarrow \begin{cases} m[i, j] = 0 & \text{if } |m[i, j]| < \gamma_k \\ m[i, j] = \beta_k & \text{if } |m[i, j]| \geq \beta_k \\ m[i, j] = m[i, j] & \text{otherwise} \end{cases} \quad (4.9)$$

Finally, Projection of $\mathbf{f}_{2,k}$ onto C_3 is given by:

$$\mathbf{f}_{3,k} = P_{C_3}\mathbf{f}_{2,k} \leftrightarrow \begin{cases} g[m, n] = g[m, 2] & \text{if } |g[m, n]| = 0 \\ g[m, n] = g[m, n] & \text{if } |g[m, n]| \geq 0 \end{cases} \quad (4.10)$$

The overall POCS based Radon transform interpolation method can be summarized as follows:

1. Find the index of the missing traces in $g(x, t)$.
2. Take the Radon transform of $g(x, t)$ to obtain $m(-, \tau)$.

3. Use the convex sets projections described in Equation 4.8 -4.9, to obtain the sparse and thresholded Radon domain $m(-, \tau)$.
4. Take the inverse Radon domain to obtain the estimated $g(x, t)$.
5. Replace the estimated traces into the original data by using the projection described by Equation 4.10.
6. Repeat until the error is less than the desired value.

Here $-$ in $m(-, \tau)$ represents that the proposed method can be applied using linear or parabolic Radon transform.

4.3 Simulation Results

The proposed POCS and Radon transform based method of finding missing traces was tested for 2-D and 3-D real seismic datasets.

4.3.1 2-D Data with linear events

The parameters of the synthetic seismic shot gather are presented in [14]. The data contain ground-roll, head waves, and three reflectors as shown in Figure 4.4(a). The total number of traces in the data is 120 ($N = 120$) with spatial sampling interval 25m and sampling interval 4ms. Among these 40 traces were randomly missing. POCS with linear Radon transform was used for interpolation of missing seismic traces. Figure 4.4(b) shows the $\tau - p$ domain for the first iteration of the proposed method. Now, based on the projections onto convex sets C_2 and

C_1 steps of the algorithm (Equations 4.8 and 4.9), the result after thresholding is presented in Figure 4.4(c). The effect of thresholding can be seen in Figure 4.4(c), where only the strong events are present. Similarly, after projections onto convex set C_3 of the algorithm (Equations 4.10) the result is presented in Figure 4.4(d). Figure 4.4(d) shows the result after the application of the inverse Radon transform and replacing the missing traces with the estimated traces. Although, some of the traces have been estimated correctly, however, the overall result is far from the original seismic data (Figure 4.4(a)). And to improve the resolution of the estimated missing traces, the algorithm was repeated several times, and the results after the application of 15 iterations of POCS is presented in Figure 4.4(d). The resulted image contains the missing traces, where almost all of the missing traces have been estimated correctly.

Noise Analysis:

To test the robustness of the proposed method data with different noise levels was tested. The total number of traces and the number of missing traces remain same. The result, after the addition of the noise with 0.1 standard deviations and 40 missing traces, is shown in Figure 4.5(a). The proposed method was used to estimate the missing traces and result after the first iteration is presented in Figure 4.5(b). As, it can be seen from the result that the interpolated traces are far from ideal, therefore, to increase the accuracy the POCS is used for several iterations, and the result after the 25 iterations is presented in Figure 4.5(c). Similar comparison after addition of white noise with standard deviation 0.4 is presented in

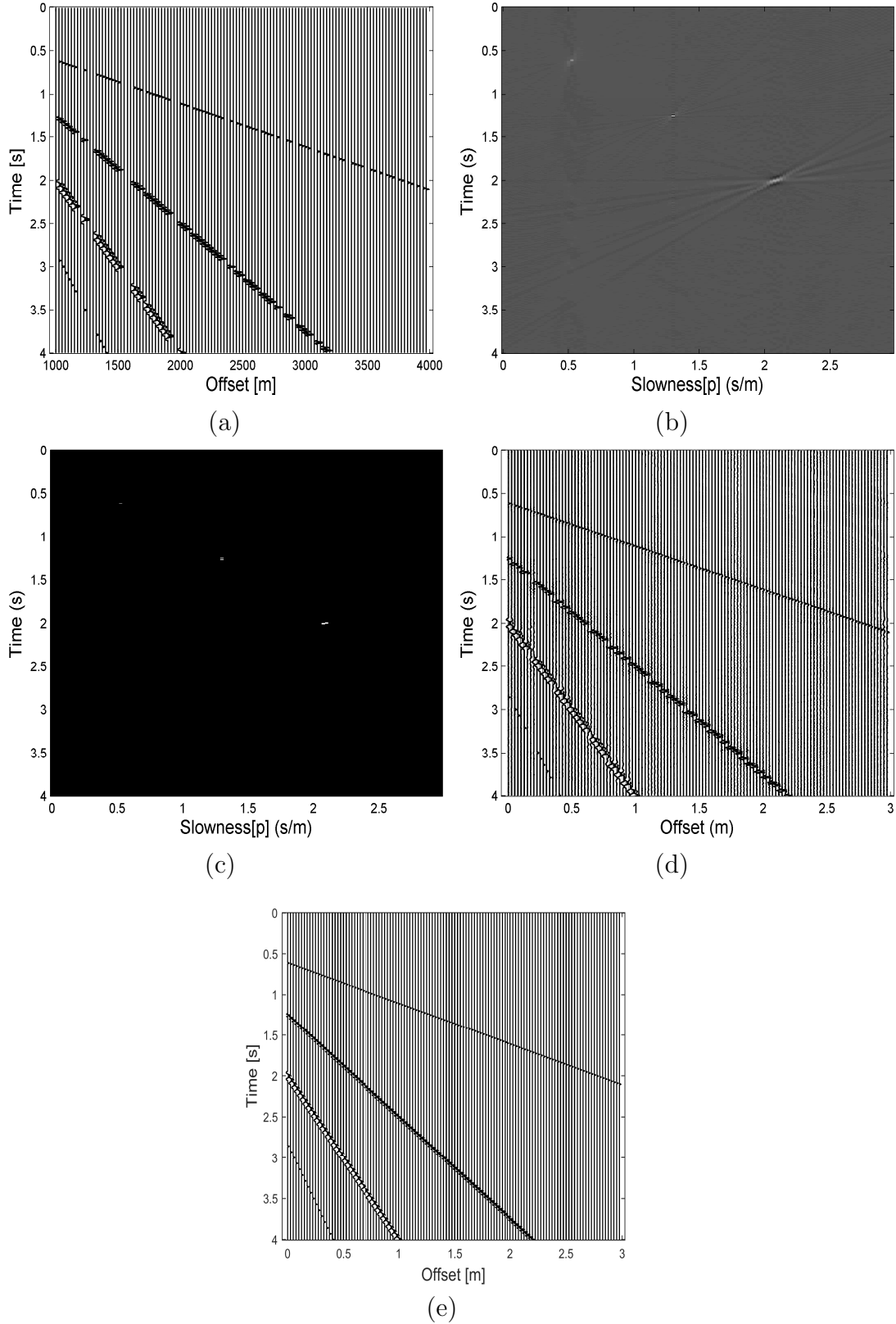


Figure 4.4: (a) The synthetic seismic data. (b) The $\tau - p$ transform of (a). (c) The $\tau - p$ domain after performing thresholding of (b). (d) The interpolated data after applying the inverse $\tau - p$ transform on (c) and replacing the missing traces after first iteration. (e) Interpolation after 15 iterations.

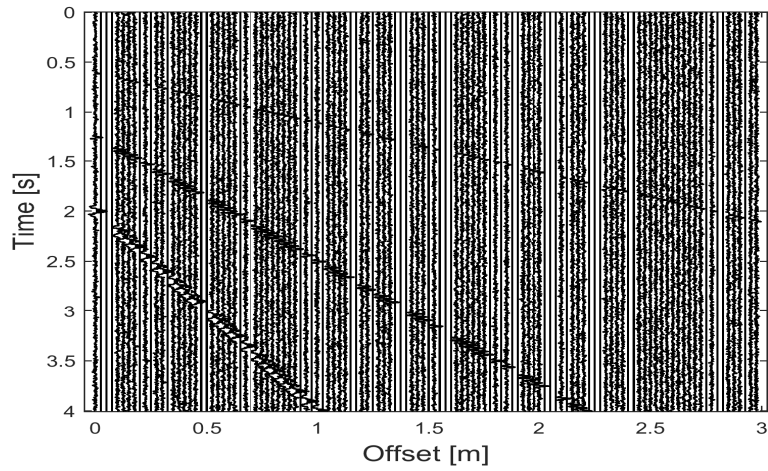
Figure 4.6. With this high level of noise, the linear events are completely missing from Figure 4.6(a), which makes manual interpolation virtually impossible. However, the linear interpolated events are fairly clear in Figure 4.6(c), which presents the results after the interpolation using POCS and linear Radon transform.

4.3.2 2-D Data with non-linear events

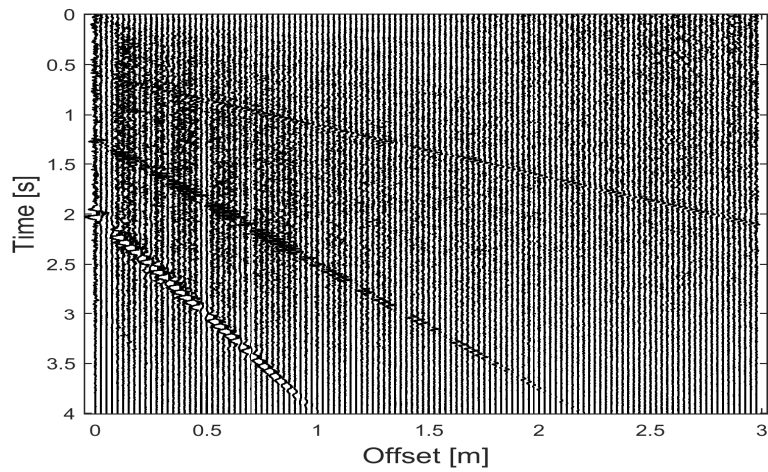
The proposed formulation, of POCS using parabolic Radon transform, was tested on the data [86] as shown in the Figure 4.7. The total number of traces in the data is 481. Out of these 481 traces 161 traces are missing. Figure 4.7 shows the result of the proposed algorithm. From the interpolated data, it can be deduced that besides interpolation the resolution of the curves also increased proposed method interpolates the missing traces even for high noise levels and low compression levels.

The algorithm was also tested with another synthetic data set along with two events as shown in Figure 4.8(a). The total number of traces in the data are 100 with spatial sampling interval 25m and sampling interval 4ms. Among these 40 traces are randomly missing (see Figure 4.8(b)). Figure 4.8(c) presents the data after the interpolation.

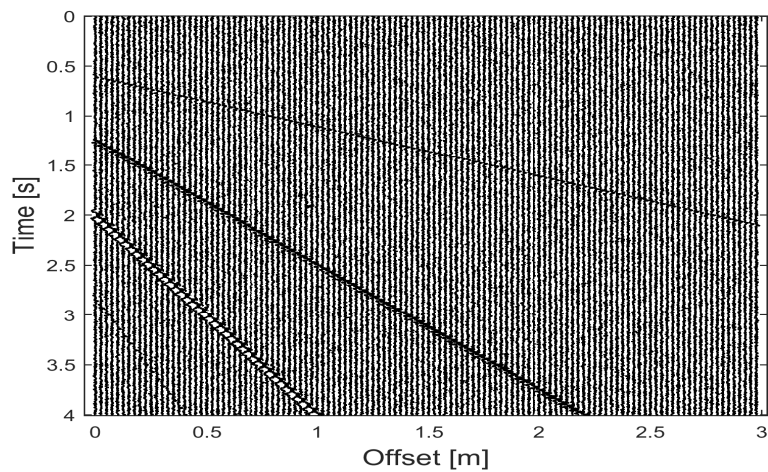
To test the robustness of the proposed setup, data with different noise level is tested. Total number of traces and number of missing traces remains same. The results after the addition of the noise with 0.3 standard deviation and 40% compression are presented in Figure 4.9.



(a)

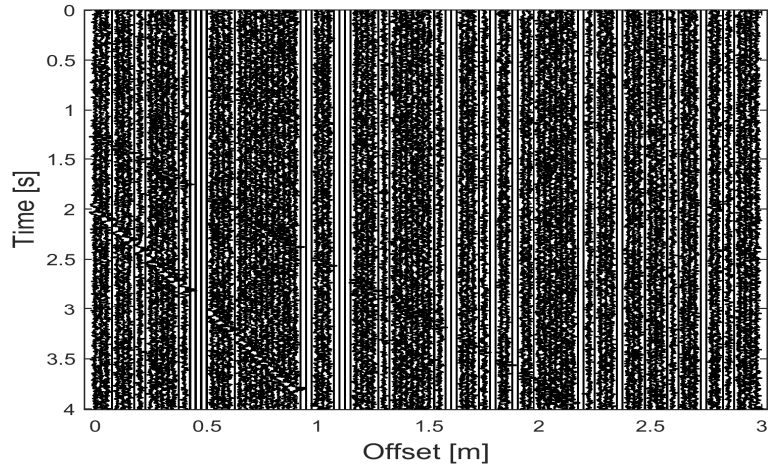


(b)

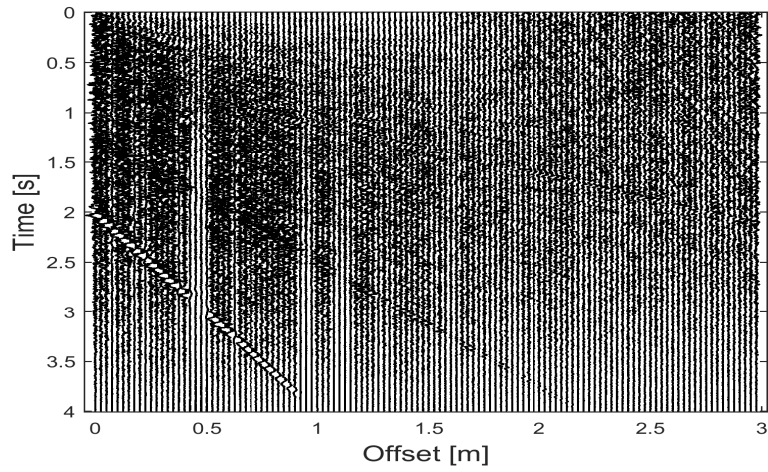


(c)

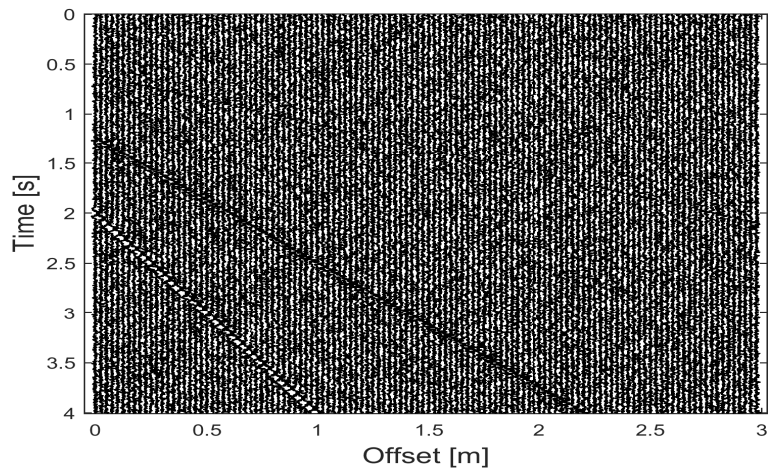
Figure 4.5: (a) The synthetic seismic data with 10% random Gaussian noise and 40 missing traces. The interpolated data after first iteration (b) and after 25 iterations (c).



(a)

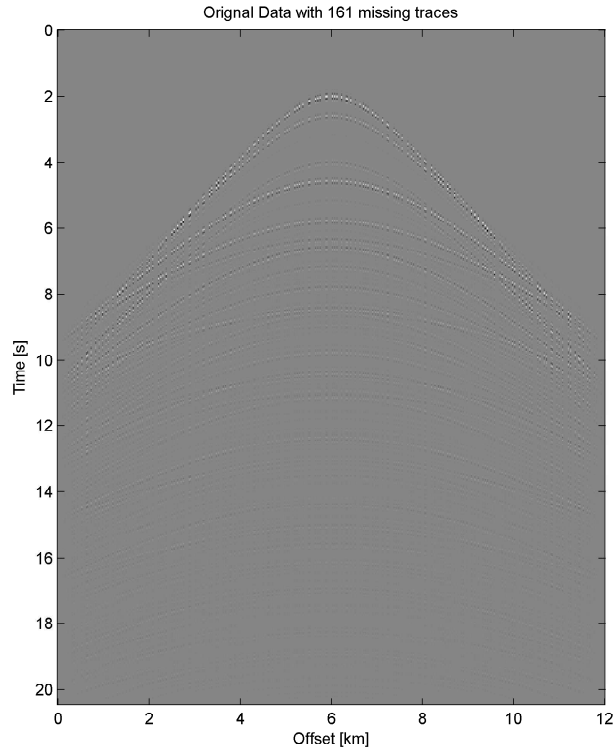


(b)

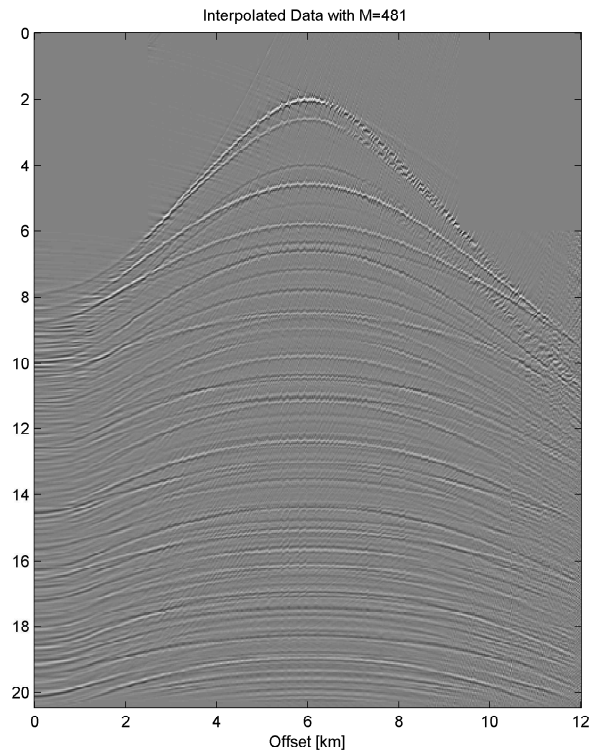


(c)

Figure 4.6: (a) The synthetic seismic data with 40% random Gaussian noise and 40 missing traces. The interpolated data after first iteration (b) and after 25 iterations (c).

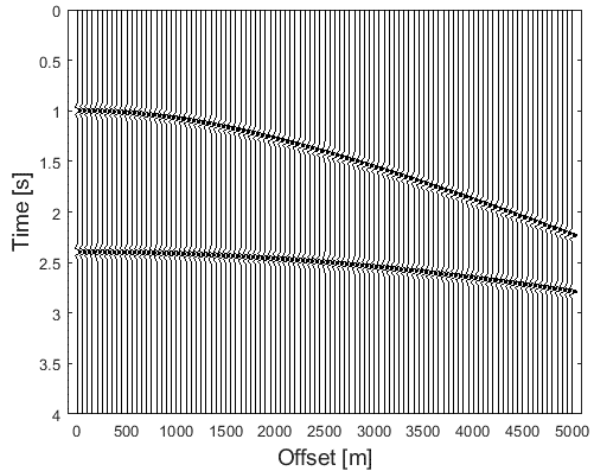


(a)

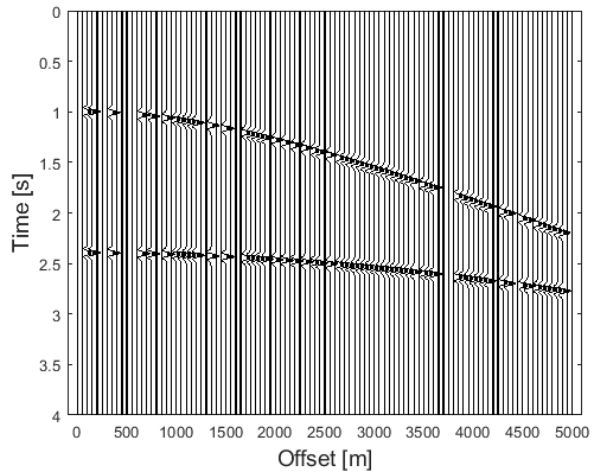


(b)

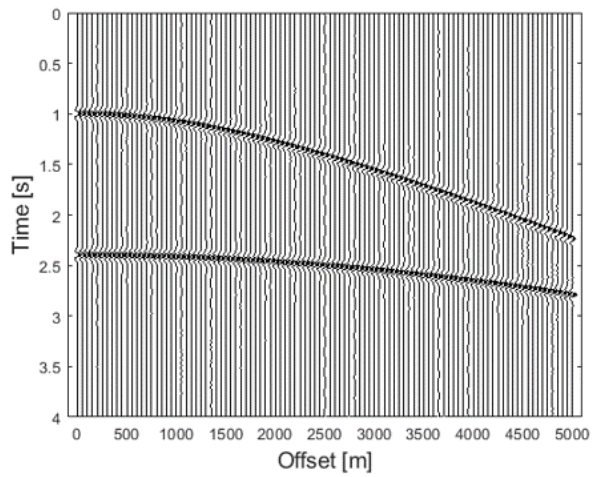
Figure 4.7: (a) Interpolation of missing seismic traces using Radon transform with total number of traces 481 with 161 missing traces.(b) Interpolated data with POCS and parabolic Radon transform.



(a)

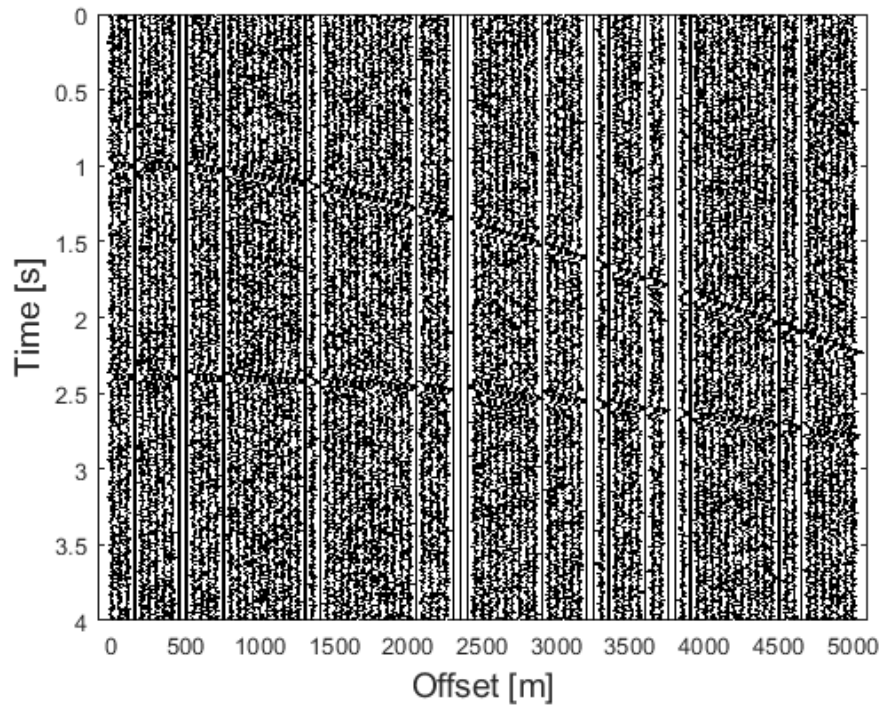


(b)

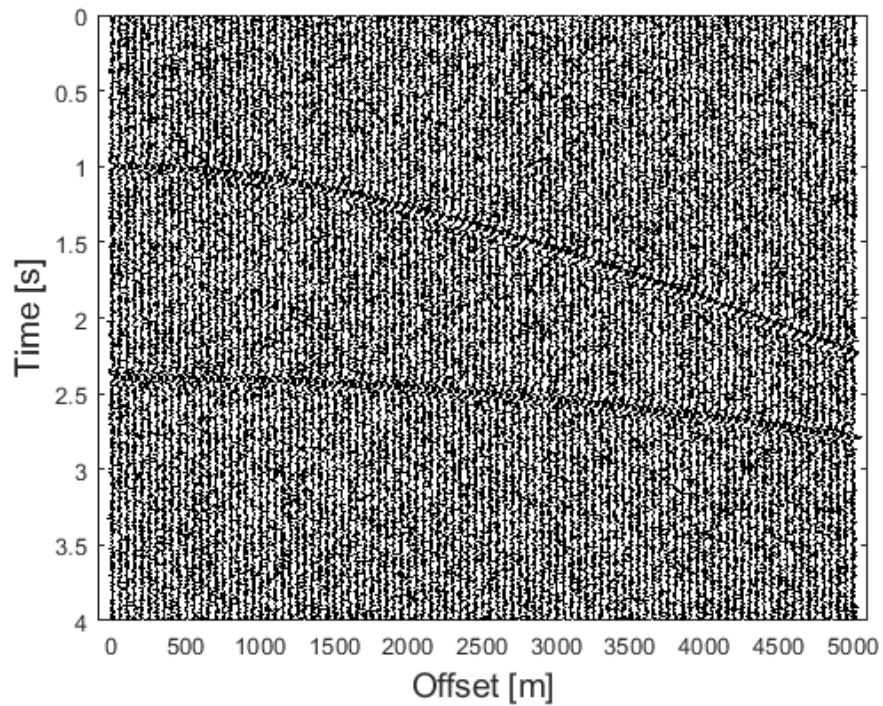


(c)

Figure 4.8: (a) The synthetic seismic reflected data and (b) data after 40 missing traces. (c) The interpolated data after applying the POCS with parabolic Radon transform.



(a)



(b)

Figure 4.9: (a) The synthetic seismic refracted data with 30% random Gaussian noise. (b) The interpolated data after using the POCS with parabolic Radon transform.

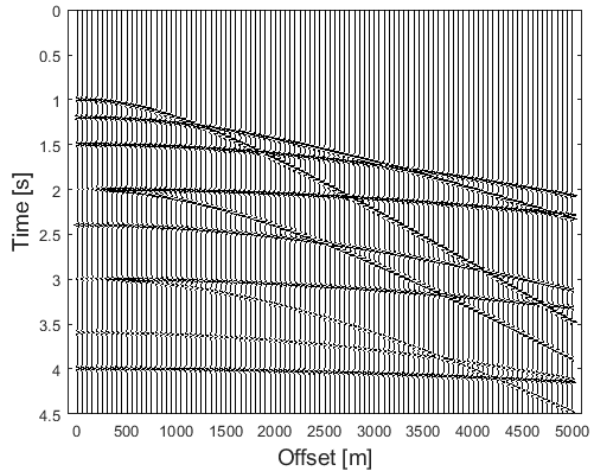
To further test the performance of the proposed Radon transform, it was applied to a data set with 10 seismic events, as shown in Figure 4.10(a). Total number of traces are 100 with spatial sampling of 50 m and sampling time 4 ms. The data with 30 missing traces is presented in Figure 4.10(b). The proposed method was used for the interpolation and the result after the interpolation is presented in Figure 4.10(c). Figure 4.10(c) shows that all the events are interpolated.

Comparison with Existing Methods:

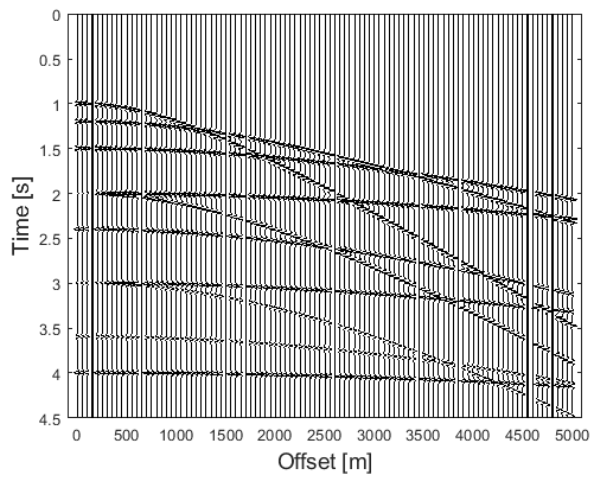
To test the effectiveness of the proposed method it was compared with the existing Radon transform. Figure 4.11 presents the result after the application of the CG-FFT based high resolution Radon transform. The results shows that there are some artifact at the far offset and the interpolation data is not accurate (Figure 4.11(d)). Similar results for a low- resolution Radon transform are presented in Figure 4.12. From Figure 4.12, it can be seen that the resolution of interpolated seismic data is low and events have low amplitudes. From the results in Figures 4.10 and 4.11 it is clear that the proposed method outperforms the traditional methods. Furthermore, the proposed method is suitable for far-offset seismic data where the existing techniques does not work.

Noise Analysis:

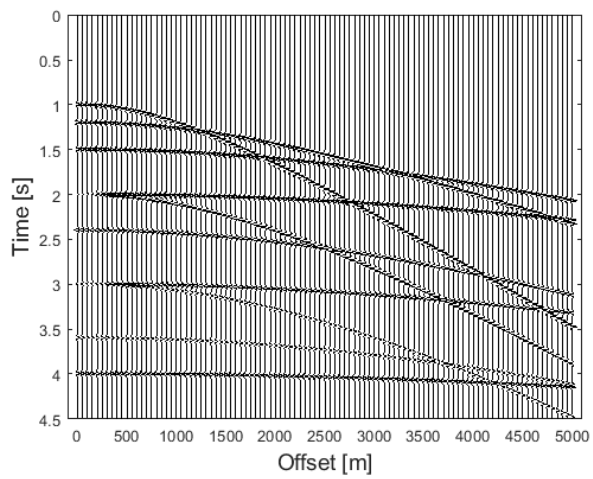
Furthermore, to test the robustness of the proposed method, it was tested with 30% noise. Figure 4.13(a) shows the data with 30% noise and 20 sample missing.



(a)

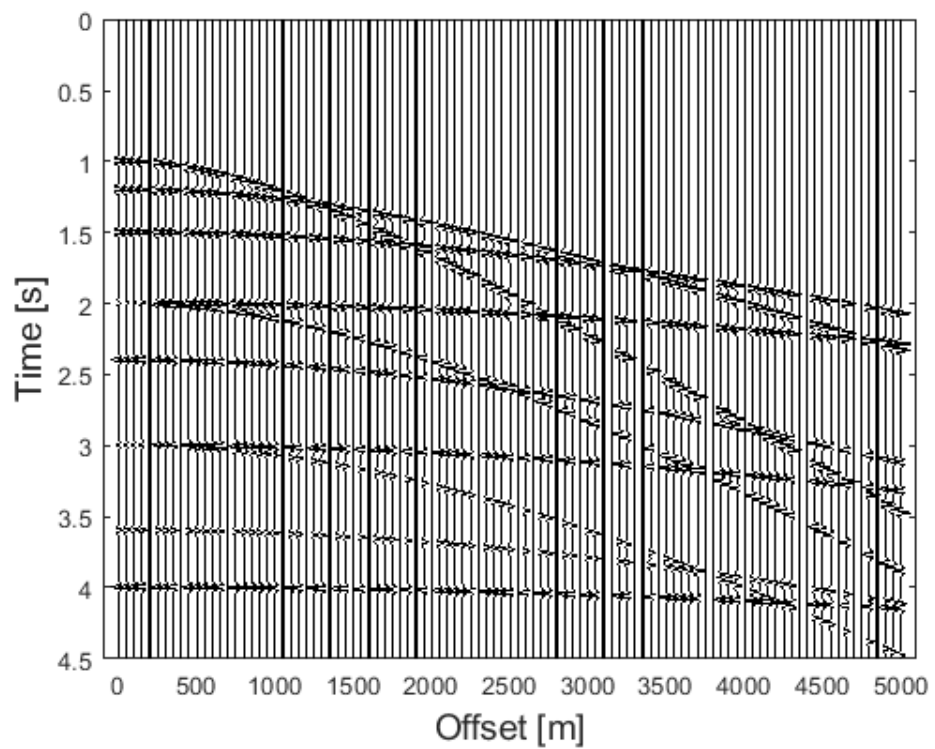


(b)

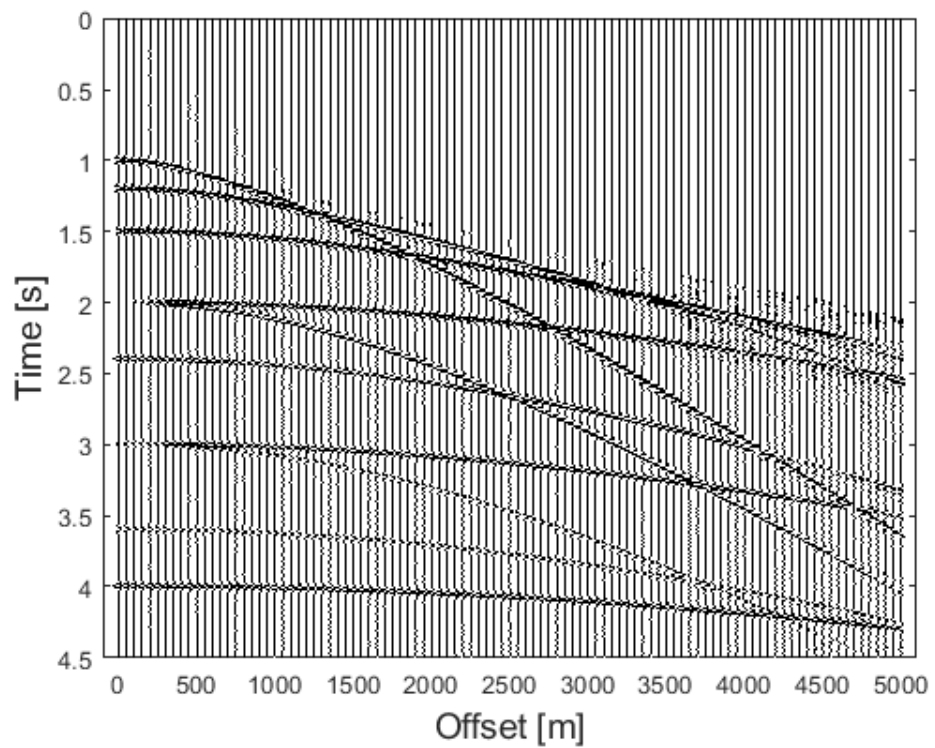


(c)

Figure 4.10: (a) The synthetic seismic reflected data. (b) The data with 30 missing traces. (c) The interpolated data after applying the POCS with parabolic Radon transform.

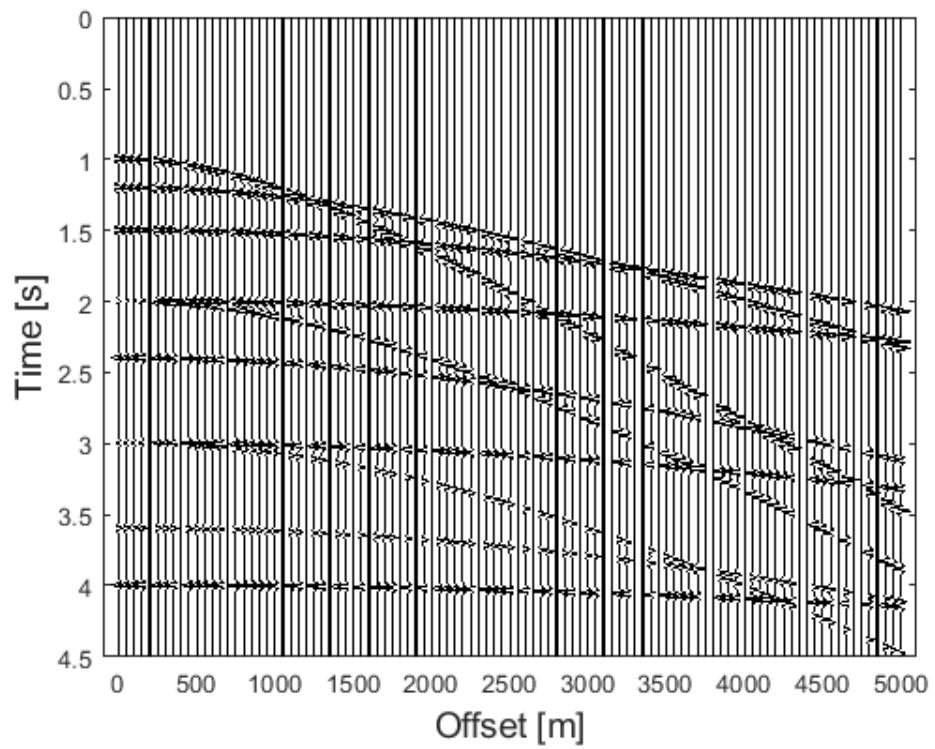


(a)

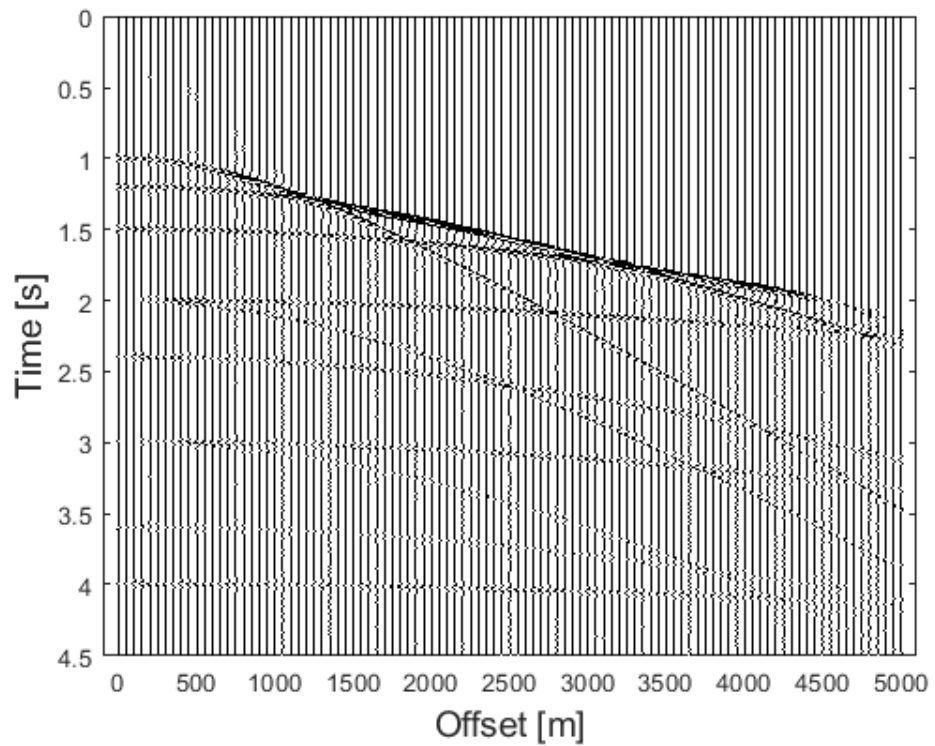


(b)

Figure 4.11: (a) The synthetic seismic reflected data with 30% compression and its interpolated version using CGG-FFT based Radon transform is presented in (b).



(a)



(b)

Figure 4.12: (a) The synthetic seismic reflected data with 30% compression and its interpolated version using least square Radon transform is presented in (b).

Table 4.1: Mean squared error for the proposed POCS based Radon transform method versus other Radon transform methods for Figure 4.10(a).

Method	Noise	MSE
Angle-based Radon transform	-	0.0065
Low-resolution Radon transform (Levinson, Least Squares)	-	0.065
Fast high-resolution Radon transform (CG-FFT)	-	0.0095
Angle-based Radon transform	10%	0.0066
Low-resolution Radon transform (Levinson, Least Squares)	10%	0.070
Fast high-resolution Radon transform (CG-FFT)	10%	0.0097
Angle-based Radon transform	30%	0.0067
Low-resolution Radon transform (Levinson, Least Squares)	30%	0.04
Fast high-resolution Radon transform (CG-FFT)	30%	0.0105

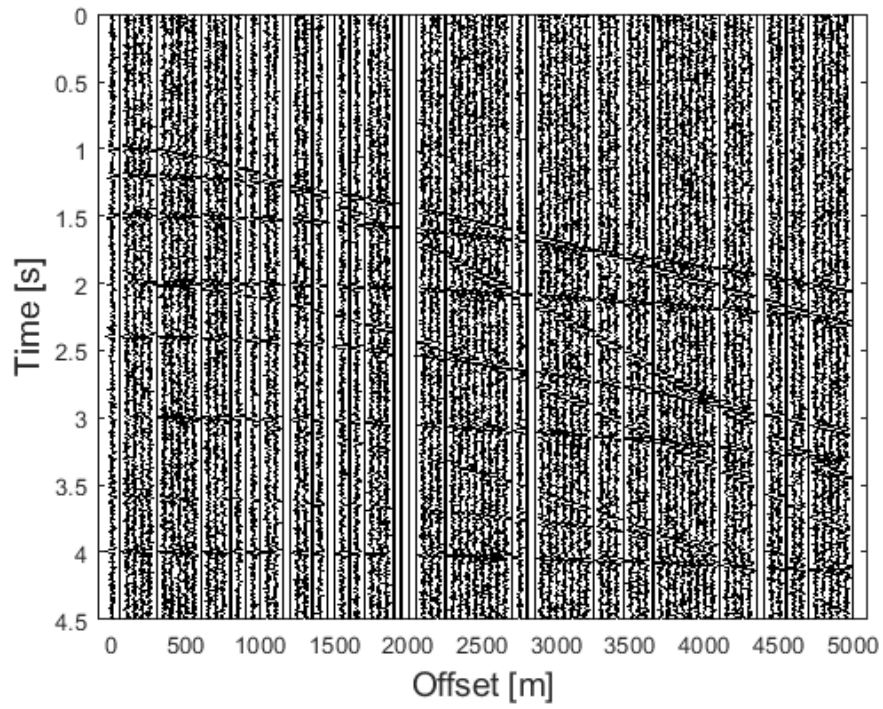
POCS based parabolic Radon transform was used to interpolate the data as shown in Figure 4.13(b).

Quantitative Analysis:

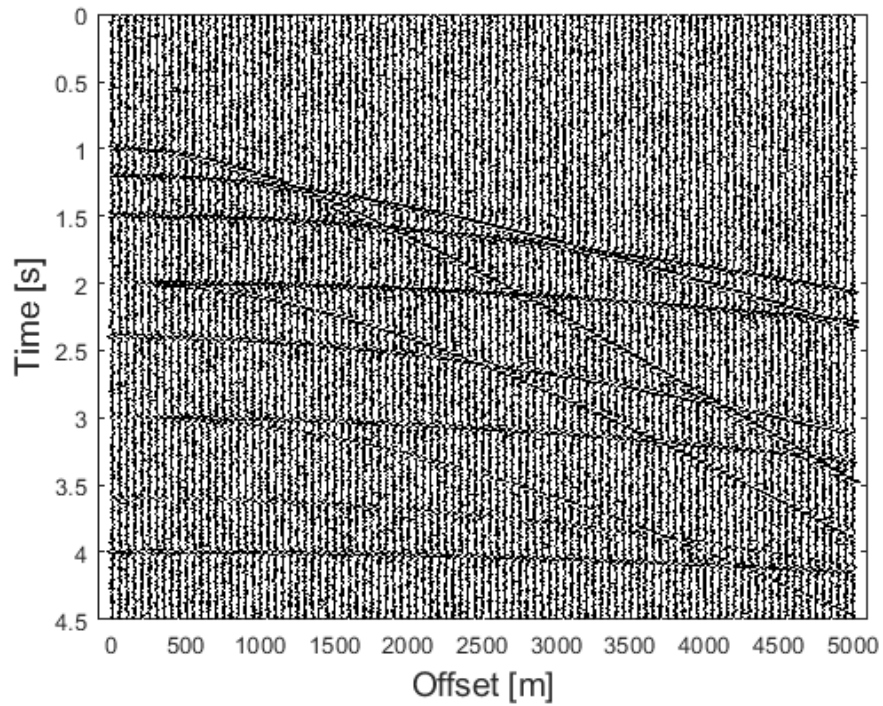
To compare the accuracy of the proposed method, the original data (Figure 4.10(a)) was compared quantitatively with the proposed and existing methods of Radon transforms. The results are summarized in Table 4.1. From Table 4.1, it is evident that the results for proposed method are more accurate than those of existing methods for Radon transforms.

4.3.3 3-D Real Marine data

The POCS based method was also applied for the interpolation of the 3-D real marine seismic data. For the 3-D data, the interpolation was performed along



(a)



(b)

Figure 4.13: (a) The synthetic seismic reflected data with 30% noise and its interpolated version is presented in (b).

the cross-line and in-line direction using the proposed method. The real data from Waihapa, New Zealand ¹ was used for the testing of the interpolation. The data is presented in Figure 4.14. The proposed method was applied to in-line and cross-line dimension separately. In-line 211 is shown in Figure 4.15(a). The data with 20 % missing traces is presented in Figure 4.15(b). By applying one iteration of POCS based Radon transform the interpolated data is presented in Figure 4.15(c), which shows the need for several iteration of the proposed method. The interpolated data in the Figure 4.15(d) is the result of the POCS based Radon transform technique after 100 iterations.

Similarly, the interpolation was also applied to the cross-line number 153 of the 3-D data base. The data and the missing data are presented in Figures 4.16(a)-(b). The result after the interpolation of missing data is shown in Figure 4.16(c). The difference between the actual and interpolated is not visible form the naked eye. For the comparison, the same data base is used with CG-FFT based Radon transform. The results for cross-line direction are presented in Figures 4.17. From the simulation results for the CG-FFT based Radon transform, it is evident that it is not efficient as compared to the proposed method. To put the results quantitatively, the error was calculated between the actual data and the interpolated data. Table 4.2 shows the error for proposed method and traditional Radon transform which also shows that the proposed method outperforms the traditional methods.

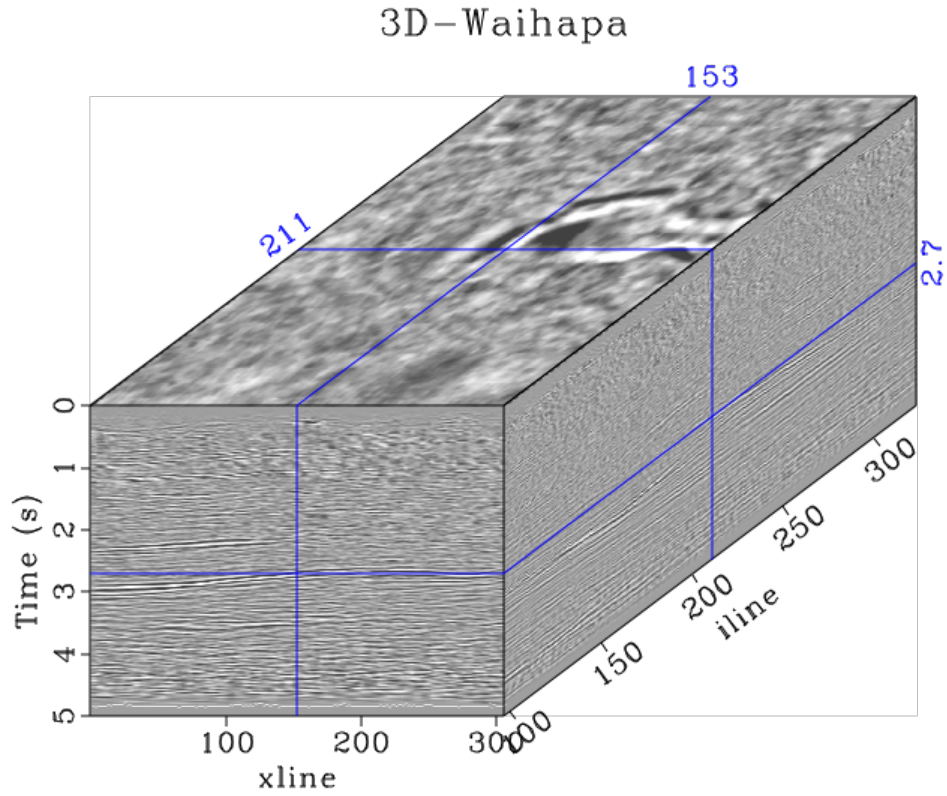


Figure 4.14: 3-D Real Data from Waihapa, New Zealand (Courtesy of New Zealand Petroleum and Minerals (NZPM)).

Table 4.2: Mean squared error for the proposed angle-based Radon transform method versus other Radon transform methods for 3-D Real Dataset.

Method	MSE
Angle-based Radon transform	0.0095
Low-resolution Radon transform (Levinson, Least Squares)	0.155
Fast high-resolution Radon transform (CG-FFT)	0.0145

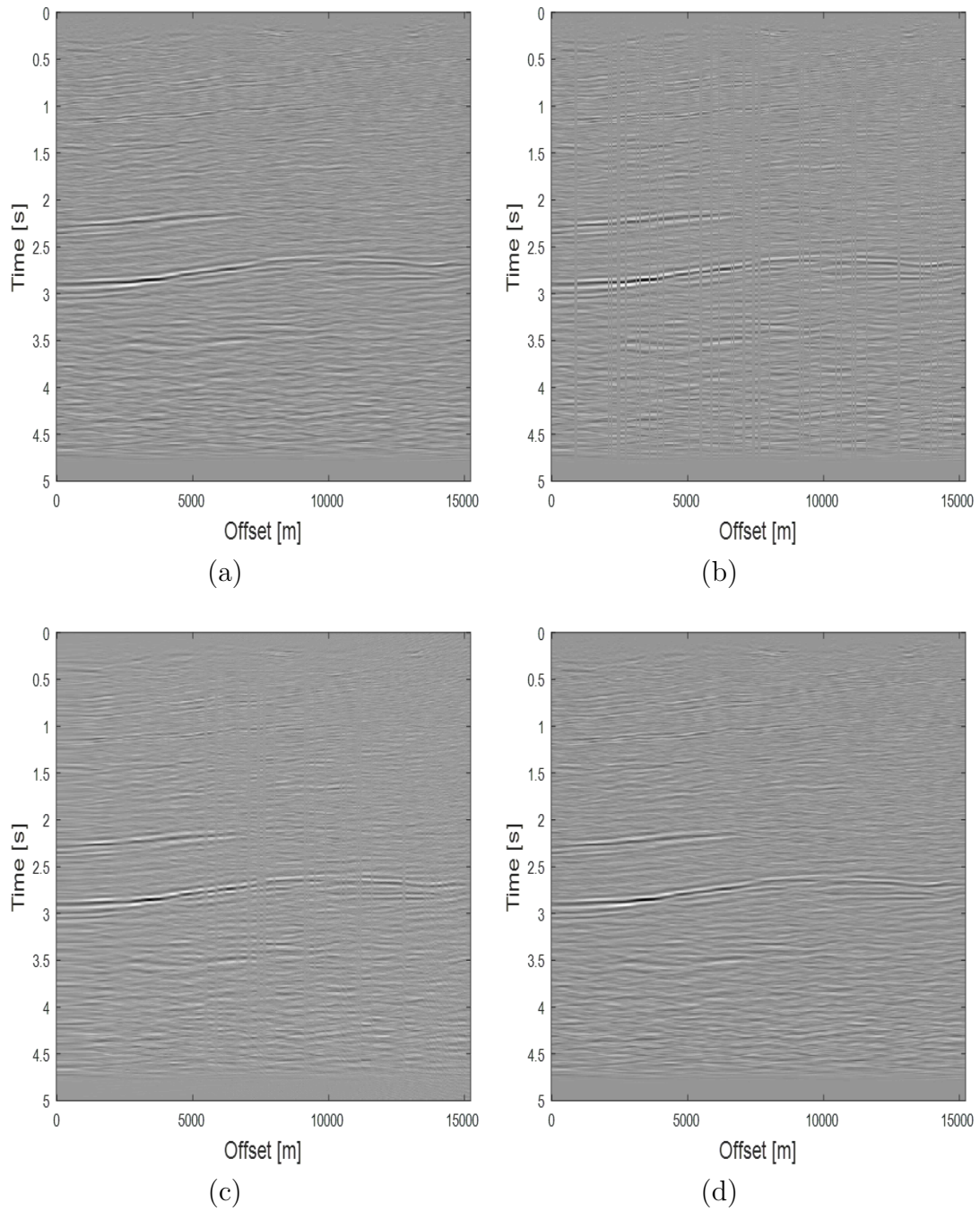


Figure 4.15: (a) The real in-line data from the Waihapa, New Zealand (Courtesy of New Zealand Petroleum and Minerals (NZPM)). (b) The data with 20 % missing traces. (c) The interpolated data after 1 iteration of the proposed method. (d) The interpolated data after 100 iterations.

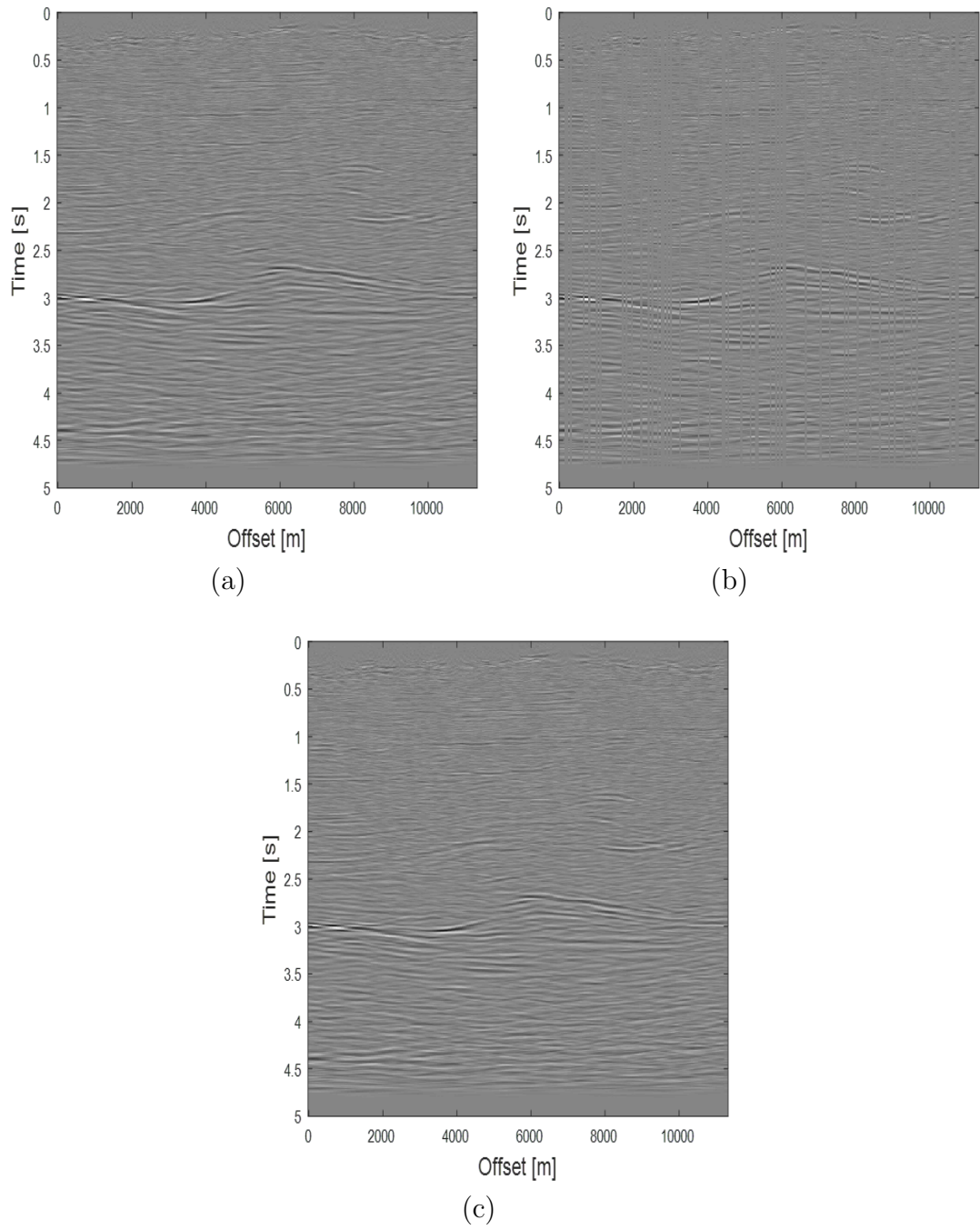
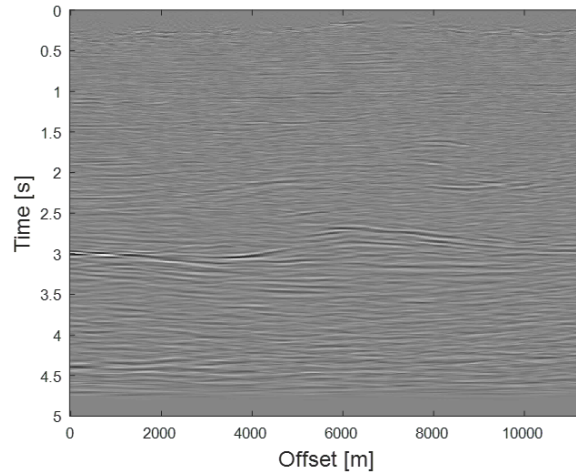
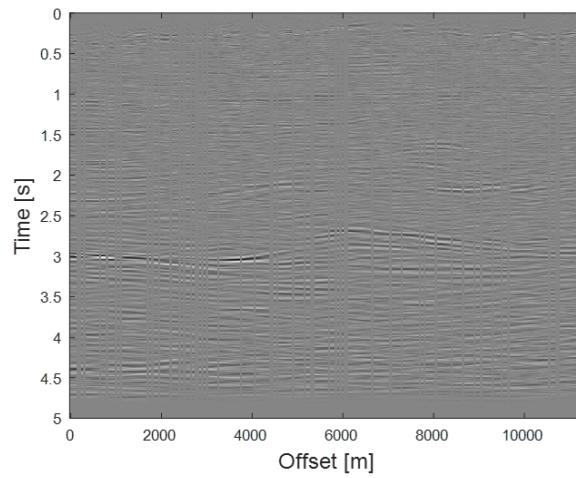


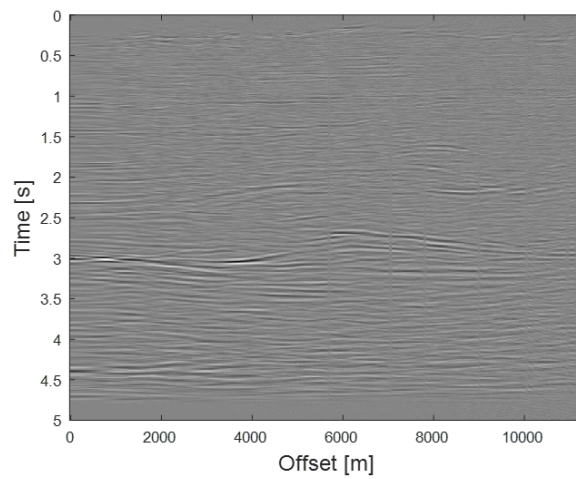
Figure 4.16: (a) The real cross-line data from the Waihapa, New Zealand (Courtesy of New Zealand Petroleum and Minerals (NZPM)). (b) The data with 20 % missing traces of proposed method. (c) The interpolated data after 100 iterations.



(a)



(b)



(c)

Figure 4.17: (a) The real cross-line data from the Waihapa, New Zealand (Courtesy of New Zealand Petroleum and Minerals (NZPM)). (b) The data with 20 % missing traces. (c) The interpolated data after 100 iterations.

4.4 Conclusion

A new method for interpolation of missing seismic traces is discussed in this chapter. The proposed method utilizes the projection on to the convex sets for the missing trace problem. From the detailed simulation results, it is clear that Radon transform with POCS not only interpolates the seismic data, but also, it is quite robust and provides an accurate estimation of the missing seismic traces even in the presence of the noise.

CHAPTER 5

AN EFFICIENT HYPERBOLIC RADON TRANSFORM

On common shot point gathers, seismic events are not linear in nature but they are hyperbolic in nature. For the hyperbolic events, hyperbolic Radon transform can be utilized which maps the hyperbolic events of the CMP gathers to points. However, due to the complexity of the hyperbolic Radon transforms, they are computationally quite expensive to realize and, therefore, they are not used much for the seismic data processing.

In this chapter, hyperbolic Radon transform is revisited and a newer efficient way is proposed for the fast computation of the hyperbolic Radon transform. In the first section, hyperbolic along with apex shifted hyperbolic Radon transform are discussed. It will be followed by the proposed method of the hyperbolic Radon transform. Finally, it will be tested on 2D and 3-D seismic data and computationally comparison will be presented.

5.1 Introduction

As already described in Chapter 2, it was Thorson, who suggested a time domain hyperbolic least-squares method in 1995, which can give a high resolution result at the expense of very large matrix computation. The shifted-hyperbolic Radon transform was introduced by Oppert and Brown [38], which also consider the apex of the hyperbolic events, resulting in an even higher variant of Radon transform. With the availability of high power computing, the feasibility of time domain Radon transform is increasing and it has been proposed in many different ways [41–45].

We already have introduced the generalized Radon Transform in time domain and frequency domain as:

$$u(q, \tau) = \int_{-\infty}^{\infty} g(x, t = \phi(x; q, \tau)) dx, \quad (5.1)$$

$$\hat{g}(x, t) = \int_{-\infty}^{\infty} u(q, \tau = \phi(q; x, t)) dq, \quad (5.2)$$

where $g(x, t)$ is the CMP shot gathered, t is the two way time, $u(q, \tau)$ is transform domain, q is representing the curvature, and τ is the time intercept.

In case of hyperbolic Radon transform, we have:

$$t = \sqrt{\tau^2 + qx^2}, \quad (5.3)$$

where $q = \frac{1}{v_{rms}^2}$. Hyperbolic Radon transform in mathematical form is given by:

$$u(q, \tau) = \int_{-\infty}^{\infty} g(x, t = \sqrt{\tau^2 + qx^2}) dx, \quad (5.4)$$

$$\hat{g}(x, t) = \int_{-\infty}^{\infty} u(q, \tau = \sqrt{t^2 - qx^2}) dq. \quad (5.5)$$

Similarly, in discrete form, the hyperbolic Radon transform is represented as:

$$u(q, \tau) = \sum_x g(x, t = \sqrt{\tau^2 + qx^2}), \quad (5.6)$$

$$\hat{g}(x, t) = \sum_q u(q, \tau = \sqrt{t^2 - qx^2}). \quad (5.7)$$

Figure 5.1 shows an example of the hyperbolic Radon transform.

5.1.1 The Shifted-Hyperbolic Radon transform

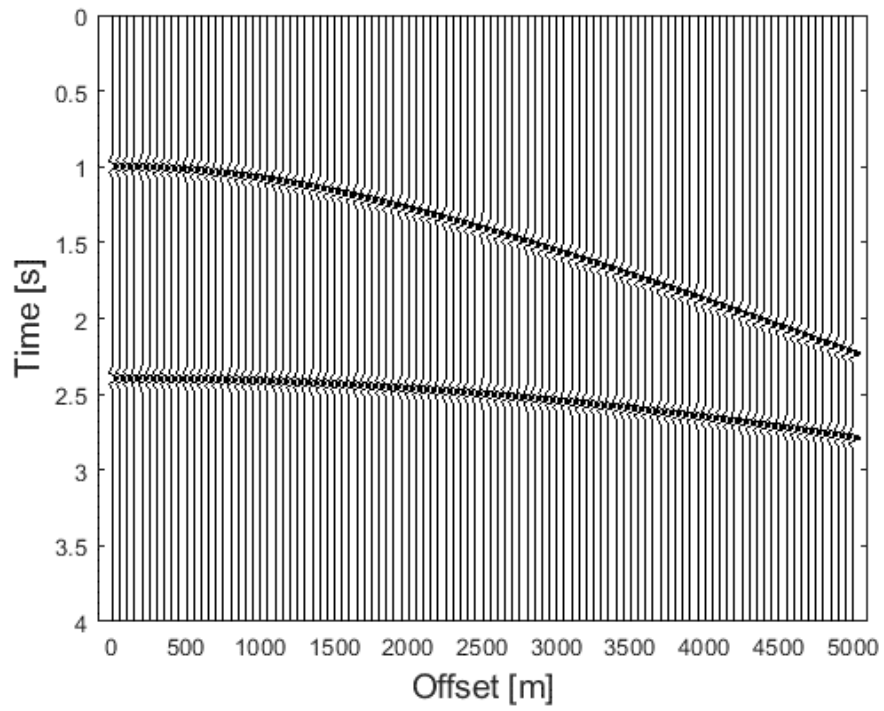
A typical travel time curve for a diffraction event is represented by following equation:

$$t = \sqrt{t^2 + (x_s - x_d)^2/v^2} + \sqrt{t_d^2 + (x_d - x_r)^2/v^2}, \quad (5.8)$$

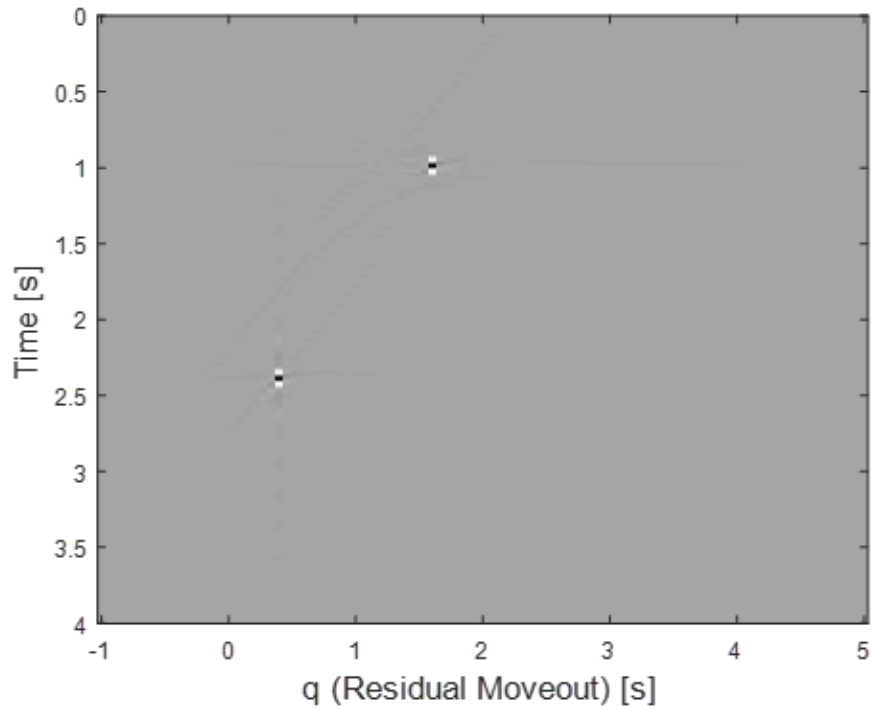
where t_d is the travel time, x_d is the diffractor location, x_s and x_r are the locations of sources and receiver, respectively.

For common shot gather the first term is constant and the equation 5.8 can be re-written as:

$$t = \tau_0 + \sqrt{t_d^2 + (x_d - x_r)^2/v^2}, \quad (5.9)$$



(a)



(b)

Figure 5.1: (a) The synthetic seismic reflected data. (b) The hyperbolic Radon transform of (a).

where $\tau_0 = \sqrt{t^2 + (x_s - x_d)^2/v^2}$.

As equation 5.9 shows that the travel time curve is considered as a hyperbolic curve, therefore, hyperbolic Radon transform produces the high resolution radon transform with better focusing of the non-linear seismic events, however, it will require to integrate over three different parameters and if size of the parameter is N then the complexity of the single iteration of the hyperbolic radon transform will be $O(N^3)$. Due to the large size of the seismic data it is not feasible to perform the integration or invert the matrices.

Coming back to the original travel time equation 5.9, the equation has three different parameter (x_d , τ_0 and v) over which one have to integrate to get the apex shifted hyperbolic Radon transform. Mathematically, the apex shifted hyperbolic Radon transform is given by:

$$u(v, \tau, \tau_0, x_d) = \int_{-\infty}^{\infty} g(x_r, t = \tau_0 + \sqrt{\tau^2 + (x_d - x_r)^2/v^2}) dx_r, \quad (5.10)$$

$$\hat{g}(x_r, t) = \int \int \int_{-\infty}^{\infty} u(v, \tau = \sqrt{t^2 - (x_d - x_r)^2/v^2} - \tau_0, \tau_0, x_d) dv d\tau_0 dx_d. \quad (5.11)$$

Similarly, for discrete case:

$$u(v, \tau, \tau_0, x_d) = \sum_{x_r} g(x_r, t = \tau_0 + \sqrt{\tau^2 + (x_d - x_r)^2/v^2}), \quad (5.12)$$

$$\hat{g}(x_r, t) = \sum_v \sum_{x_d} \sum_{\tau_0} u(v, \tau = \sqrt{t^2 - (x_d - x_r)^2/v^2} - \tau_0, \tau_0, x_d). \quad (5.13)$$

Due to the t^2 , this can not be solved by dividing into small sub problems

and solving separately for each frequency. The only way to solve is to solve the following inverse problem:

$$\mathbf{g} = \mathbf{L}\mathbf{u},$$

$$\hat{\mathbf{u}} = \mathbf{L}^T \mathbf{g},$$

where \mathbf{g} , \mathbf{m} , $\hat{\mathbf{u}}$ are the data, original and estimated Radon parameter. \mathbf{L} and \mathbf{L}^T represent the Radon and adjoint Radon operators as described in the Equations 5.12 and 5.13.

5.2 The Proposed efficient Hyperbolic Radon transform

Traditionally, the apex shifted hyperbolic Radon transform is solved by solving the Equations 5.12 and 5.13 in time domain and require a lot of time to compute it. Here, a new method to solve the apex shifted hyperbolic Radon transform is proposed which reduces the search space by first computing the adjoint operator $\hat{\mathbf{u}}$ which will provide an estimate of the parameters where hyperbolic parameters are more likely. Then, based on the estimates use the reduced parameter space to calculate the apex shifted hyperbolic Radon transform. So, in simple terms instead of integrating over the entire length of x_d , τ_0 and v , now, integration will be performed only to the fractions of these parameter. The overall algorithm is as follows:

1. Find the $\hat{\mathbf{u}}$ by frequency domain formulation or by integrating. This will give an estimate or low resolution hyperbolic Radon transform.
2. Based on the calculated Radon estimate, find the values of x_d , τ_0 , v for which the $\hat{\mathbf{u}}$ has a peak.
3. Now, based on the values of previous step, define the windows of fixed size for all these parameter. These windows will be used to integrate in the apex shifted hyperbolic Radon transform.
4. Now solve the inverse problem described by equations 5.12 and 5.13.

One thing to mention here is the effect of window size on the computation of the proposed model. The window size depends upon the data itself. If the data is low noise then a small size window can be used because for simple and clean data adjoint based hyperbolic Radon transform also performs well and the estimates are quite close to the high resolution apex shifted Radon transform. On the other hand, if the data has a lot of noise and it contains a lot of multiples then in that case larger window is suitable. Based on my experiments, a window of size 10×10 , which provides a trade off between the computational time and the resolution of the proposed apex shifted hyperbolic Radon transform. However, this can be investigated as future work.

5.2.1 Computational Efficiency

The original travel time equation 5.9 has three different parameter (x_d , τ_0 and v) over which one have to integrate to get the apex shifted hyperbolic Radon transform. For the seismic data of size $N_t \times N_{x_r}$ and $N_\tau = N_t$, the cost of adjoint operator is given by:

$$Cost_{adj} = N_\tau N_v N_{x_d}, \quad (5.14)$$

where N_v, N_{x_d} are the number of velocities and apex positions. Furthermore, the overall cost for a single iteration of apex-shifted hyperbolic Radon transform is given by:

$$Cost_{1f} = N_{x_r} N_\tau N_v N_{x_d}. \quad (5.15)$$

Similarly, the cost for k iterations is given by:

$$Cost_{kf} = k N_{x_r} N_\tau N_v N_{x_d}. \quad (5.16)$$

Equation 5.16 represents the number of mathematical operations needed for the basic implementation of the apex-shifted hyperbolic Radon transform.

Now, following the same argument, we can calculate the cost for the proposed method for apex-shifted hyperbolic Radon transform. According to the first step of the proposed method, we have to calculate the adjoint using traditional hyperbolic Radon transform, for which the cost is given by Equation 5.14. Now, the cost of next steps will depend upon the size of the window. Let the size of window, for a specific parameter, be $L \times L$ and the total number of elements be

N_w , where $N_w = L^2$. For proposed algorithm integration is performed only over the window N_w and based on that Equation 5.15 can be written as follows:

$$Cost_{1_p} = N_w N_w N_w N_w. \quad (5.17)$$

Overall cost of the proposed algorithm is given by:

$$Cost_{k_p} = (k - 1)Cost_{1_p} + Cost_{1_f} \quad (5.18)$$

$$= (k - 1)(N_w)^4 + N_{x_r} N_\tau N_v N_{x_d}. \quad (5.19)$$

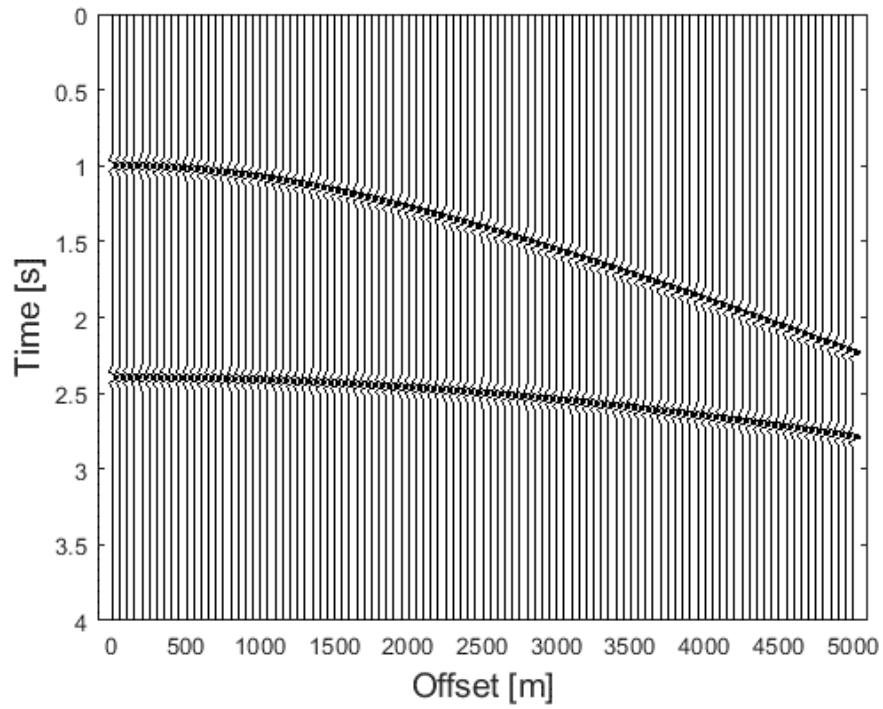
Since, $(N_w)^4 \ll N_{x_r} N_\tau N_v N_{x_d}$, therefore, the cost of proposed algorithm depend upon the number of iterations used to solve the inverse problem.

5.3 Simulation Results

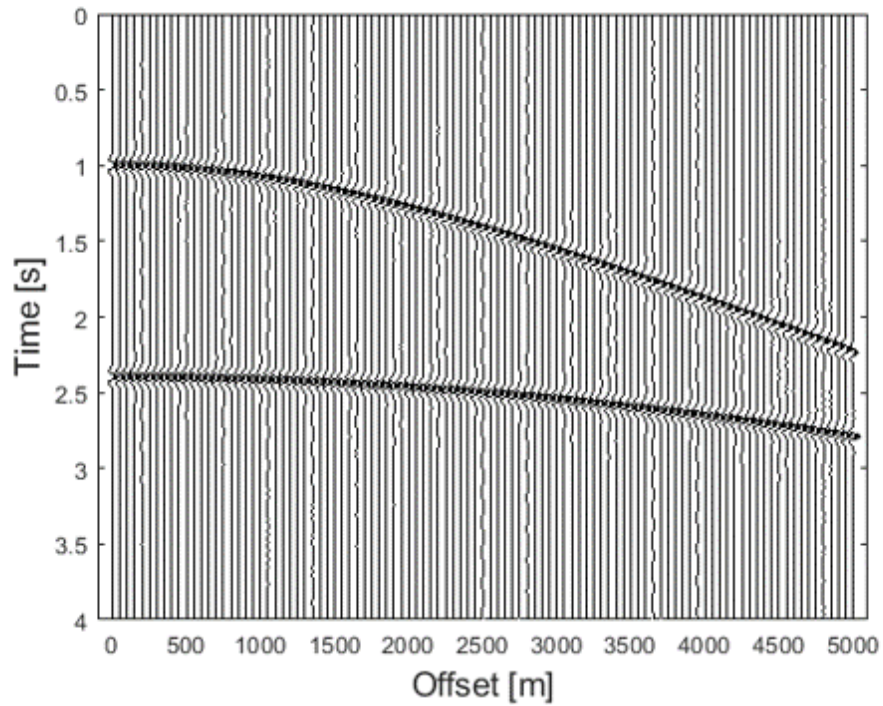
For testing, the seismic synthetic data was generated using a Ricker wavelet of 10 Hz and two reflection events (see Figure 5.2(a)). The total number of traces in the data were 50 with spatial sampling interval 150 *m* and sampling interval 8 *ms*. Figure 5.2(b) shows the result after the application of the proposed method. In this case, the window of size 3×3 was sufficient to solve the inverse problem effectively.

Comparison with Existing Methods:

To test the efficiency of the proposed algorithm, it was compared with existing methods for Radon transform. For the comparison, traditional high resolution



(a)



(b)

Figure 5.2: Efficient apex-shifted hyperbolic Radon transform: (a) The synthetic seismic reflected data. (b) The data after the application of inverse Radon transform.

Transform Type	Noise	Time	MSE
Proposed Radon Transform	0%	1.58 min	0.0071
Proposed Radon Transform	10%	1.57 min	0.0073
Proposed Radon Transform	20%	1.58 min	0.0077
Proposed Radon Transform	30%	1.59 min	0.0080
Time domain traditional Radon Transform	0%	11.46 min	0.0070
Time domain traditional Radon Transform	10%	12.14 min	0.0073
Time domain traditional Radon Transform	20%	12.12 min	0.0077
Time domain traditional Radon Transform	30%	12.25 min	0.0079

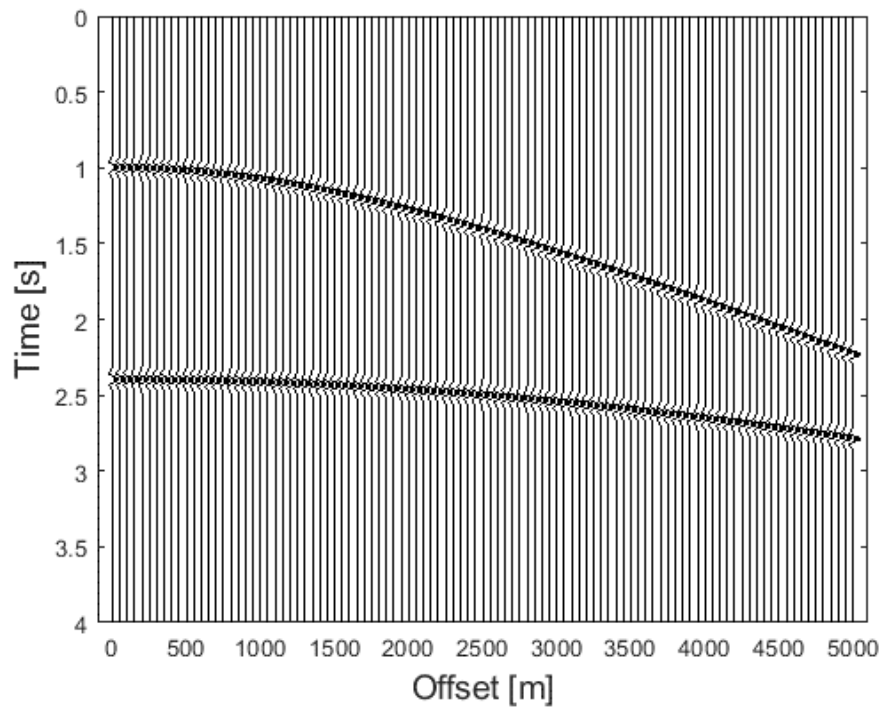
Table 5.1: Time comparison: Proposed and traditional apex shifted Radon transform

apex shifted hyperbolic Radon transform, is utilized. Figures 5.3(a) and 5.3(b) shows the original data and the data after the traditional apex shifted Radon transform.

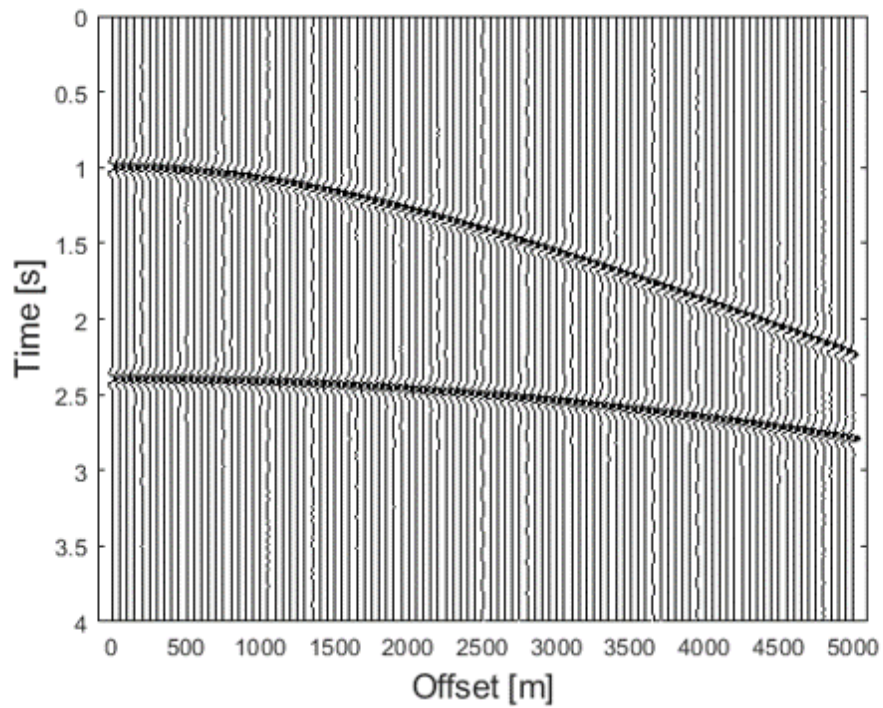
Quantitative Analysis:

The computational difference between both these methods, with and without noise is presented in Table 5.1. Furthermore, table also presents the data error between the original data and after applications of the hyperbolic Radon transform. From the Table it is evident that the proposed method is about 7 times faster and provides comparable results to the apex shifted hyperbolic Radon transform.

These results are in accordance with the computational efficiency of the method as discussed in section 5.2.1. In this case, $N_w = 9$, $N_{x_r} = 50$, $N_\tau = 500$, $N_v = 20$, $N_{x_d} = 50$, and $k = 7$. Cost in terms of major mathematical operations



(a)



(b)

Figure 5.3: Traditional apex-shifted hyperbolic Radon transform: (a) The synthetic seismic reflected data. (b) The data after the application of inverse Radon transform.

for the traditional apex-shifted hyperbolic Radon transform is given by:

$$\begin{aligned} Cost_{k_f} &= kN_{x_r}N_{\tau}N_vN_{x_d}, \\ &= 7 \times 50 \times 500 \times 20 \times 50 = N_{\tau}N_vN_{x_d} = 175 \times 10^6. \end{aligned}$$

Similarly, for the proposed algorithm the cost is given by:

$$\begin{aligned} Cost_{k_p} &= (k - 1)(N_w)^4 + N_{x_r}N_{\tau}N_vN_{x_d} \\ &= 6 \times 9^4 + 50 \times 500 \times 20 \times 50 = N_{\tau}N_vN_{x_d} = 25 \times 10^6. \end{aligned}$$

From above it is evident that the cost depend upon the number of iterations of the algorithm. As the number of iterations increases, which is true for complex data sets, the computational saving increases.

5.3.1 3-D Data

The same method was applied for the 3-D real seismic data. The real data from Waihapa, New Zealand¹ was used for the testing. The proposed method was applied to in-line and cross-line dimension separately. The in-line 211 data is shown in Figure 5.5(a). By applying the forward and reverse Radon transform the data is presented in Figure 5.5(b).

Similarly, the proposed method was also applied to the cross-line number 153 of the 3-D data base. The data is presented in Figure 5.6(a). The result after the application of the proposed method is shown in Figure 5.6(b).

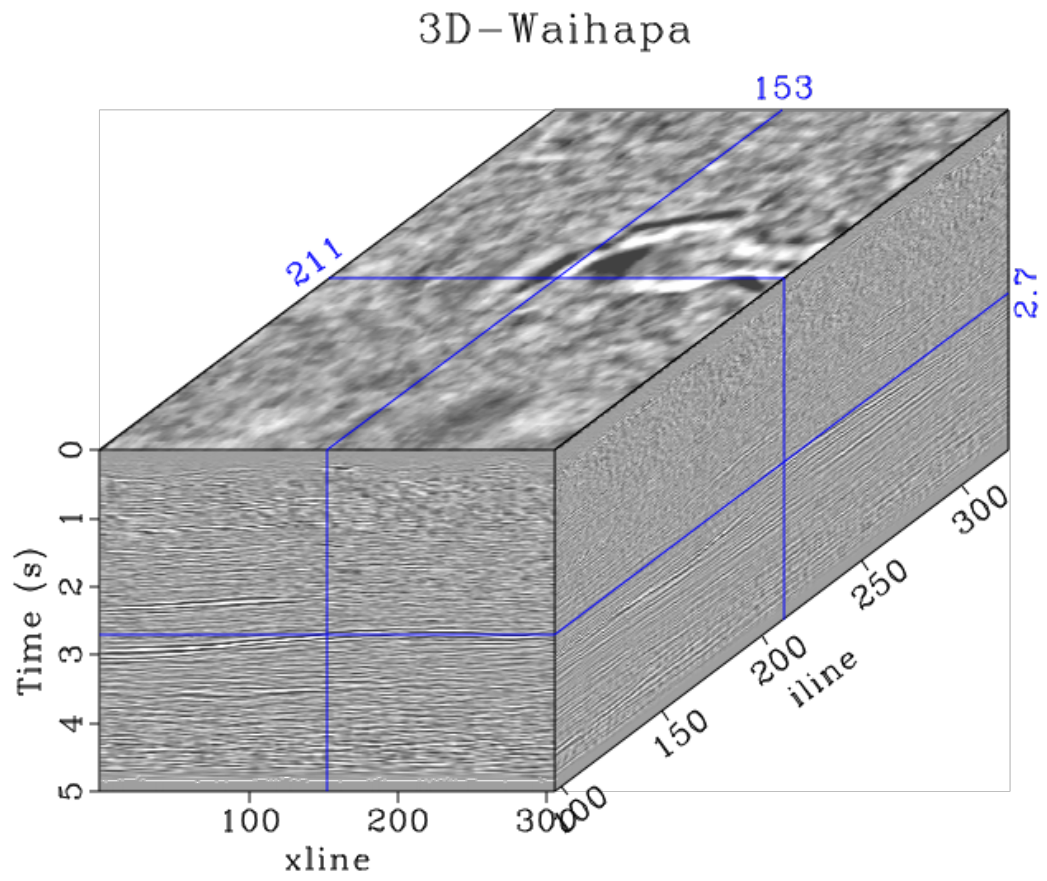
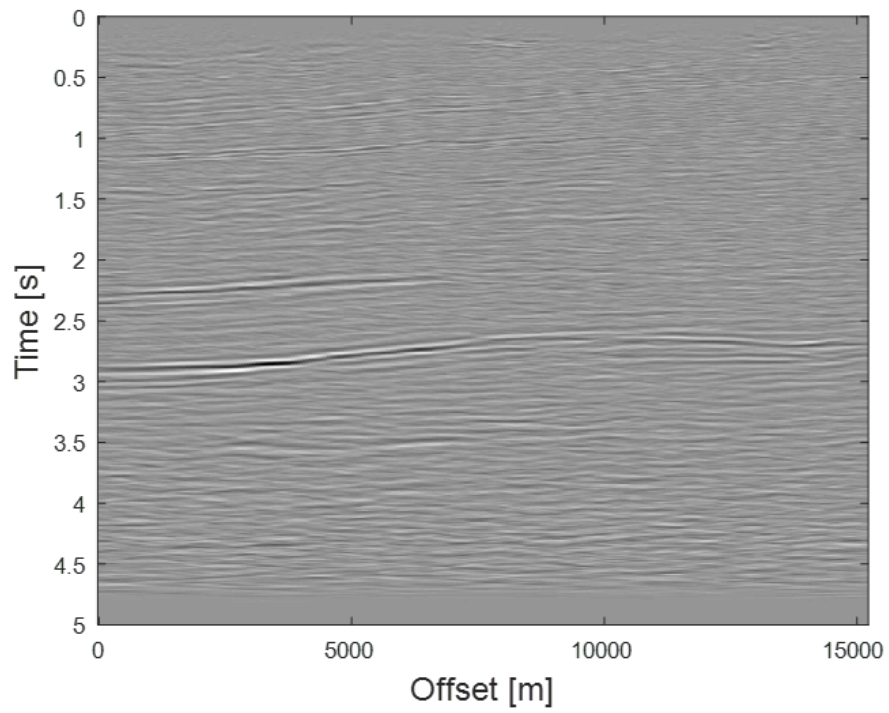
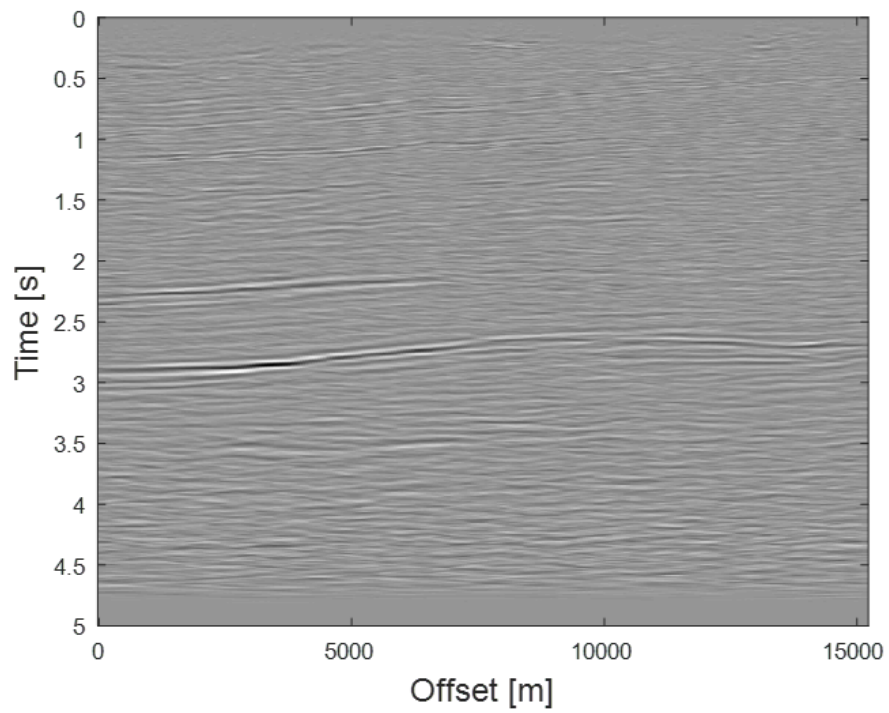


Figure 5.4: 3-D Real Data from Waihapa, New Zealand (Courtesy of New Zealand Petroleum and Minerals (NZPM)).

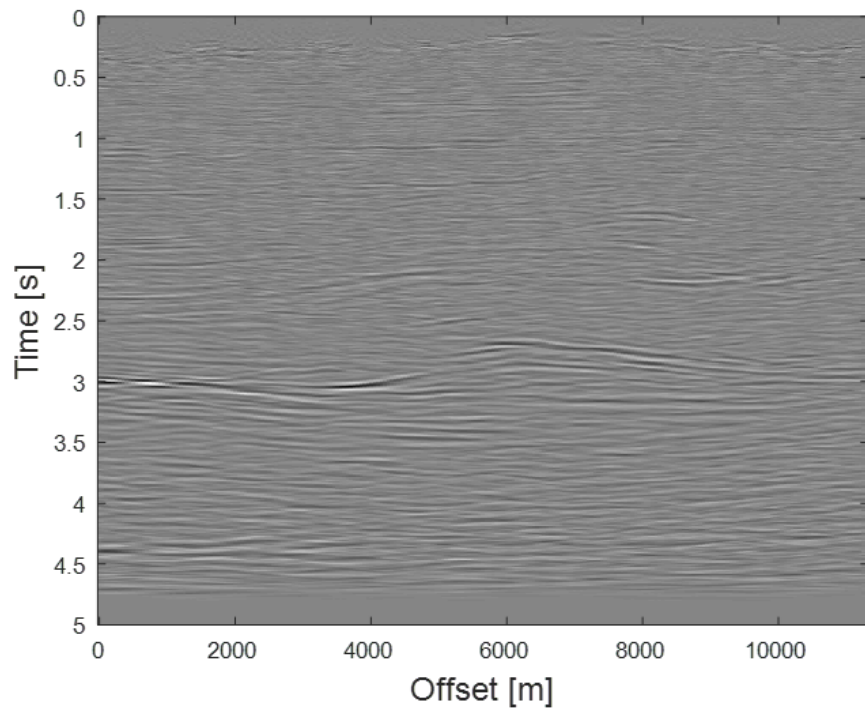


(a)

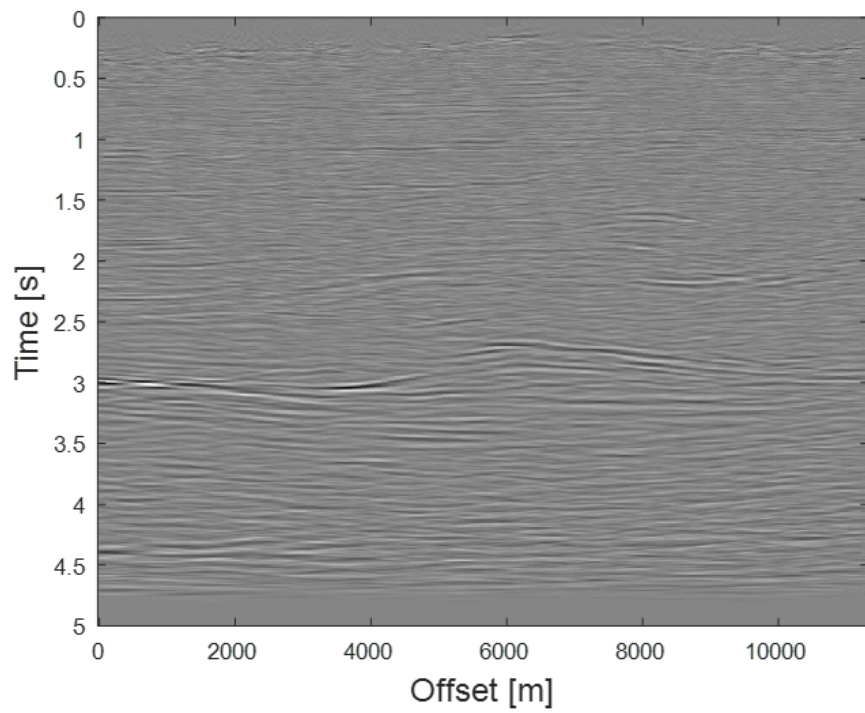


(b)

Figure 5.5: (a) The real in-line data from the Waihapa, New Zealand. (b) The data after the proposed method (Courtesy of New Zealand Petroleum and Minerals (NZPM)).



(a)



(c)

Figure 5.6: (a) The real cross-line data from the Waihapa, New Zealand. (b) The data after the proposed method (Courtesy of New Zealand Petroleum and Minerals (NZPM)).

5.4 Conclusion

Apex shifted hyperbolic Radon transform is the most robust and computational expensive Radon transform and an efficient way of calculating this hyperbolic Radon transform has been proposed. The proposed method utilizes the prior information of the adjoint based hyperbolic Radon transform to reduce the search space of apex based hyperbolic Radon transform and can significantly reduce the computational time of the existing hyperbolic Radon transform as evident from the simulation results for 2-D and 3-D dataset. From the comparison, it is evident that the proposed method is about k times faster than the existing apex based hyperbolic Radon transform, where k is the number of iterations.

CHAPTER 6

CONCLUSION

In this thesis, the Radon transform for the seismic data processing was studied and three new versions of high resolution Radon transform were proposed (Chapters 3-5) for 2-D and 3-D seismic data. The proposed methods are efficient, robust, and produce high resolution Radon transform. These methods are used for seismic interpolation and multiple attenuation of 2-D and 3-D seismic data.

We started with the theory of generalized Radon transform and its applications in Chapter 2. Different types of Radon transform that are used for seismic data processing have been covered with different examples. Through proper mathematical derivations it has been shown that $\tau - p$ and $\tau - q$ domain provides sparse representation of the linear and parabolic (or hyperbolic) seismic events, respectively. Furthermore, it has been shown that hyperbolic Radon transform is best suited for seismic data processing, however, due to large computational costs, it is not feasible. We also studied the limitations of the existing Radon transform techniques and based on these limitations and drawbacks, we have de-

veloped three different methods for Radon transforms. First two techniques, are the modification for the parabolic and linear Radon transform (Chapters 3 and 4) and the last proposed method is an efficient way to calculate the apex shifted hyperbolic Radon transform (Chapter 5).

To be precise, we developed a new technique for the robust Radon transform which is discussed in Chapter 3. A new angle based parameter has been proposed to calculate the Radon transform and the proposed technique is termed as angle based Radon transform. It has been shown that by introducing the angle to traditional Radon transform the limitations of parabolic Radon transform can be overcome and unlike the existing parabolic and linear Radon transform the proposed method doesn't require normal move-out correction which require manual human input. Furthermore, the proposed angle based Radon transform work for even far offset where traditional techniques fail to properly map the seismic events. Furthermore, the proposed method can be applied for 2-D and 3-D seismic data processing.

To investigate the performance of the angle based Radon transform, it was applied for two important seismic data processing applications which are interpolation of missing seismic traces and attenuation of multiple reflection. We tested the proposed method for different 2-D and 3-D seismic data sets. Furthermore, the effect of noise has been observed and the result showed that the obtained transform is robust in nature and does not require normal move-out correction. Comparison with existing Radon transform was also presented in detail and it has

been shown that the proposed method even works for far offset where traditional methods suffer to focus. In short, the proposed angle based Radon transform removes the need of normal move-out correction and produces high resolution, robust, and efficient Radon transform.

As the demand for denser high resolution data is increasing so is the importance of the seismic data interpolation. In this thesis, we proposed a new efficient and robust way of seismic data interpolation. In Chapter 4, projections on to convex sets (POCS) along with Radon transform has been discussed for the interpolation of the seismic data. It is shown that parabolic and linear Radon transform can be used along with the POCS to calculate the missing traces accurately. Interpolation is performed by introducing three different convex and closed sets in time-offset and Radon domain. The proposed method has been applied to real and synthetic data sets and the results showed that the error between the interpolated and the original traces is quite small. Furthermore, the comparison with existing method showed that the proposed method outperforms the existing methods based on Radon transform.

Since, the seismic travel time curves are hyperbolic in nature, therefore, hyperbolic Radon transform is an obvious choice for the seismic data. However, due to the the complexity of the hyperbolic transform, it is not suitable to process a large amount of seismic data and mostly parabolic Radon transform is used. We propose an efficient way to calculate apex shifted hyperbolic Radon transform in Chapter 5. The proposed method utilizes the prior information of the adjoint

based hyperbolic Radon transform to reduce the search space of apex based hyperbolic Radon transform and can significantly reduce the computational time of the existing hyperbolic Radon transform as evident from the simulation results for 2-D and 3-D dataset. Computational comparison with the existing method showed that the proposed method is about k , number of iterations, times faster than the traditional method with comparable results to the existing method.

In summary, in this thesis three different Radon transform are proposed which are robust, efficient, easy to implement and can be used for 2-D and 3-D datasets. From the results, it is interesting to see how different types of Radon transforms can be used for various applications of seismic signal processing. The proposed Radon transform does not only work well but it is significantly faster than the existing proposed transform.

6.1 Further Work

In this research, Radon transform is used with frequency domain representation. Instead of using frequency domain Radon transform representation, time-domain high resolution Radon transform can be used. Time-domain Radon transform will map the seismic events into the single point, more accurately at the cost of computational time.

By tweaking the proposed methods, they can be extended and applied for other seismic applications like denoising and first arrival picking. To achieve this the POCS can be efficiently used by introducing more convex sets and constraint.

One such constraint can be removing the noise in the Radon domain.

In this thesis, the efficiency of the algorithm is not considered. It is believed that by introducing the sparsity and posing this problem in terms of compressive sensing, the efficiency can be increased. For this purpose, different recovery algorithm can be tested along with the compressive sensing.

One problem with the $\tau - q$ or $\tau - p$ transform is that their basis are not orthogonal. As a result, it requires a large p -range and small p -increment (i.e., the model space is large, especially for high dimensions) to represent the input data accurately. Furthermore, the frequency space is also huge. So, by utilizing the frequency slicing the problem can be simplified and Radon transform can be calculated more efficiently.

Furthermore, the methods can be applied and tested on more challenging real data sets.

REFERENCES

- [1] Ö. Yilmaz, *Seismic data analysis*. Society of Exploration Geophysicists
Tulsa, 2001, vol. 1.
- [2] D. W. Steeples and R. D. Miller, “Seismic reflection methods applied to
engineering, environmental, and groundwater problems,” *Geotechnical and
environmental geophysics*, vol. 1, pp. 1–30, 1990.
- [3] A. B. Weglein, F. V. Araújo, P. M. Carvalho, R. H. Stolt, K. H. Matson,
R. T. Coates, D. Corrigan, D. J. Foster, S. A. Shaw, and H. Zhang, “Inverse
scattering series and seismic exploration,” *Inverse problems*, vol. 19, no. 6, p.
R27, 2003.
- [4] M. B. Dobrin and C. H. Savit, *Introduction to geophysical prospecting*.
McGraw-hill New York, 1960, vol. 4.
- [5] D. Trad, T. Ulrych, and M. Sacchi, “Latest views of the sparse Radon
transform,” *Geophysics*, vol. 68, no. 1, pp. 386–399, jan 2003.

- [6] M. Sacchi, D. Verschuur, and P. Zwartjes, “Data Reconstruction by Generalized Deconvolution,” *SEG Technical Program Expanded Abstracts*, no. October, pp. 1989–1992, 2004.
- [7] J. Fan, Z. Li, X. Song, K. Zhang, Q. He *et al.*, “Application of anisotropic high-resolution radon transform for multiple attenuation,” in *2015 SEG Annual Meeting*. Society of Exploration Geophysicists, 2015.
- [8] A. Latif and W. A. Mousa, “An Efficient Undersampled High-Resolution Radon Transform for Exploration Seismic Data Processing,” *IEEE Transactions on Geoscience and Remote Sensing*, vol. 55, no. 2, pp. 1010–1024, feb 2017.
- [9] F. Matúš and J. Flusser, “Image Representations via a Finite Radon Transform,” *IEEE Transactions on Pattern Analysis and Machine Intelligence*, vol. 15, no. 10, pp. 996–1006, 1993.
- [10] T. M. Lehmann, C. Gonner, and K. Spitzer, “Survey: interpolation methods in medical image processing,” *IEEE Trans. Med. Imag.*, vol. 18, no. 11, pp. 1049–1075, 1999.
- [11] Z. Cao, “Analysis and application of the Radon transform,” *Masters Abstracts International*, 2007.
- [12] P. Kuchment, “Generalized transforms of Radon type and their applications,” *Proceedings of Symposia in Applied Mathematics*, vol. 0000, pp. 1–32, 2006.

- [13] F. Natterer, “Inversion of the attenuated Radon transform,” *Inverse Problems*, vol. 17, no. 1, pp. 113–119, 2001.
- [14] W. A. Mousa, A. A. Al-Shuhail, and A. Al-Lehyani, “A new technique for first-arrival picking of refracted seismic data based on digital image segmentation,” *Geophysics*, vol. 76, no. 5, pp. V79–V89, sep 2011.
- [15] X. Gong, C. Yu, and Z. Wang, “Separation of prestack seismic diffractions using an improved sparse apex-shifted hyperbolic Radon transform,” *Exploration Geophysics*, vol. 48, no. 4, pp. 476–484, 2017.
- [16] S. Tong, R. Wang, H. Liu, J. Zhang, and C. Bu, “High resolution radon transform and its applications in multiple suppression of seismic data in deep-sea,” *Proceedings of the 2009 2nd International Congress on Image and Signal Processing, CISP’09*, vol. 2, no. 1, pp. 1–4, oct 2009.
- [17] A. Ibrahim, P. Terenghi, and M. D. Sacchi, “Interpolation using asymptote and apex shifted hyperbolic Radon transform Interpolation using asymptote and apex shifted hyperbolic,” no. March, pp. 1–5, 2016.
- [18] A. Latif and W. A. Mousa, “Efficient under-sampled high resolution Radon transform,” *SEG Technical Program Expanded Abstracts*, no. 1985, pp. 4574–4579, 2015.
- [19] V. M. Amir, a. Javaherian, V. Minaeian, and a. Moslemi, “Multiple Attenuation by FX Parabolic Radon Transform,” *1st International Petroleum Conference & Exhibition*, no. May 2009, pp. 4–6, 2009.

- [20] J. R. Thorson and J. F. Claerbout, “Velocitystack and slantstack stochastic inversion,” *Geophysics*, vol. 50, no. 12, pp. 2727–2741, dec 1985.
- [21] Z. Cao and J. C. J. J. C. J. Bancroft, “A Semblance Weighted Radon Transform on Multiple Attenuation,” *CSEG National Convention*, vol. 2, no. 1917, pp. 298–301, 2005.
- [22] A. Latif and W. A. Mousa, “An efficient and robust method for automatic first arrival picking using under-sampled fast high resolution Radon transform,” *SEG Technical Program Expanded Abstracts 2016*, pp. 2439–2443, sep 2016.
- [23] M. D. Sacchi and T. J. Ulrych, “Highresolution velocity gathers and offset space reconstruction,” *Geophysics*, vol. 60, no. 4, p. 1169, jul 1995.
- [24] M. Ng, M. Perz *et al.*, “High resolution radon transform in the tx domain using” intelligent” prioritization of the gauss-seidel estimation sequence,” in *2004 SEG Annual Meeting*. Society of Exploration Geophysicists, 2004.
- [25] X. Gong, S. Yu, and S. Wang, “Prestack seismic data regularization using a time-variant anisotropic Radon transform,” *Journal of Geophysics and Engineering*, vol. 13, no. 4, pp. 462–469, 2016.
- [26] M. D. Sacchi, M. Porsani *et al.*, “Fast high resolution parabolic radon transform,” in *1999 SEG Annual Meeting*. Society of Exploration Geophysicists, 1999.

- [27] H. Liu and Y. Luo, “Invertible Radon transform for making true amplitude angle gathers,” *SEG Technical Program Expanded Abstracts*, pp. 4158–4163, 2015.
- [28] G. Poole *et al.*, “Radon modelling with time-frequency sparseness weights,” in *2015 SEG Annual Meeting*. Society of Exploration Geophysicists, 2015.
- [29] P. Toft, “The Radon Transform: Theory and Implementation,” Ph.D. dissertation, Technical University of Denmark, 1996.
- [30] S. Helgason, *The Radon Transform (Google eBook)*. Springer, 1999.
- [31] G. Beylkin, “Discrete Radon Transform,” *IEEE Transactions on Acoustics, Speech, and Signal Processing*, vol. 35, no. 2, pp. 162–172, feb 1987.
- [32] T. G. Feeman, *The Mathematics of Medical Imaging*, ser. Springer Undergraduate Texts in Mathematics and Technology. New York, NY: Springer New York, 2010, vol. 51, no. 1.
- [33] S. Deans, *Radon and Abel transforms*, 2000.
- [34] R. Gordon, G. T. Herman, and S. A. Johnson, “Image reconstruction from projections,” *Scientific American*, vol. 233, no. 4, pp. 56–71, 1975.
- [35] C. H. Chapman, “Generalized Radon transforms and slant stacks,” *Geophysical Journal of the Royal Astronomical Society*, vol. 66, no. 2, pp. 445–453, 1981.

- [36] M. Sarajæarvi, “Inversion of the Linear and Parabolic Radon Transform,” Ph.D. dissertation, University of Bergen, 2010.
- [37] N. Temme, “The Radon transform: first steps,” *CWI Newsletter*, vol. 15, pp. 41–46, 1987.
- [38] K. Arp, Á. Kurusa, and K. Arp, “The Radon transform on hyperbolic space,” *Geometriae Dedicata*, vol. 40, no. 1980, pp. 325–339, 1991.
- [39] P. W. Cary, “The simplest discrete Radon transform,” *SEG Technical Program Expanded Abstracts 1998*, pp. 1999–2002, jan 1998.
- [40] B. Zhou and S. a. Greenhalgh, “Linear and parabolic τ - p transforms revisited,” *Geophysics*, vol. 59, no. 7, pp. 1133–1149, 1994.
- [41] X. Gong, S. Wang, and T. Zhang, “Velocity analysis using high-resolution semblance based on sparse hyperbolic Radon transform,” *Journal of Applied Geophysics*, vol. 134, pp. 146–152, 2016.
- [42] T. Seher *et al.*, “A high-resolution apex-shifted hyperbolic radon transform and its application to multiple attenuation,” in *2017 SEG International Exposition and Annual Meeting*. Society of Exploration Geophysicists, 2017.
- [43] J. Wang, M. Ng, and M. Perz, “Seismic data interpolation by greedy local Radon transform,” *Geophysics*, vol. 75, no. 6, p. WB225, 2010.
- [44] D. O. Trad, “Interpolation and multiple attenuation with migration operators,” *Geophysics*, vol. 68, no. 6, pp. 2043 – 2054, 2003.

- [45] X. Jiang, F. Zheng, H. Jia, J. Lin, and H. Yang, “Time-domain hyperbolic Radon transform for separation of P-P and P-SV wavefields,” *Studia Geophysica et Geodaetica*, vol. 60, no. 1, pp. 91–111, jan 2016.
- [46] S. Karimpouli, A. Malehmir, H. Hassani, H. Khoshdel, and M. Nabi-Bidhendi, “Automated diffraction delineation using an apex-shifted Radon transform,” *Journal of Geophysics and Engineering*, vol. 12, no. 2, pp. 199–209, 2015.
- [47] D. Hampson, “Inverse velocity stacking for multiple elimination,” *Journal of the Canadian Society of Exploration Geophysicists*, vol. 22, no. 1, pp. 44–55, jan 1986.
- [48] M. Schonewille, P. Aaron, and T. Allen, “Applications of time-domain high-resolution radon demultiple,” *ASEG Extended Abstracts*, vol. 2007, no. 1, pp. 1–5, 2007.
- [49] A. Gholami and H. R. Siahkoochi, “Simultaneous constraining of model and data smoothness for regularization of geophysical inverse problems,” *Geophysical Journal International*, vol. 176, no. 1, pp. 151–163, jan 2009.
- [50] Y. Luo, J. Xia, R. D. Miller, Y. Xu, J. Liu, and Q. Liu, “Rayleigh-wave mode separation by high-resolution linear radon transform,” *Geophysical Journal International*, vol. 179, no. 1, pp. 254–264, oct 2009.

- [51] S. T. Kaplan, M. Naghizadeh, and M. D. Sacchi, “Data reconstruction with shot-profile least-squares migration,” *Geophysics*, vol. 75, no. 6, pp. WB121–WB136, nov 2010.
- [52] O. Yilmaz, “Seismic data processing, volume 2 of investigations in geophysics,” *Society of Exploration Geophysicists*, 1987.
- [53] B. Liu and M. D. Sacchi, “Minimum weighted norm interpolation of seismic records,” *Geophysics*, vol. 69, no. 6, pp. 1560–1568, 2004.
- [54] G. Hennenfent and F. J. Herrmann, “Seismic denoising with nonuniformly sampled curvelets,” *Computing in Science and Engineering*, vol. 8, no. 3, pp. 16–25, 2006.
- [55] N. Gulunay, “Seismic trace interpolation in the Fourier transform domain,” *Geophysics*, vol. 68, no. 1, p. 355, 2003.
- [56] B. Recht, “Tu-04-13 Seismic Data Interpolation and Denoising Using SVD-free Low-rank Matrix Factorization,” in *75th EAGE Conference & Exhibition incorporating SPE EUROPEC 2013 London, UK, 10-13 June 2013*, no. June 2013, 2013, pp. 10–13.
- [57] A. J. Berkhout and D. J. Verschuur, “Imaging of multiple reflections,” *Geophysics*, vol. 71, no. 4, pp. SI209–SI220, 2006.
- [58] W. Curry and G. Shan, “Interpolation of near offsets using multiples and prediction-error filters,” in *Geophysics*, vol. 75, no. 6, jun 2010, pp. WB153–WB164.

- [59] Y. Wang, Y. Luo, and G. T. Schuster, “Interferometric interpolation of missing seismic data,” *Geophysics*, vol. 74, no. 3, pp. SI37–SI45, may 2009.
- [60] J.-J. CAO, Y.-F. WANG, and C.-C. YANG, “Seismic Data Restoration Based on Compressive Sensing Using Regularization and Zero-Norm Sparse Optimization,” *Chinese Journal of Geophysics*, vol. 55, no. 2, pp. 239–251, mar 2012.
- [61] F. J. Herrmann, D. Wang, and G. Hennenfent, “Multiple prediction from incomplete data with the focused curvelet transform,” *SEG Technical Program Expanded Abstracts*, vol. 26, no. 1, pp. 2505–2509, 2007.
- [62] H. Mansour, F. J. Herrmann, and Ö. Yilmaz, “Improved wavefield reconstruction from randomized sampling via weighted one-norm minimization,” *Geophysics*, vol. 78, no. 5, pp. V193–V206, sep 2013.
- [63] A. Ibrahim, P. Terenghi, M. D. Sacchi *et al.*, “Wavefield reconstruction using a stolt-based asymptote and apex shifted hyperbolic radon transform,” in *2015 SEG Annual Meeting*. Society of Exploration Geophysicists, 2015.
- [64] A. J. Berkhout and E. J. Verschuur, “Estimation of multiple scattering by iterative inversion, part 1: {T}heoretical considerations,” *Geophysics*, vol. 62, no. 5, pp. 1586–1595, 1995.
- [65] D. J. Verschuur, “Surface-related multiple elimination, an inversion approach,” Ph.D. dissertation, Delft University of Technology, 2013.

- [66] A. J. Berkhout and D. J. Verschuur, “Estimation of multiple scattering by iterative inversion, Part II: Practical aspects and examples,” *Geophysics*, vol. 62, no. 5, pp. 1596–1611, 1997.
- [67] S. T. Kaplan and K. A. Innanen, “Adaptive subtraction of free surface multiples through order-by-order prediction, matching filters and independent component analysis,” *SEG - Society of Exploration Geophysicists*, vol. 73, no. 3, pp. 2694–2698, 2006.
- [68] C. A. da Costa Filho, L. T. Duarte, and M. Tygel, “Multiple attenuation through independent component analysis: a case study,” *13th International Congress of the Brazilian Geophysical Society & EXPOGEF*, pp. 1435–1438, aug 2013.
- [69] D. Donno, “Improving multiple removal using least-squares dip filters and independent component analysis,” *Geophysics*, vol. 76, no. 5, pp. V91–V104, 2011.
- [70] W.-k. Lu and L. Liu, “Adaptive multiple subtraction based on constrained independent component analysis,” *Geophysics*, vol. 74, no. 1, p. V1, 2009.
- [71] H. Stark and Y. Yang, *Vector Space Projections: a numerical approach to Signal and Image processing, Neural nets, and Optics*, 1st ed. John Wiley and Sons Publisher, 1998.
- [72] W. A. Mousa, M. van der Baan, S. Boussakta, and D. C. McLernon, “Designing stable extrapolators for explicit depth extrapolation of 2D and

- 3D wavefields using projections onto convex sets,” *Geophysics*, vol. 74, no. 2, p. S33, mar 2009.
- [73] A. E. Çetin, Ö. N. Gerek, and Y. Yardimci, “Equiripple FIR filter design by the FFT algorithm,” *IEEE Signal Processing Magazine*, vol. 14, no. 2, pp. 60–64, mar 1997.
- [74] K. C. Haddad, H. Stark, and N. P. Galatsanos, “Constrained {FIR} Filter Design by the Method of Vector Space Projections,” *IEEE Trans. on Circuits and Systems*, vol. 47, no. 8, pp. 714–725, aug 2000.
- [75] A. Ozbek, L. Hoteit, and G. Dumitru, “3D filter design on a hexagonal grid with applications to point-receiver land acquisition,” *74th Ann. Internat. Mtg.*, no. October, pp. 1965–1968, 2004.
- [76] K. C. Haddad, “Design of digital linear-phase fir crossover systems for loudspeakers by the method of vector space projections,” *IEEE Transactions on Signal Processing*, vol. 47, no. 11, pp. 3058–3066, nov 1999.
- [77] P. Oskoui-Fard and H. Stark, “Tomographic Image Reconstruction Using the Theory of Convex Projections,” *IEEE Trans. on Medical Imaging*, vol. 7, no. 1, pp. 45–58, mar 1988.
- [78] M. I. Sezan, “An overview of convex projections theory and its application to image recovery problems,” *Ultramicroscopy*, vol. 40, no. 1, pp. 55–67, 1992.

- [79] a. Levi and H. Stark, “Signal restoration from phase by projections onto convex sets,” in *ICASSP '83. IEEE International Conference on Acoustics, Speech, and Signal Processing*, vol. 8, no. 6, 1983, p. 3.
- [80] —, “Image restoration by the method of generalized projections with application to restoration from magnitude,” *ICASSP '84. IEEE International Conference on Acoustics, Speech, and Signal Processing*, vol. 9, no. 9, pp. 932–943, sep 1984.
- [81] R. J. Marks and L. E. Atlas, “Kernel Synthesis for Generalized Time-Frequency Distributions Using the Method of Alternating Projections Onto Convex Sets,” *IEEE Transactions on Signal Processing*, vol. 42, no. 7, pp. 1653–1661, jul 1994.
- [82] T. Bjarnason and W. Menke, “Application of the POCS inversion method to cross-borehole imaging,” *Geophysics*, vol. 58, no. 7, pp. 941–948, jul 1993.
- [83] J. Ma, “Three-dimensional irregular seismic data reconstruction via low-rank matrix completion,” *Geophysics*, vol. 78, no. 5, pp. V181–V192, 2013.
- [84] F. Janiszewski, C. Mosher, and Y. Ji, “Increasing the Efficiency of Seismic Data Acquisition via Compressive Sensing,” *Offshore Technology ...*, no. April, 2014.
- [85] F. J. Herrmann, U. Böniger, and D. J. Verschuur, “Non-linear primary-multiple separation with directional curvelet frames,” *Geophysical Journal International*, vol. 170, no. 2, pp. 781–799, aug 2007.

- [86] E. van den Berg, M. P. Friedlander, G. Hennenfent, F. J. Herrmann, R. Saab, and Ö. Yilmaz, “Algorithm 890,” *ACM Transactions on Mathematical Software*, vol. 35, no. 4, pp. 1–16, 2009.

Vitae

- Name: Arbab Latif
- Nationality: Pakistan
- Date of Birth: Feb 15,1987.
- Email: *arbablatif@gmail.com*
- Permanent Address: Gujranwala Cantt, Punjab, Pakistan
- MS Electrical Engineering: King Fahd University of Petroleum and Minerals, Saudi Arabia.
- BE Electrical Engineering: National University of Sciences and Technology, Pakistan.
- Research Papers:
 - Arbab Latif and Wail. A. Mousa, "An Efficient Under-Sampled High-Resolution Radon Transform for Exploration Seismic Data Processing", IEEE Transactions on Geosciences & Remote Sensing, vol. 55, no. 2, pp. 1010-1024, Feb. 2017.
 - Arbab Latif and Wail. A. Mousa, An Efficient and Robust Method for Automatic First Arrival Picking using Under-Sampled Fast High-Resolution Radon Transform, Proceedings of the 86th Society of Exploration Geophysicists, Annual Meeting, Dallas, TX, USA, SEG, 2016.

- Arbab Latif and Wail. A. Mousa, Efficient Under-Sampled High-Resolution Radon Transform, Proceedings of the 85th Society of Exploration Geophysicists, Annual Meeting, New Orleans, LA, USA, SEG, 2015.
 - Arbab Latif and Wail. A. Mousa, "An Angle based High-Resolution Radon Transform for Exploration Seismic Data Processing", IEEE Transactions on Geosciences & Remote Sensing, submitted.
 - Arbab Latif and Wail. A. Mousa, "POCS based Radon transform method for the missing seismic traces", Geophysics, submitted.
 - Arbab Latif and Wail. A. Mousa, "An Efficient method to compute apex shifted hyperbolic Radon transform", Geophysical Prospecting, submitted.
- Book:
 - Arbab Latif and Wail. A. Mousa, "Compressive Sensing for Seismic Data Analysis", J. Wiley & Sons, under preparation.
- Patent:
 - Wail A. Mousa, Arbab Latif, Abdullatif Al-Shuhail, System and Method for Acquisition and Processing of Seismic Data using Compressive Sensing, U.S. Patent Application 20160327661, filed May 2016. Patent Pending.